Studying the ICM velocity structure within galaxy clusters with simulations and X–ray observations

Veronica Biffi

Sigillum Universitatis Ludovici Maximiliani

Ludwig-Maximilians-Universität

Sigillum Universitatis Ludovici Maximiliani

Studying the ICM velocity structure within galaxy clusters with simulations and X–ray observations

Dissertation der Fakultät für Physik

Sigillum Universitatis Ludovici Maximiliani

1. Gutachter: Prof. Dr. Hans Böhringer

2. Gutachter: Prof. Dr. Jochen Weller

Tag der mündlichen Prüfung: 23.04.2012

Contents

List of Figures

List of Tables

Zusammenfassung

Galaxienhaufen sind ideale Laboratorien, um sowohl Kosmologische Modelle als auch physikalische Prozesse, die auf kleineren Skalen ablaufen, zu testen. Das heiße Gas (ICM), welches innerhalb des durch die dunkle Materie erzeugten Potentials des Galaxienhaufens sitzt und im Röntgenlicht beobachtbar ist, stellt immer noch einen der besten Wege dar, um intrinsische Haufeneigenschaften zu untersuchen. Methoden, die auf Röntgenbeobachtungen des ICM beruhen, werden häufig benutzt, um die Gesamtmasse des Haufens zu bestimmen, wobei angenommen wird, dass das Gas dem vorhandenen Potentialtopf folgt, sphärisch symmetrisch verteilt ist und der thermische Druck dominiert. Nicht-thermische Bewegungen können ebenfalls im ICM auftreten, tragen zum Gesamtdruck bei und müssen bei der Massenbestimmung berücksichtigt werden.

In dieser Dissertation untersuche ich die thermisch-dynamische Struktur des ICM durch die Kombination von hydrodynamischen Simulationen und synthetischen Röntgenbeobachtungen von Galaxienhaufen. Das Hauptziel ist die Untersuchung ihrer Gasgeschwindigkeitsfelder und die Folgen von nicht-thermischen Bewegungen: erstens durch die direkte Analyse von Geschwindigkeitsstrukturen in simulierten Haufen und zweitens durch die Rekonstruktion der internen ICM Struktur durch virtuelle Beobachtungen. Hierfür habe ich einen Röntgenphotonensimulator entwickelt und angewandt, um synthetische Röntgenspektren der Gaskomponente von hydrodynamischen Simulationen von Haufen zu erhalten.

Die wichtigsten Ergebnisse sind wie folgt.
(i) Geordnete Rotationsbewegungen im Gasgeschwindigkeitsfeld von Haufenzentren können während des Massenwachstumsprozesses entstehen, sind aber ein vorübergehendes Phänomen, das leicht durch Durchgänge von gasreichen Subhalos zerstört werden kann. Das weist daraufhin, dass in stetig wachsenden Halos dieses Phänomen im

Allgemeinen nur einen geringen Effekt hat. Nichtsdestotrotz können stark gestörte Systeme (z.B. bei großen Zusammenstößen) in der Tat signifikante geordnete Bewegungen und Rotationen ausbilden, die zu Fehlern bei der Bestimmung der Gesamtmasse von bis zu 20% führen. (ii) Es ist in der Tat möglich, die thermische Struktur des ICM in Haufen durch eine Röntgenspektralanalyse zu rekonstruieren, indem die Verteilung der Emissionsstärke (EM) des Gases als Funktion der Temperatur gemessen wird. Dies ist mit jetzigen Röntgenteleskopen (z.B. Suzaku) durch Multi-Temperaturrekonstruktion von Röntgenspektren möglich. (iii) Hochpräzisionsröntgenspektrometer, wie z.B. ATHENA, werden es uns erlauben, Geschwindigkeitsamplituden von nicht-thermischen Bewegungen des ICM durch die geschwindigkeitsbedingte Verbreiterung von Emissionslinien von Schwerionen (z. B. Eisen) zu messen. Die Ergebnisse in dieser Arbeit wurden durch die Anwendung des virtuellen Röntgensimulators erzielt, mit dem synthetische ATHENA Spektren von simulierten Haufen generiert wurden. Diese, in der Zentralregion gemessenen, nicht-thermischen Geschwindigkeiten innerhalb des ICM können dazu verwendet werden, den dynamischen Zustand des Haufens zu charakterisieren und den Grad der Abweichung von der erwarteten Selbstähnlichkeit zu bestimmen. Durch den Ausschluss der Haufen mit der höchsten, nicht-thermischen Geschwindigkeitsdispersion kann die Streuung der gemessenen Skalierungsrelationen (z.B. $L_X - T$) signifikant reduziert werden, was einen deutlich besseren Vergleich zwischen Beobachtungen und Simulationen ermöglicht.

Summary

Galaxy clusters are optimal laboratories to test cosmology as well as models for physical processes acting on smaller scales. X–ray observations of the hot gas filling their dark matter potential well, i.e. the intra–cluster medium (ICM), still provides one of the best ways to investigate the intrinsic properties of clusters. Methods based on X–ray observations of the ICM are commonly used to estimate the total mass, assuming that the gas traces the underlying potential well and satisfies spherical symmetry, and thermal motions dominate the total pressure support. However, non–thermal motions are likely to establish in the ICM, hence, contribute to the total pressure and have to be taken into account in the mass estimate.

In this thesis I study the ICM thermo–dynamical structure by combining hydrodynamical simulations and synthetic X–ray observations of galaxy clusters. The main goal is to study their gas velocity field and the implications due to non–thermal motions: first, by analysing directly the velocity patterns in simulated clusters and, secondly, by reconstructing the internal ICM structure from mock X–ray spectra. To this aim, I developed and applied an X–ray photon simulator to obtain synthetic X–ray spectra from the gas component in hydrodynamical simulations of galaxy clusters.

The main findings of this work are as follows.
(i) Ordered, rotational patterns in the gas velocity field in cluster cores can establish during the mass assembly process, but are found to be transient phenomena, easily destroyed by passages of gas–rich subhaloes. This suggests that in smoothly growing haloes the phenomenon is in general of minor effect. Nonetheless, major mergers or highly disturbed systems can indeed develop significant ordered motions and rotation, which contribute up to 20% to the total mass. (ii) It is indeed possible to reconstruct the thermal structure of the ICM in clusters from X–ray spectral analysis, by recovering the emission measure (EM) distribution of the gas as a function of temperature. This is

possible with current X–ray telescopes (e.g. Suzaku) via multi–temperature fitting of X–ray spectra. (iii) High–precision X–ray spectrometers, such as ATHENA, will allow us to measure velocity amplitudes of ICM non–thermal motions, from the velocity broadening of heavy–ion (e.g. iron) emission lines. In this work, these achievements are obtained by applying the virtual X–ray simulator to generate ATHENA synthetic spectra of simulated clusters. The non–thermal velocity of the ICM in the central region is used to further characterise the cluster and the level of deviation from the expected self–similarity. By excluding the clusters with the highest non–thermal velocity dispersion, the scatter of the $L_X - T$ relation for the sample is significantly reduced, which will allow for a more precise comparison between observations and simulations.

Part I

General overview

Chapter 1

Introduction

1.1 The standard cosmological paradigm

The matter content of the Universe is constituted only for a small fraction by the visible objects that we can observe, such as gas, stars, galaxies, groups and clusters. The mass dominant component is indeed in the form of non-baryonic, "dark matter" (DM), which interacts only gravitationally. Although the constituent particles of the Dark Matter are still unknown, the scenario that best explains the observed Universe seems to require this matter component to be "cold" ("CDM", cold dark matter), i.e. its particles were non–relativistic at the moment of decoupling between matter and radiation, during the early stages of the evolution of the Universe.

Nonetheless, the baryonic and dark matter cannot be the only cosmic components, since they would imply the Universe to stop expanding end eventually recollapse or the expansion rate to become remarkably low. On the contrary, observational studies of distant supernovae in the late 1990s (Riess et al., 1998; Perlmutter et al., 1999) showed that the Universe is expanding with a rate which is higher than in the past. This requires the introduction of an additional contribution to the cosmic energy content, which must be indeed dominant and have a repulsive effect. The characteristics and nature of this component are still unknown and therefore this is usually referred to as "dark energy". Despite the fact that several theoretical models have been developed in order to interpret the dark energy (see, e.g., Weinberg and Kamionkowski, 2003; Bartelmann et al., 2006), it is commonly represented with the Cosmological Constant term, Λ, originally introduced by Einstein into the field equations describing the evolution of the Universe.

The so–called ΛCDM paradigm (Bryan and Norman, 1998) represents the standard

cosmological model describing the Universe. Recent observational estimates obtained from the seven–year WMAP (Komatsu et al., 2011) data provides $\Omega_{0,\Lambda} = 0.728$, $\Omega_{0,M} = 0.272$ and $\Omega_{0,b} = 0.045$, for the density parameter of dark energy, dark matter and baryonic matter, respectively, and $H_0 = 70.4 \, \text{km s}^{-1} \, \text{Mpc}^{-1}$ for the Hubble constant.

1.2 Hierarchical structure formation

The cosmic microwave background (CMB) radiation, serendipitously discovered in 1965 (for which Penzias and Wilson were later awarded with the Nobel Prize), is the thermal radiation permeating almost uniformly the whole Universe, theoretically expected to be left as a relic of a primordial, very hot phase of the cosmic evolution. CMB radiation has been proven to have an almost perfect black–body spectrum at a temperature of 2.725K, and a low degree of anisotropy, confirming indeed the large–scale isotropy of the Universe. Nonetheless, sophisticated measurements obtained with the COBE and WMAP satellites (see Fig. 1.1) provide evidences for primordial inhomogeneities in the density/energy field, visible, for instance, as fluctuations of order 10^{-5} in the CMB temperature map.

The challenge for models of structure formation consists of explaining in detail how these initial seeds have grown into the present–epoch structures, such as galaxies and clusters.

The standard scenario assumes the perturbations observed in the CMB to originate from the amplification of quantum fluctuations during a phase of accelerated expansion of the early Universe (referred to as "inflation"). Even though several complex theories about the primordial distribution have been proposed and debated during the last decades (e.g. non–Gaussian initial conditions), the probability distribution function for the primordial fluctuations of the cosmic density field is usually assumed to be Gaussian.

The growth of these initial density perturbations can be studied analytically through the linear Jeans's theory of gravitational instability as long as the density contrast with respect to the underlying background is smaller than unity. The collapse into DM haloes, however, implies the overdensities to enter the non–linear regime and eventually grow into highly non–linear structures, for which the Jeans's theory provides no more a valid solution and a semi–analytical or numerical approach is then required.
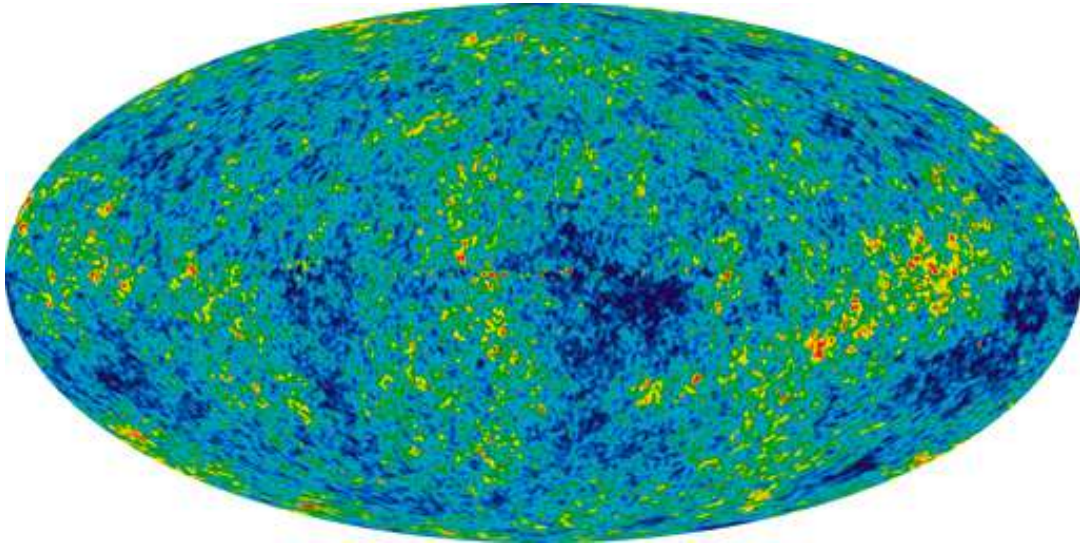
Figure 1.1: Image of the CMB anisotropy map, obtained from the WMAP satellite. Temperature fluctuations with respect to the mean are color–coded from blue (colder) to red (warmer) and represent the perturbations that have eventually grown into the present–epoch cosmic structures. Credit: NASA, WMAP Science Team

Since pioneering theoretical studies in the 1970s (Press and Schechter, 1974; White and Rees, 1978), the CDM scenario emerged as the most suited to fit observations. This commonly accepted scenario for structure formation implies a "bottom–up" hierarchy of cosmic structures, according to which smaller haloes of dark matter collapse first and consequently merge to form bigger structures.

Clusters of galaxies form from the evolution and collapse of the rare high peaks in the primordial Gaussian density fluctuations, being therefore the largest structures in the Universe that have had enough time to reach virial equilibrium. This is the reason why, in this hierarchical scenario, clusters of galaxies occupy a very special position, at the crossroad between the gravity–dominated regime and the small scales where the baryonic astrophysics become important. The treatment of clusters with a purely gravitational description is valid in their use as cosmological probes, allowing us to trace the large–scale structure of the Universe and its geometrical properties. Nonetheless, clusters contain also a fair sample of the Universe content and therefore play a key role in the study of small–scale astrophysical mechanisms, governing, for instance, the gas emission or driving the interaction and evolution of galaxies.

1.3 The role of numerical simulations

In order to properly follow the formation and evolution of cosmic structures, for which the typical overdensities reach $\approx 10^2$ or even $\approx 10^3$ and the linear theory of gravitational instability fails, a numerical approach is the best way to proceed.

Starting from the seventies of the last century, numerical simulations have been a very powerful tool to study the astrophysical N–body problem as well as cosmology. Numerical studies in cosmology significantly contributed, for instance, to confirm the reliability of the Cold Dark Matter scenario for structure formation (see, e.g., early works by Davis et al., 1985; Frenk et al., 1985; White et al., 1987; Frenk et al., 1988) and help constraining the standard cosmological paradigm, in remarkable agreement to the observed large–scale structure of the Universe (e.g. in the Millennium Simulation Run by Springel et al., 2005b, see Fig. 1.2).

Essentially, numerical codes follow the structure formation also in the non–linear regime by finding an accurate solution for the potential of the N particles under their reciprocal gravitational attraction. For collisionless matter the treatment of the gravity is enough to solve the equations of motion, since gravity is the dominant interaction. This is done, for instance, in numerical, cosmological simulations that follow exclusively the dark–matter component of the cosmic fluid (also called *dark–matter–only simulations*).
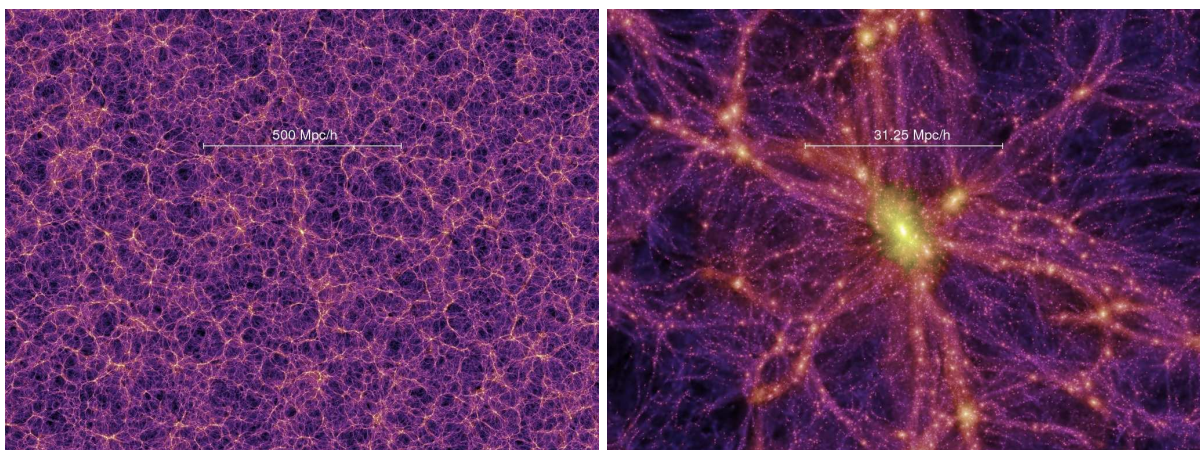
Figure 1.2: Slices through the density field of the DM–only Millennium Simulation Run, at redshift $z = 0$ (Springel et al., 2005b). The right–hand–side panel shows a zoom in by a factor of 16 with respect to the left–hand–side panel. Reference scales, in comoving units, are reported on the maps. It is evident from these snapshots of the simulation the filamentary structure which constitute the cosmic web, where small haloes are

Different techniques have been developed to solve for the gravitational interactions, such as the particle–particle (PP) or particle–mesh (PM) methods, tree codes or mixed algorithm like the Tree–PM solver implemented in the N-body code Gadget (Springel, 2005).

Numerical codes have also been developed to include hydrodynamics. Nevertheless, in cosmological applications especially, many physical processes, such as star formation or feedback phenomena, have been treated by means of semi–empirical relations in order to make calculations feasible, since a proper sub–grid treatment would be definitely too demanding in computational terms. Even though a still missing, deeper understanding of these physical processes would be required in order to implement the correct models, the approach adopted is already very useful to investigate many other properties of cosmic structures.

When the baryonic matter is also considered, being collisional instead, also the fluid equations have to be solved in addition to the gravitational potential, since the interaction among the fluid elements actually determine their behaviour. Computationally, the hydrodynamical equations can be solved with two different approaches:

- **Eulerian, grid–based codes**, which smooth the fluid onto a *grid*, with a certain spatial resolution, and discretize and solve the fluid equations for each grid point;

- **Lagrangian, Smoothed Particle Hydrodynamics (SPH) codes**, which discretize the fluid and represent it by *particles*, for which the relevant hydrodynamical quantities are calculated by smoothing on the surrounding particles.

1.3.1 Hydrodynamical simulations of galaxy clusters

The study of galaxy clusters has taken advantage of numerical, hydrodynamical simulations as well. Dedicated studies of single cluster–like haloes have been thoroughly explored and improved in the last decades. In this respect, up–to–date hydro–simulations can currently account for a vast range of gas physics, with models for star formation from multi–phase medium (e.g. Katz, 1992; Katz et al., 1996; Springel and Hernquist, 2003; Marri and White, 2003) and thermal or kinetic feedback from supernovae–driven winds (Navarro and White, 1993; Scannapieco et al., 2006; Dalla Vecchia and Schaye, 2008), chemical enrichment and cooling (e.g. Mosconi et al., 2001; Yoshida et al., 2003;
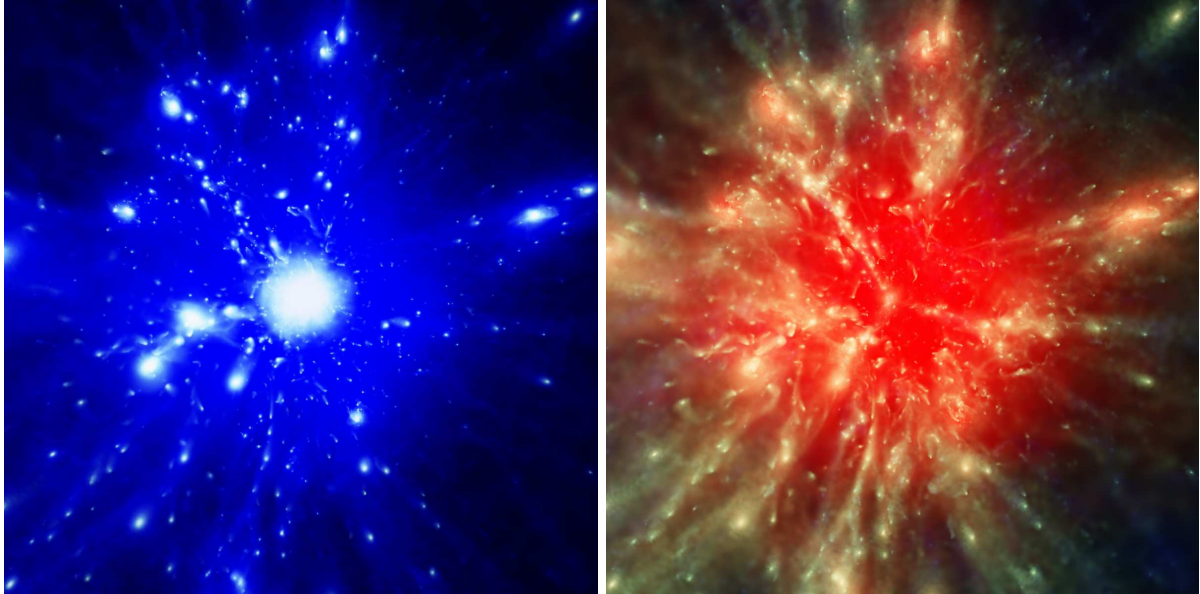
Figure 1.3: Example of a simulated galaxy cluster at $z = 0$. The maps, enclosing a region of 20 Mpc per side, visualize the gas density (left–hand–side panel) and temperature (right–hand–side panel; logarithmic color scale) and have been obtained with the ray–tracing package SPLOTCH (Dolag et al., 2008). The cluster shown here is part of the Hutt sample of cluster–like haloes (Dolag et al., 2009), originally extracted from a cosmological simulation performed with GADGET–2 and re–simulated at higher resolution by means of the ZIC technique, including star formation, cooling and supernova–driven winds.

Tornatore et al., 2004, 2007; Scannapieco et al., 2005; Maio et al., 2007, 2010), thermal conduction (Cleary and Monaghan, 1999; Jubelgas et al., 2004; Ruszkowski et al., 2010), AGN feedback (e.g. Springel et al., 2005a; Di Matteo et al., 2005; Sijacki and Springel, 2006; Sijacki et al., 2007, 2008; Puchwein et al., 2008; Fabjan et al., 2010; Dubois et al., 2010; Teyssier et al., 2011), cosmic rays (Pfrommer et al., 2007; Jubelgas et al., 2008) and magnetic fields (Phillips and Monaghan, 1985; Dolag et al., 1999; Brüggen et al., 2005; Price and Monaghan, 2005; Dolag and Stasyszyn, 2009). The possibility to include detailed descriptions for various physical processes, both in Eulerian, Adaptive Mash Refinement codes (e.g. ENZO, Norman et al. (2007); ART, Kravtsov (1999); Kravtsov et al. (2002)) and SPH (in particular, GADGET Springel et al., 2001; Springel, 2005) codes, has been particularly important to study the details of cluster intrinsic structure, in order to compare and interpret cluster observations.

One of the most convenient ways to simulate galaxy clusters with such complexity consists in isolating clusters in cosmological, DM–only simulations and re–simulate them at higher resolution including also the baryonic components and the treatment

of hydrodynamics. This is done, e.g., in SPH simulations via the so–called Zoomed Initial Condition (ZIC) technique (Tormen et al., 1997), as for the simulated cluster–like halo shown in Fig. 1.3. In general, hydrodynamical simulations of galaxy clusters are fairly successful in recovering the main properties of real clusters, especially in terms of global features and predictions on the outer part of the cluster volume. However, the innermost part of simulated haloes still represent the most crucial part to model correctly, since it is particularly sensitive to the small–scale astrophysical processes, such as the interplay between cooling and feedback.

So far, hydrodynamical simulations of cosmic volumes have been usually limited to include only some basic aspects of gas physics, usually star formation and cooling, since the computational effort required to preserve very large spatial scales and follow at the same time the hydrodynamical interactions on the smaller scales can be extremely demanding. Only recently, enormous improvements in the computing facilities have allowed for pioneering campaigns of cosmological and hydrodynamical simulations of Gpc^3 volumes, including the proper treatment of several baryonic processes.

The different simulation sets used in this thesis work were originally performed with the TreePM/SPH code GADGET–2 (Springel et al., 2001; Springel, 2005) and their characteristics are described in the corresponding Chapters. In particular, we will also make use of high–resolution re–simulations of galaxy clusters, both isolated and residing in filament–like regions, in Chapter 3 and Chapter 4.

1.4   Structure of the thesis

Galaxy clusters are the primary targets of the research carried on in this thesis. In particular, we will restrict ourselves to the physics of the intra–cluster medium (ICM), with special concern for the complicated internal gas motions that could establish in the ICM and contribute to the pressure support of the whole structure. The detailed diagnostics of the ICM velocity field is in fact of great importance in the determination of their total mass, which is often estimated from X–ray observations of the hot, X–ray–emitting gas. In fact, it is crucial to assess the reliability of these mass measurements and the validity of the assumptions on which they rely, for they substantially assume the gas to be in hydrostatic equilibrium and usually account for thermal pressure only. In a

more general perspective, this could eventually help constraining the covariance among different cluster properties and calibrating scaling relations between the total mass and X–ray global observables.

This thesis is structured as follows.

Chapter 2 will be entirely devoted to present galaxy clusters, from a perspective which is foresighted for our further investigation. We aim at describing their general properties, with special concern for their X–ray observational features and for theoretical aspects that can be well studied by means of numerical, hydrodynamical simulations.

Within the second, and main, part of this work (Part II), we will address in more detail the physics of the hot diffuse gas that resides in galaxy clusters, the ICM, with the help of hydro–simulations and synthetic X–ray data obtained with a novel virtual telescope named PHOX. Our interest is particularly dedicated to the velocity field of the ICM in clusters (Chapter 3) and the non–thermal motions that can settle in the gas through their evolution history. Strongly motivated by this kind of investigation, which can be pursued in particular via high–resolution X–ray spectroscopy, we also present the description of PHOX, the X–ray photon simulator that we developed in order to obtain X–ray mock data from the output of hydrodynamical simulations and applied to study the ICM of galaxy clusters. We explicitly apply the simulator to study the thermal structure of the ICM in simulated clusters (Chapter 4) and to estimate the detectability of line shift and velocity broadening in the synthetic high–resolution spectra likely to be observed with upcoming X–ray spectrometers (Chapter 5). We summarise and draw our conclusions in Chapter 6. In Appendix A we recall the fundamental cosmological quantities utilised throughout our investigation.

Chapter 2

At the top of the hierarchy: clusters of galaxies

Clusters place themselves at the top of the hierarchical formation, as the largest gravitationally–bound structures in the Universe that had enough time to virialize. Being the highest overdensities in the cosmic matter distribution, their evolution is mainly driven by gravitation, so that they can be used as cosmological probes. Nonetheless, these systems represent optimal laboratories to study the baryonic physics which determines the formation and evolution of galaxies and their interaction. In fact, observational studies of galaxy clusters in different wavelengths continue to provide us with an increasingly complicated picture, for which a clear interpretation of the underlying physics is very challenging.

Here, we will focus in particular on the features extracted from X–ray observations that are related to cluster intrinsic structure, which can be directly investigated via numerical hydrodynamical simulations. In our analysis, we will specially concentrate on the physics of the ICM. We will devote our attention to the deviation of the ICM state from the standard assumption of Hydrostatic Equilibrium (HE), used to determine the total gravitating mass. This is, in fact, the crucial quantity required to correctly employ clusters as cosmological probes as well as to study the characteristics of the cluster population. This will be explored in particular through the analysis of non–thermal contributions to the pressure support, which are believed to derive, for instance, from turbulence and bulk motions of the hot gas. Additionally, we will introduce the leading concept of virtual X–ray simulators, developed to obtain from hydrodynamical simulations synthetic observations, which are directly and faithfully comparable to real ones.

2.1   Galaxy clusters

Already in the eighteenth century, the catalog compiled by the astronomer Charles Messier included some "nebulae" particularly clustered in a certain region of the sky, specifically in the direction of the Virgo and Coma Berenices constellations. Those aggregations of objects, afterwards known to be galaxies external to our Milky Way, are now recognised to constitute the close–by Virgo and Coma clusters of galaxies, both comprising well over a thousand of members. Despite their name, though, clusters of galaxies are more than a pure agglomeration of galaxies. Already in the 1930s, Fritz Zwicky estimated for the Coma cluster (Fig. 2.1) that a large amount of "unseen" mass has to be contained in the system in order to be able to explain the extremely high velocities of its member galaxies (Zwicky, 1937). In fact, velocity dispersions of order $\sim 500 - 1000 \, \mathrm{km/s}$ are usually measured for the galaxies moving within clusters, which imply a significantly deeper potential well with respect to what can be associated to the visible galaxies. Indeed, the dark matter (DM) does account for about $\sim 80\%$ of the total gravitating mass, while the rest is constituted by baryonic matter. The main baryonic component is the hot diffuse gas, the intra–cluster medium (ICM), while few percents of the total mass resides in the galaxies.

The total mass can be indirectly inferred from X–ray observations or directly from weak–lensing estimates, and ranges from $10^{13} \, \mathrm{M_\odot}$ for smaller groups up to $10^{15} \, \mathrm{M_\odot}$ for the richest systems. Their size is of order of few Mpc and their morphology varies according to their dynamical state. In the cosmic web, galaxy clusters reside at the nodes of the filaments, through which they can continue to accrete mass in the form, mainly, of smaller systems. Especially at higher redshift, they can be caught in the process of merging with other clusters or groups and such interacting states are often marked by elongated, asymmetric structures as well as by non–thermal signatures in the ICM, e.g. the presence of turbulence, shocks, cold fronts, streaming motions.

2.1.1   X–ray observations of galaxy clusters

X–ray observations of galaxy clusters show that they contain hot diffuse plasma (e.g. Kellogg et al., 1972). This intra–cluster medium (ICM) shares the same potential as the member galaxies and has temperatures of $10^7 - 10^8 K$, reflecting in fact the depth of the potential well ($kT \propto GM/R$). Typical number densities of the ICM are of order of
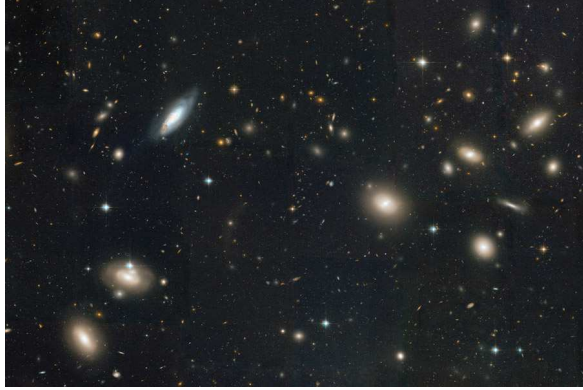
Figure 2.1: Mosaic image obtained with the Hubble Space Telescope of a small portion of the Coma galaxy cluster, which is one of the most massive and rich ones in the local Universe.
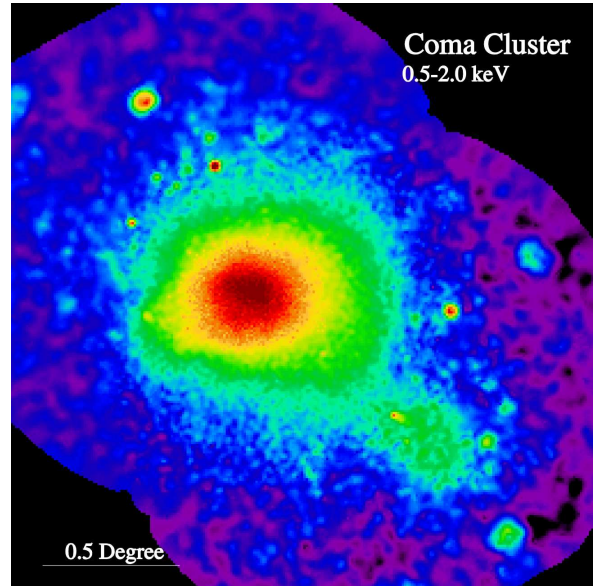
Figure 2.2: Coma cluster of galaxies in the soft X–ray band ($0.5 - 2\,\text{keV}$) obtained with the ROSAT satellite. The field is 2.7 degrees wide and 2.5 degrees high and it shows the central large, bright cluster while merging with a fainter group of galaxies, visible in the lower–right corner of the image (Credit: S. L. Snowden USRA, NASA/GSFC).

$10^{-2} - 10^{-4}\,\text{cm}^{-3}$ and therefore the plasma in clusters is in general optically thin (only in the central regions the higher density can lead to the possibility of resonant scattering at the energies of strong emission lines; see, e.g. Gilfanov et al., 1987). In the X rays, clusters of galaxies are very bright, extended sources, with luminosities of $\sim 10^{43} - 10^{45}\,\text{erg/s}$.

Given the temperatures of the ICM, hydrogen and helium are fully ionized and their ions and electrons mainly contribute to the continuum emission, dominated by free–free radiation or thermal Bremsstrahlung (Sarazin, 1988). Also free–bound or recombination processes contribute to the continuum, as well as the normally forbidden "two–photon process", i.e. the radiative transition from the $2s$ to the $1s$ state, which is allowed to happen in the ICM because of the very low densities (see, e.g. Kaastra et al., 2008; Böhringer and Werner, 2010). Galaxy cluster spectra are also characterised by emission lines, coming from the bound–bound, or de–excitation radiation of electrons changing the quantum level in ions. Emission lines are related to heavy elements, which are highly ionized and have typical abundances of about a third of their solar value. Among the various lines in the X–ray band of the spectrum, a very prominent line for galaxy clusters

is represented by the Fe K line complex around 6.7 keV.

Spectral modelling of the ICM

To the modelling of hot plasma several codes are dedicated. They mainly calculate the continuum emission and the additional radiation coming from emission lines, under the assumption of collisional ionisation equilibrium. Among others, two codes in particular are employed in our present work, that is the APEC (Astrophysical Plasma Emission Code, Smith et al., 2001) and MEKAL (after MEwe, KAastra and Liedahl, Mewe et al., 1985; Kaastra and Mewe, 1993) models, which are both incorporated within the X–ray analysis package XSPEC (Arnaud, 1996).

An example of X–ray emission, calculated according to the APEC model for collisionally–ionized plasma, is shown in Fig. 2.3 for a plasma with 0.3 solar abundance, at $kT = 5\,\mathrm{keV}$.
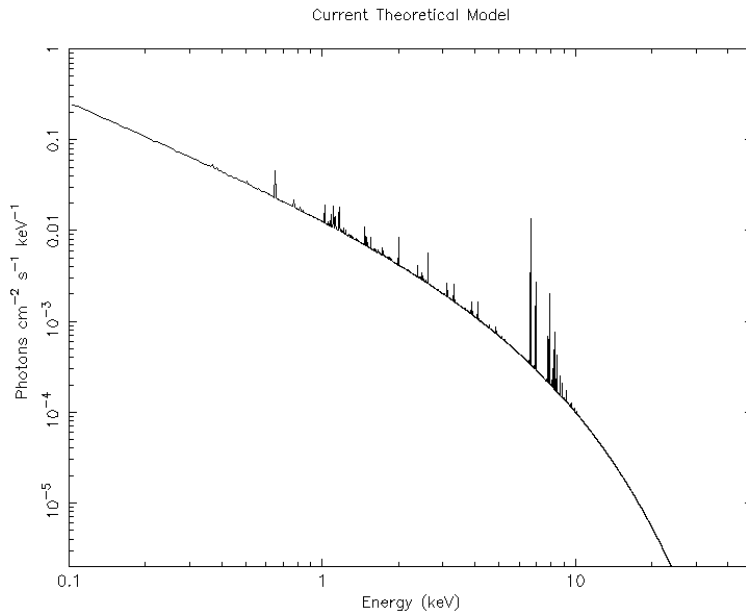
Figure 2.3: X–ray emission from a thin, collisionally–ionized plasma with 0.3 solar abundance, at $kT = 5\,\mathrm{keV}$.

Many of the global properties of galaxy clusters and also the detailed investigation of the ICM thermo–dynamical structure can be successfully explored through the analysis of the X–ray spectra.

Temperature. The temperature of the emitting plasma (kT) determines the shape

of the X–ray spectrum. This quantity is recovered from spectral fitting, that is from the comparison between the theoretical emission model, convolved with the instrumental response, and the observed data. Given the shape of the Bremsstrahlung emission, the prominent feature of the spectrum is the exponential cut–off at energies greater than kT. Therefore, it is crucial to have an instrument which is sensitive to energies greater than these in order to have a reliable determination of the plasma temperature. In general, the thermal structure of the ICM is not simply isothermal and can help constraining the complicated merging history or galaxy formation processes in clusters.

Density. The normalization of the spectrum is instead related to the density, via the emission measure of the emitting plasma, defined[1] by the volume integral

$$\text{E.M.} = \int n_e n_H dV, \tag{2.1}$$

where n_e and n_H are the electron and hydrogen number densities, respectively.

The measurement of these two quantities as function of the distance from the cluster centre allows to derive the estimation of the total mass of the cluster, via the assumptions of spherical symmetry and hydrostatic equilibrium of the ICM, and considering only the thermal component of the ICM pressure (e.g. Sarazin, 1988). Biases or uncertainties in the correct determination of pressure, i.e. of density and temperature of the ICM, can nonetheless affect such hydrostatic mass estimates up to $10 - 20\%$ and require therefore special attention (we refer to Section 2.3 for a more extended discussion).

Metal enrichment. Emission lines in the X–ray spectra come from bound–bound transitions in ionized heavy elements. The element abundances inferred from X–ray spectra of the ICM provide valuable hints on the history of metal enrichment, that is on the contribution of different supernova explosions in the stellar population to the nucleosynthesis of heavy elements.

2.1.2   Cool–cores and AGN feedback

Early X–ray observations showed that the ICM in many clusters has a sharply peaked X–ray brightness–profile and presents a drop in temperature in the central region (Fabian and Nulsen, 1977). The gas in those regions has been observed to have very high density,

---

[1]We note here that this definition is not unique. The one provided in Eq. 2.1 is commonly used in major public plasma radiation codes, such as XSPEC (Arnaud, 1996), but also the definition $EM = \int n_e^2 dV$ is sometime adopted in the literature.

which indeed could make the characteristic cooling time shorter than the Hubble time and let this gas loose energy very efficiently in the form of X–ray radiation. Indeed, this was first interpreted through the so–called "cooling–flow" model (see, e.g., Fabian, 1994). In this model the gas in the very dense central regions of massive ellipticals, groups and clusters of galaxies can radiate and cool, forming stars and diminishing the pressure support to outer ICM layers, which consequently collapse and flow inwards. However, the star formation predicted by the cooling–flow model in the centre of clusters exceeds definitely what is observable in the optical band and fails therefore to find an optical counterpart to support the picture, constituting a major problem for the model. While it is well established that cluster cores have very short cooling times and contain a smaller fraction of X–ray temperature plasma with respect to outer regions, still the amount of mass which has cooled out of the X–ray band is under debate. These clusters have been therefore called "cool–core" clusters, admitting the observational evidence without suggesting any physical explanation (Molendi and Pizzolato, 2001). Observationally, cool–core clusters show in general a more dynamically relaxed configuration with respect to non–cool–core systems, which are generally found to be more complex and disturbed.

The failure of the cooling–flow model has been also confirmed by more recent XMM and Chandra observations showing also that the ICM temperature in the innermost part of clusters is not as low as predicted, since it drops only to roughly 1/3 of the virial temperature (e.g. Peterson et al., 2001; Kaastra et al., 2001; Böhringer et al., 2001; Peterson et al., 2003). Thus, a fine–tuned mechanism is necessary in order to prevent most of the gas to cool and form stars. Moreover, since the cooling–flow problem involves a wide class of objects (from galaxies to clusters) this heating source must be able to act on very different length scales. Several candidates have been proposed to interpret the source of heat needed to overcome the cooling–flow problem, requiring a stable, fine–tuned and continuous mechanism. Among these, we recall thermal conduction and AGN heating by bubble injection and shock waves. The last mechanism, in particular, has been thoroughly investigated and agrees with the evidence that central black holes have been found in the majority of galaxies with a bulge component and seem to interact strongly with the surrounding ambient. Both observations and theory suggest different channels of AGN feedback, associated for instance with the energy release due to gas accretion onto the central black hole, bubbles of relativistic plasma, interaction between cosmic rays and

the ICM. Being able to convert very large amounts of gravitational energy into radiation, supermassive black holes are a very suitable solution as source of heating in cool–cores, where evidences for the interaction between the ICM and the AGN activity, as bubbles, radio activity and shocks, have been indeed observed (e.g. McNamara and Nulsen, 2007).

The simulator perspective. The observational evidences for a central source of heating, most likely associated to AGN activity, make the necessity of including a proper modelling of the phenomenon into numerical simulations as well. Indeed, basic hydrodynamical simulations generally fail in reproducing correctly the observed properties of the ICM in the very central part (i.e. in the region enclosed by $\sim 0.15 R_{500}$), while the expectations for the outer regions are definitely more reliable and in better agreement with observations. In fact, hydrodynamical simulations of galaxy clusters which include the cooling treatment but no proper sources of feedback definitely show an "over–cooling" problem in the cluster innermost region, where a far too large amount of stars are formed with respect to the fraction observed (e.g. Balogh et al., 2001). Thermal feedback from supernovae and a proper implementation of the multi–phase model for star formation (e.g. Springel and Hernquist, 2003) can actually partially reduce the over–cooling effect, even though it is clear that such heating source is not enough to solve completely the problem and the inclusion of AGN feedback is definitely a major goal. The challenge, however, is to reach a full comprehension of the details that characterise the balance between heating and cooling. Moreover, the degree to which other agents (e.g. thermal conduction) may contribute, together with AGN feedback, to the conversion of injected energy into heat is not yet well understood.

Several descriptions have been proposed to represent the AGN feedback model in hydrodynamical simulations, which overall helped in making the simulated galaxy clusters more realistic. Theoretical studies of suitable models for AGN heating of the ICM (e.g. Churazov et al., 2001; Brighenti and Mathews, 2003), in fact, have necessarily to be included within cosmological simulations of cluster formation, in order to properly account for the combined effect of many single episodes happening at high redshift on the proto–clusters and their progenitors. As first attempts to this goal, AGN–blown bubbles as well as interaction with cosmic rays have been, for instance, included in SPH simulation performed with the TreePM/SPH code GADGET in Sijacki and Springel (2006) and later in Sijacki et al. (2007, 2008), on the base of the model proposed by Springel et al. (2005a).

Results of these models succeeded in quenching star formation at the cluster centre and properly regulated the cooling flow, but substantially failed to consistently reproduce the central entropy profile. Following the pioneering encouraging results of those early works, more recently, alternative models for the black–hole growth and feedback mechanisms in GADGET have also been developed and discussed by Puchwein et al. (2008), Booth and Schaye (2009), McCarthy et al. (2010) and Fabjan et al. (2010). As for Eulerian AMR codes, AGN heating models have been introduced in hydrodynamical simulations of galaxy clusters and investigated by Dubois et al. (2010) and Teyssier et al. (2011).

2.2   Self–similarity: theoretical expectation

In the standard cosmological model, the haloes at different scales are expected to show a substantial self–similarity during the evolution, both in scale and in time. Galaxy clusters, therefore, are expected to fit this picture (the proper formalism for such scaling has been proposed by Kitayama and Suto, 1996). Regarding the purely dark–matter (DM) structure growth, this is indeed fairly true, as widely studied both in early theoretical studies and in simulations (e.g. Gunn and Gott, 1972). In particular, the evolution, structure and appearance of DM haloes have been shown to constitute a self–similar family from the comprehensive numerical studies carried on by Navarro et al. (1995, 1996, 1997) and prosecuted in several following works. The so–called NFW density profile (named after the names of the three authors leading the study) has been proven to be universal, fitting reasonably well all the simulated haloes over a large range in size. The expression for the NFW profile is

$$\rho_{NFW}(r) = \frac{\rho_{cr}(z)\delta_c}{\left(\frac{r}{r_s}\right)\left(1 + \frac{r}{r_s}\right)^2},   \tag{2.2}$$

with $(200/3)c^3/[\ln(1+c)-c/(1+c)]$. According to this characterisation, the population of DM haloes can be described by two parameters, namely the concentration $c = r_{200}/r_s$ and total mass (or, equivalently, time of formation). This represents the average properties of the cluster population as well, despite the possible deviations from this mean because of particular realizations of mass distribution during the formation of their DM haloes.

The introduction of baryons to the DM–only formation scenario causes a complication and a change in the description. For smaller haloes, as in the case of galaxies, baryons might be very significant in affecting the theoretical predictions made in the purely DM

scenario. Nevertheless, clusters of galaxies have the special advantage of being only mildly affected by the baryonic physics, since the DM structure is definitely dominant and the perturbation introduced by the baryonic component to the formation and evolutionary process can be considered, in general, minor. As such, the gravitational description is to first order already very useful, while the more complicated representation of small–scale hydrodynamical processes is pursued to refine better the detailed study of these systems.

Since the gas can be assumed to follow the gravitational collapse influencing it only mildly, some signatures of the self–similarity of the DM haloes must persist in its observable properties. As studied in an early work by Kaiser (1986), predictions for these relations among gas observables and total mass can in fact be derived already from the pure gravitational model of halo formation.

From the definition of a fiducial radius, corresponding to a certain overdensity Δ,

$$r_\Delta = \left(\frac{3M_{cl,\Delta}}{4\pi\Delta\rho_{cr}} \right)^{1/3} \tag{2.3}$$

we already obtain the correlation expected between size and mass, M_{cl}, (both calculated for the overdensity Δ) of the cluster and its scaling with time (redshift),

$$r_{\Delta(z)} \propto M_{cl,\Delta}^{1/3} E(z)^{-2/3} \Delta(z)^{-1/3} \tag{2.4}$$

expressing the dependance on the underlying cosmology through the $E(z)$ function [2].

Also the temperature can be related to the total mass, starting from the consideration that it must reflect the potential energy converted into heating during the collapsing process:

$$T \propto \left(\frac{M_{cl,\Delta}}{r_{\Delta(z)}} \right) \propto M_{cl,\Delta}^{2/3} E(z)^{2/3} \Delta(z)^{1/3}. \tag{2.5}$$

Similarly, one can derive other correlations involving X–ray observables. Among those, the most common ones are, e.g.

- X–ray luminosity[3] ($L_X - T$ relation)

$$L_X \propto \rho_{cl}^2 T^{1/2} r_{\Delta(z)}^3 \propto T^2 E(z) \Delta(z)^{1/2}$$

  wherein the emission has been assumed to be $\propto \rho^2 T^{1/2}$, as for thermal bremsstrahlung.

---

[2]In the general case where more than one component of the cosmic fluid is considered (e.g. ordinary matter, radiation and Cosmological Constant) one can write, for the evolution of the Hubble constant,

$$H(z)^2 = H_0^2 \left[(1 - \Omega_{0,tot})(1+z)^2 + \Sigma\Omega_{0,w_i}(1+z)^{1-3w_i} \right] \equiv H_0^2 E^2(z)$$

wherein each component is denoted by its equation–of–state parameter, w_i, and density parameter at present epoch, Ω_{0,w_i}.

[3]Here L_X is defined as the *bolometric* X–ray luminosity and is usually calculated over the entire band, in contrast to the X–ray luminosity calculated in a narrow energy band.
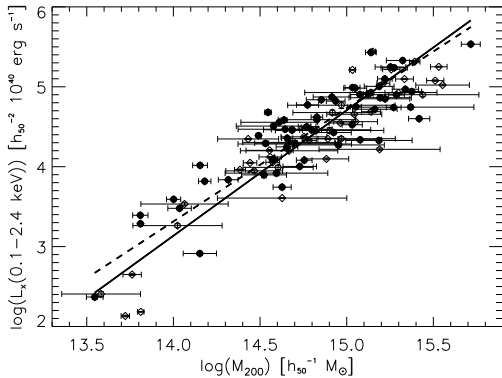
Figure 2.4: $L_X - M$ scaling relation for a sample of X–ray selected clusters. The gravitational mass is calculated within M_{200}. Figure from Reiprich and Böhringer (2002).
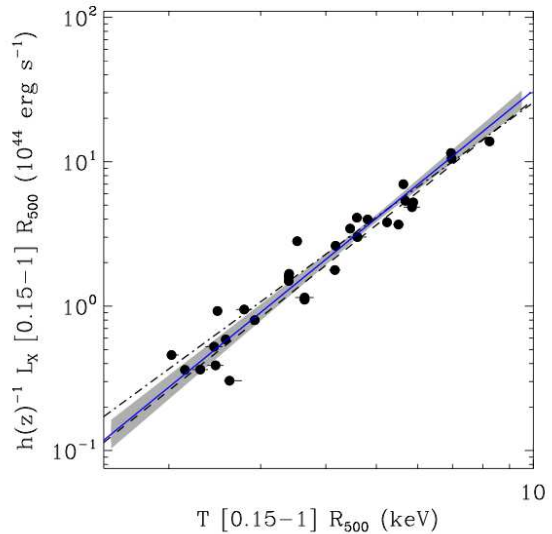
Figure 2.5: $L_X - T$ scaling relation for clusters in the REXCESS sample. Both luminosity and temperature have been calculated by excluding the innermost region of the clusters, i.e. considering only the $0.15R_{500} < R < R_{500}$ region. Figure from Pratt et al. (2009).

- entropy ($S - T$ relation)

$$S \propto \frac{T}{\rho_{cl}^{2/3}} \propto TE(z)^{-4/3}\Delta(z)^{-2/3}$$

- gas mass ($M_{gas} - T$ relation)

$$M_{gas} \propto \rho_{cl}r_{\Delta(z)}^3 \propto T^{3/2}E(z)^{-1}\Delta(z)^{-1/2}$$

These are the predicted slopes for self–similarity, as derived within the purely gravitational formalism.

2.2.1   Observed X–ray scaling relations

Observations in the X–ray band offer the tool to measure gas properties such as luminosity, temperature, entropy, gas mass fraction, and permit to infer the total mass as well. Thus, it is straightforward to investigate to which degree the X–ray scaling relations agree with theoretical and numerical predictions from the gravitational formation model.

Indeed, clusters of galaxies can span quite large ranges in temperature, luminosity, gas mass fraction and total mass, but they do not occupy the entire parameter space of

physical properties and rather define clear correlations among these observable features. Several works, based on data from different X–ray instruments and for various X–ray selected samples of galaxy clusters, are dedicated to obtain X–ray scaling relations. Two well–known observational results for the $L_X - M$ and $L_X - T$ X–ray scaling relations are shown in Fig. 2.4 (from the work by Reiprich and Böhringer, 2002) and Fig. 2.5 (from Pratt et al., 2009).

Differences with respect to the self–similar scaling predicted from the gravity–dominated collapse are observed in real clusters. For instance, the general trend for the $M_{gas} - T$ and $L - T$ relations shows a steeper logarithmic slope than expected. The main differences with respect to predictions are most likely introduced by hydrodynamical processes, especially significant in the innermost part of clusters. In fact, in Fig. 2.5 the moderately reduced scatter is obtained by excluding the very central part ($< 0.15R_{500}$) of the clusters of the REXCESS sample utilized for the study. Certainly, the effects introduced by the observational process as well as the intrinsic covariance among the X–ray properties of the ICM (e.g. Nord et al., 2008; Stanek et al., 2010) can additionally affect the resulting relations and are definitely worth of deeper investigation. Furthermore, non–thermal processes also contribute to bias the estimated mass (up to $\sim 10 - 20\%$), determining an additional source of uncertainty in X–ray scaling relations. It is important, in this context, to precisely estimate the total gravitating mass, especially in the case of X–ray–based estimates.

2.3   Non–thermal motions in the ICM

The assumption usually made about the ICM in regular, relaxed galaxy clusters is that the gas is in hydrostatic equilibrium. The Hydrostatic Equilibrium Hypothesis (HEH) has a fundamental importance, for instance, for X–ray–based mass estimates (e.g., see Sarazin, 1988), which still constitute one of the best and most commonly adopted methods to infer the total gravitating mass of galaxy clusters. Under hydrostatic equilibrium:

$$\frac{dP_{gas}}{dr} = -\frac{GM(<r)\rho_{gas}(r)}{r^2} \tag{2.6}$$

From which, assuming spherical symmetry for the gas and only thermal motions to contribute to the gas pressure P_{gas},

$$M_{hyd}(< r) = -\frac{k_B T r}{G \mu m_p} \left(\frac{d \ln \rho_{gas}}{d \ln r} + \frac{d \ln T_{gas}}{d \ln r} \right). \qquad (2.7)$$

Clearly, such hydrostatic mass estimates strongly rely on the assumptions made about the dynamical state of the galaxy cluster, for which the non–thermal contributions to pressure (e.g. due to turbulence, streaming and bulk motions, and rotational patterns) are usually neglected in Eq. 2.7 (Rasia et al., 2004; Fang et al., 2009).

Significant non–thermal motions are indeed expected to establish in the ICM of galaxy clusters, not only in disturbed systems undergoing major mergers, which obviously cannot be classified as relaxed (see, e.g., numerical studies by Fang et al., 2009; Lau et al., 2011), but also in cases where small merging events occur in the central region, like the close–by passage of gas–rich substructures, which is deeply investigated with the help of hydrodynamical, numerical simulations in Chapter 3. Furthermore, both simulations and observations of galaxy clusters suggest that turbulence, magnetic fields and cosmic rays (e.g. Dolag and Schindler, 2000; Dolag et al., 2005; Bonafede et al., 2010) are almost certainly significant in the ICM and are likely to contribute as well to the total pressure support, consequently affecting the total mass estimate. Numerically, the importance of all these non–thermal contributions has been investigated both in the cluster core region (Fang et al., 2009; Lau et al., 2011) and in the outskirts (Parrish et al., 2011; Vazza et al., 2009), where a significant part of the total gravitating mass resides and it is therefore crucial to make very precise measurements. In general, Eulerian and Lagrangian high–resolution simulations of galaxy clusters agree in suggesting that a sizable amount of pressure support can be due to chaotic motions.

Ideally, one should be able to detect and estimate such non–thermal contribution from real observations, in order to properly account for them in the total pressure budget,

$$P_{tot} = P_{thermal} + (P_{turb} + P_{CR} + P_{rot} + P_{stream} + P_{mag}), \qquad (2.8)$$

and correctly derive the total gravitating mass from X–ray observables.

Better constraints on the detailed ICM thermo–dynamical structure are also fundamental to evaluate correctly the global properties of X–ray clusters, involved directly in the determination of the total mass. Complicated thermal structures, for instance,

should be carefully accounted for in order to reconstruct the radial temperature profile utilised in Eq. 2.7. Especially, only very few, recent observational studies have managed to provide meaningful measurements of the ICM temperature out to and beyond R_{500}[4], where a significant part of the cluster volume is contained. The outer part of galaxy clusters, though, is very crucial to probe, since it is expected to play a key role in the understanding of the assembly process, occupying the region where the accretion of pristine gas is most–likely still in place. Besides, a number of factors are still competing to the degeneracy of the information that can be extracted from X–ray observations of the ICM, e.g. the spatial distribution and mixing of metals that enrich the hot gas, the thermal conduction affecting the temperature structure of the cluster and the already mentioned motions of the gas.

Hence, it is crucial to constrain the conditions under which the HEH does hold for real clusters and evaluate the origin and level of deviation from the hydrostatic equilibrium as precisely as possible.

2.3.1 Constraining the ICM velocity field

A number of processes ongoing in clusters of galaxies, such as the sloshing of DM cuspy cores that may take place in cluster innermost regions or the central AGN activity, are likely to transfer energy from the larger scales into the thermal and kinetic energy of the ICM, representing various potential sources of turbulence.

From the observational point of view, measurements of the Faraday Rotation of the polarization angle of the synchrotron emission from cluster radio galaxies suggests the presence of turbulent motions in the ICM (see, e.g., Bonafede et al., 2010). Certainly, a deeper understanding of the turbulence velocity field in the ICM can be precious to constrain the turbulent heating rate in clusters and clarify the role of gas motions in the particle acceleration process.

Likewise, X–ray observations have attempted to provide independent hints on the ICM velocity field associated to non–thermal motions such as turbulence. Such observational studies are based, for instance, on measurements of distortions of X-ray surface brightness (Churazov et al., 2011) or of fluctuations in the pressure maps of the core region of nearby clusters, which can be obtained from X–ray telescopes. As a seminal work of this

---

[4]This is defined as the radius enclosing a density of 500 times the critical density of the Universe, and is $\sim 0.7R_{200}$, where R_{200} defines approximately the virial radius.
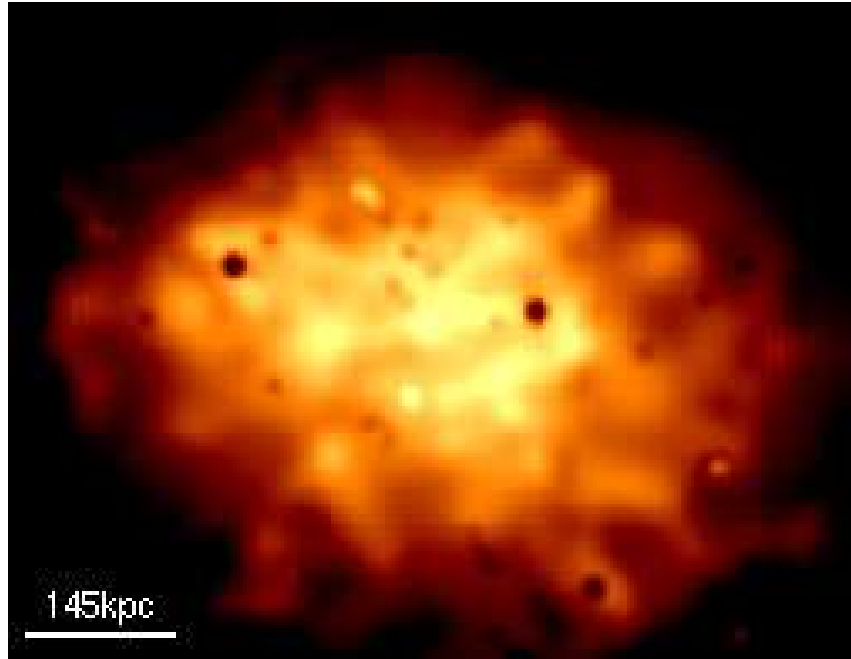
Figure 2.6: Map of the projected pressure distribution in the central part of the Coma cluster, obtained from XMM-Newton observations. The scale reported on the map refers to the estimated, largest size of the turbulent eddies. Figure adopted from Schuecker et al. (2004).

kind, constraints on the spectrum of pressure fluctuations of the hot gas in the central region of the Coma cluster were obtained by Schuecker et al. (2004) from XMM–Newton observations (see Fig. 2.6), suggesting the spectrum to be roughly in agreement with a Kolmogorov power law with a contribution of $\sim 10\%$ due to turbulence. This, in particular, is also indicated by hydrodynamical simulations, which uniquely provide us with precise information on the intrinsic, 3D velocity structure in clusters (Dolag et al., 2005; Iapichino and Niemeyer, 2008; Iapichino et al., 2011; Vazza et al., 2009, 2011). A visualization of the gas velocity field for an AMR simulation of a galaxy cluster is shown in Fig. 2.7 (from Vazza et al., 2009). Both AMR and SPH simulations seem to suggest the spectrum for the turbulent velocity to be similar to a Kolmogorov spectrum, as well, even though the findings are still largely debated.

So far, however, only indirect indications of ICM turbulent velocities have been obtained, because of the still lacking high energy resolution required to directly detect turbulent motions from X–ray data. Only with the XMM RGS (Reflection Grating Spectrometer) has it been possible to place direct upper limits on the velocity amplitude, for a set of clusters, groups and elliptical galaxies (Sanders et al., 2011). A comparison
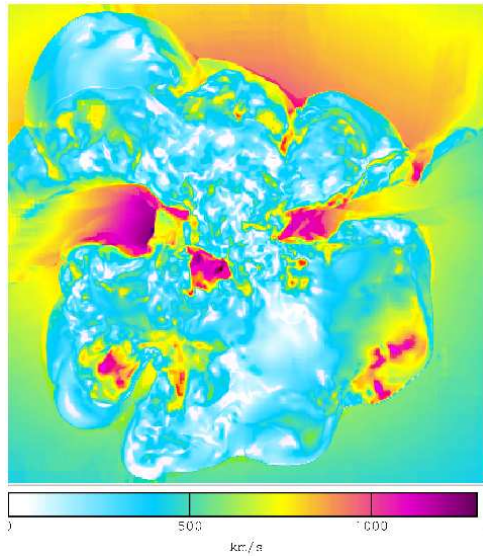
Figure 2.7: The map, with side of 7.5 Mpc and depth of 18 kpc, shows the gas velocity field for an AMR simulation of a galaxy cluster. Figure adopted from Vazza et al. (2009).
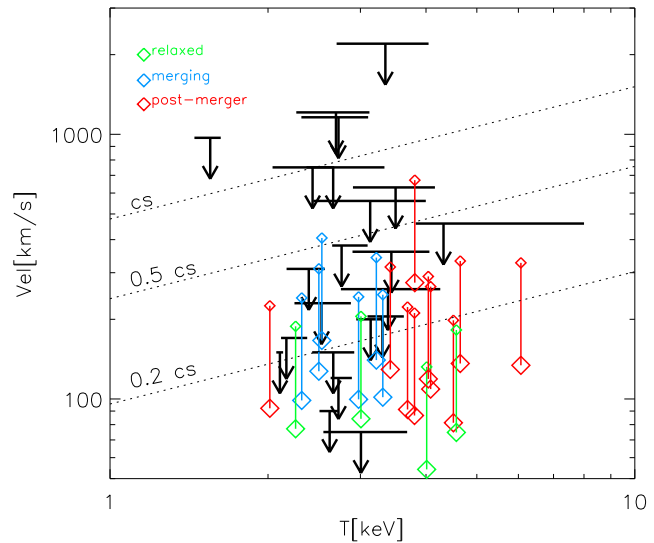
Figure 2.8: Mean velocity dispersion as function of temperature for the set of simulated clusters studied in Vazza et al. (2011) and for the clusters observed with XMM–Newton by Sanders et al. (2011). Figure adopted from Vazza et al. (2011).

between AMR simulations of galaxy clusters and such observational limits to the turbulent velocity amplitude is discussed by Vazza et al. (2011), as shown by Fig. 2.8.

In general, X–ray spectrometry potentially offers a very promising way to detect and quantify such velocity structures in the ICM, provided that high–precision spectra become available. This will be reached with upcoming X–ray instruments like ASTRO–H or ATHENA, for which the spectroscopic resolution is expected to reach a few eV at $\sim 6\,\mathrm{keV}$.

Several theoretical studies propose to focus on the centroid shift, broadening and shape of highly–energetic spectral emission lines from heavy ions, as a direct source of information on the gas velocity field (e.g. Sunyaev et al., 2003; Inogamov and Sunyaev, 2003). In fact, X–ray lines emitted by ions with large atomic weight, like the He–like iron line at $\sim 6.7\,\mathrm{keV}$, are particularly sensitive to velocity broadening, with respect to the thermal contribution, and could help therefore to detect gas turbulent, streaming or rotational motions in galaxy clusters (see also Dolag et al., 2005; Rebusco et al., 2008). Additionally, promising results rely on the possibility to use the resonant scattering effect (see, for a recent review, Churazov et al., 2010), which might characterise the brightest X–ray emission lines, as the He–like iron line at $\sim 6.7\,\mathrm{keV}$. Indeed, for such resonant lines, the thin–plasma approximation (valid in the X–ray regime) can be violated, since the

optical depth for purely thermal broadening of the line can be larger than unity, causing detectable effects on surface brightness distribution but also changes in the shape and polarization of the emission lines themselves. All these effects are sensitively dependent on the turbulent broadening of the lines, making resonant scattering extremely powerful not only to give precise information on the temperature and density structure of the gas, but also to probe the amplitude of the gas velocities (Churazov et al., 2010; Zhuravleva et al., 2010).

Even though enormous progress has been made in the field of X–ray observations, biases and uncertainties are still under debate, especially when the observational results are attempted to be compared to theoretical expectations and hydrodynamical simulations of cluster–like objects.

2.4 Towards a detailed comparison between observations and numerical simulations

As already suggested, the gravitation–only semi–analytical approach cannot properly account for perturbative effects due to the baryonic physics in galaxy clusters, which, although minor, should be ultimately taken into account. This is the main motivation to make use of numerical simulations, which represent a powerful tool to push the investigation further (beyond analytical modelling) and explore the expected structure of galaxy clusters and of their ICM.

The results obtained for simulated galaxy clusters, however, are not easily comparable to observations in a direct and faithful way. For instance, the simulated data offer the unique advantage of unveiling unambiguously the three–dimensional structure of the cluster, which in real observations would be hidden by projection effects. Similarly, the total gravitating mass of the simulated systems can be precisely measured by directly summing up the masses of the single member particles or grid cells. Moreover, while the observed galaxy clusters are captured in a certain configuration and hints on the evolution can only be inferred indirectly or via statistical studies at different redshifts, numerical simulations provide a detailed record of all the evolutionary process from the initial perturbations to the final, collapsed halo of the cluster. Basically, the significant difference is that no instrumental effects intervene to bias and limit what can be measured of the intrinsic quantities characterising the system. If on one hand, the possibilities

offered by hydrodynamical simulations of clusters are therefore numerous and precious, on the other hand the conclusions drawn from them is limited to the theoretical modelling of the understood physics and it is somehow difficult to make the ultimate step towards clusters as they really appear in the Universe.

2.4.1 Virtual X–ray telescopes for hydrodynamical simulations

A significant effort has been made in order to provide tools able to suite simulation outputs in a fashion as much as possible similar to real observations, to which the final word on the nature of galaxy clusters belongs. To this scope, simulators like X–MASS/X–MASS2 (Gardini et al., 2004; Rasia et al., 2008) or XIM (Heinz et al., 2010), have been developed in order to obtain synthetic X–ray observations from hydrodynamical simulation outputs, which can be compared in the most direct and faithful way possible to real X–ray observations. The approach adopted so far in these virtual X–ray simulators, as X–MASS or XIM, starts from the choice of the particular geometry of the synthetic observation, *in primis* the line of sight (l.o.s.) direction. Once this projection step is done, the emissivity is calculated per each gas volume (SPH particle for X–MASS or grid cell for XIM) and integrated along the l.o.s.. Finally, the resulting spectral data cube (basically a spectrum per each sky cell) is convolved with an instrumental response, which provides information on the effective area and efficiency of the selected X–ray instrument as function of energy. These simulators usually rely on a library of model spectra, ranging over a grid in the parameter space of temperature, density and metallicity, whose expanse is consequently confined because of memory requirements.

For galaxy clusters, the possibility to obtain a real–like observation corresponding to the simulated data is of extreme importance, since it allows us to consistently test methods dedicated to extract reliable information on their intrinsic nature from observable X–ray properties. Moreover, this permits to calibrate biases on the inferred quantities that are possibly introduced by wrong assumptions on the cluster dynamical state or on the thermo–dynamical structure of the hot, emitting gas, like those affecting total mass estimations. A number of interesting results has been achieved with this investigation method: useful constraints have been set on the temperature profile of clusters (e.g. Mazzotta et al., 2004; Rasia et al., 2004, 2006) and on the differences between various definitions of the ICM temperature, from the comparison between the value inferred

from X–ray spectral fitting and the different values calculated from the simulation output directly, e.g. mass–, emission– or EM–weighted temperature.

The perspectives for the near future, both from observational and numerical sides, suggest an increase in the amount and in the richness of details that will become available to describe galaxy clusters. Huge cosmological, hydrodynamical simulations of Gpc^3 volumes will indeed provide us with vast catalogs of simulated clusters, as well as with simulations of large–scale structures, well resolved in space and simulated accounting for many physical processes, e.g. accretion onto black holes, AGN feedback, star formation, chemical enrichment following several species, metal and molecule cooling, magnetic fields, to name some. Synthetic observations of such outputs will also have to guarantee high spatial and spectral resolution, in order to keep the pace with up–coming X–ray observatories, expected to achieve high energy resolution, as in the case of ASTRO–H or Athena. In addition, the possibility to use these tools on vast statistical samples will be crucial in order to take full advantage of all–sky surveys, as eRosita, that will increase enormously the statistics on clusters, optimal for scaling relations and population studies.

To these purposes a successful simulator has necessarily to combine the possibility of processing efficiently very large datasets, within reasonable time scales, with the capability to account without undue difficulty for many physical parameters describing the X–ray emitting plasma, provided by the input simulations. At the same time, high spatial and spectral resolution for the mock emission would be an important goal to pursue, likewise. To this subject we will dedicate Chapter 4.

Part II

The physics of the intracluster medium

Chapter 3

Velocity structure diagnostics of simulated galaxy clusters

Veronica Biffi, Klaus Dolag & Hans Böhringer

Gas motions in the hot intracluster medium of galaxy clusters have an important effect on the mass determination of the clusters through X–ray observations. The corresponding dynamical pressure has to be accounted for in addition to the hydrostatic pressure support to achieve a precise mass measurement. An analysis of the velocity structure of the ICM for simulated cluster–size haloes, especially focusing on rotational patterns, has been performed, demonstrating them to be an intermittent phenomenon, strongly related to the internal dynamics of substructures. We find that the expected build–up of rotation due to mass assembly gets easily destroyed by passages of gas–rich substructures close to the central region. Though, if a typical rotation pattern is established, the corresponding mass contribution is estimated to be up to $\sim 17\%$ of the total mass in the innermost region, and one has to account for it. Extending the analysis to a larger sample of simulated haloes we statistically observe that (i) the distribution of the rotational component of the gas velocity in the innermost region has typical values of $\sim 200 - 300 \, \mathrm{km/s}$; (ii) except for few outliers, there is no monotonic increase of the rotational velocity with decreasing redshift, as we would expect from approaching a relaxed configuration. Therefore, the hypothesis that the build–up of rotation is strongly influenced by internal dynamics is confirmed, and minor events like gas–rich substructures passing close to the equatorial plane can easily destroy any ordered rotational pattern.

3.1 Introduction

Within the hierarchical structure–formation scenario, galaxy clusters are key targets that allow us to study both the dynamics on the gravity–dominated scale and the complexity of astrophysical processes dominating on the small scale. In such studies their mass is one of the most crucial quantities to be evaluated, and the bulk properties measured from X–ray observations still provide the best way to estimate the mass, primarily on the assumption of hydrostatic equilibrium (Sarazin, 1988). Mass estimates rely then on the assumptions made about the cluster dynamical state, since the Hydrostatic Equilibrium Hypothesis (HEH) implies that only the thermal pressure of the hot ICM is taken into account (Rasia et al., 2004). Lately, it has been claimed in particular that non–thermal motions, as rotation, could play a significant role in supporting the ICM in the innermost region (e.g. Lau et al., 2009; Fang et al., 2009) biasing the mass measurements based on the HEH. The analysis of simulated cluster–like objects provides a promising approach to get a better understanding of the intrinsic structure of galaxy clusters and the role of gas dynamics, which can be eventually compared to X–ray observations. Because of the improvement of numerical simulations, the possibility to study in detail the physics of clusters has enormously increased (see Borgani and Kravtsov, 2009, for a recent comprehensive review) and future satellites dedicated to high–precision X–ray spectroscopy, such as ASTRO–H and IXO, will allow to detect these ordered motions of the ICM. With this perspective, we perform a preliminary study on the ICM structure for some clusters extracted from a large cosmological hydrodynamical simulation, investigating in particular the presence of rotational motion in the ICM velocity field.

The paper is organized as follows. We describe the numerical simulations from which the samples of cluster–like haloes have been selected in Section 3.2. In Section 3.3 we consider a first set of simulated clusters and present results on build–up of rotation in the halo core for single cases of study (Section 3.3.1 and Section 3.3.2), while results about the contribution to the mass estimations are given in Section 3.4. A second sample of clusters is then statistically investigated in Section 3.5. We discuss our results and conclude in Section 3.6.

Appendix A is devoted to comment on the effects of artificial viscosity, while in Appendix B we briefly comment on the ellipticity profiles of the simulated clusters.

3.2   Numerical Simulations

We consider two sets of cluster–like haloes selected from two different parent cosmological boxes. In both cases the cosmological simulations were performed with the TreePM/SPH code GADGET–2 (Springel et al., 2001; Springel, 2005), assuming a slightly different cosmological model (a standard ΛCDM model and a WMAP3 cosmology, respectively) but including the same physical processes governing the gas component (Springel and Hernquist, 2003), i.e. radiative cooling, star formation, and supernova feedback (*csf* simulation, see Dolag et al. (2009) and references therein for a more detailed overview on different runs of the parent hydrodynamical simulations we refer to in our work). Additionally, we refer to simulations of the same objects without including radiative processes as *ovisc*.

Set 1. The first data set considered consists of 9 cluster–size haloes, re–simulated with higher resolution using the "zoomed initial condition"(ZIC) technique (Tormen et al., 1997). The clusters have been originally extracted from a large–size cosmological simulation of a ΛCDM universe with $\Omega_0 = 0.3$, $h = 0.7$, $\sigma_8 = 0.9$ and $\Omega_b = 0.039$, within a box of $479h^{-1}$ Mpc a side. The final mass–resolution of these simulations is $m_{DM} = 1.13 \times 10^9 h^{-1}$ M$_\odot$ and $m_{gas} = 1.69 \times 10^8 h^{-1}$ M$_\odot$, for the DM and gas particles, respectively. The spatial resolution for Set 1 reaches $5h^{-1}$ kpc in the central parts and for the most massive clusters we typically resolve up to 1000 self–bound sub–structures within R_{vir} (as shown in Dolag et al., 2009). The main haloes have masses larger than $\sim 1.1 \times 10^{14} h^{-1}$ M$_\odot$ and they have all been selected in a way that they are quite well–behaved spherically–shaped objects at present epoch, although a fair range from isolated and potentially relaxed objects to more disturbed systems embedded within larger structures is available. Having a reasonable dense sample within the time domain (e.g. 50 outputs between $z = 1$ and today) and high resolution, we can study how common and significant the rotational support of the ICM is. In particular we focus on the detailed evolution of such rotational motions.

Set 2. In the second data set we analyzed a volume limited sample of cluster–size haloes, where we computed the distribution of the ICM rotational velocity and compared their distribution at different redshift. This second set of clusters has been extracted from a large size cosmological simulation with a box–size of $300h^{-1}$ Mpc, simulated with

2×768^3 particles, assuming the 3–year WMAP values for the cosmological parameters (Spergel et al., 2007), i.e. $\Omega_0 = 0.268$, $\Omega_b = 0.044$, $\sigma_8 = 0.776$ and $h = 0.704$. The final mass–resolution for this second set of simulations is $m_{DM} = 3.71 \times 10^9 h^{-1}\,\mathrm{M}_\odot$ and $m_{gas} = 7.28 \times 10^8 h^{-1}\,\mathrm{M}_\odot$. Given the larger sample, a fair investigation of the amount of rotational support within the ICM from a statistical point of view is then possible.

The two sets of simulations analyzed were performed with a different value of σ_8, meaning that differences in the merging histories can be introduced. Nevertheless, we stress that the purpose of the second set is only to enlarge the statistics on the build–up of rotational motions in simulated galaxy clusters, and not a direct comparison of single objects to the objects of Set 1. Therefore, we are confident that our conclusions do not depend on these differences in the parameters of the two simulations.

3.3 Velocity structure of the ICM

In the first place, we have been investigating the velocity structure of the ICM for all the main haloes of the Set 1, looking for evidence of rotational patterns in the most central regions of the simulated clusters, especially for the most massive haloes.

Although a variety of objects is offered (ranging from more complex structures sitting in a denser environment to quite isolated haloes), all the cluster-like haloes have been originally selected to be fairly regularly shaped. For this aspect, the whole Set 1 is biased towards quite relaxed clusters and we would expect to find a more significant amount of rotation than on average. Among the four most massive systems, for which Fig. 3.1 gives the X–ray surface brightness maps in the three projected directions, we identify as the most relaxed clusters g51 and g8, while g1 and g72 are disturbed systems still suffering at the present epoch from recent major mergers

An indication of this differences is clearly shown in Fig. 3.2, where we plot the mass accretion history for the main progenitor of each cluster as function of redshift. The curves referring to g51 and g8 (solid black line and dotted blue line, respectively) show a smoother mass assembly (at late times, i.e. $z \lesssim 0.3$) if compared with those for g1 and g72 (dashed green line and dot–dashed light–blue line, respectively), whose curves show bumps related to major merging events down to very low redshift. In addition, a visual inspection of the X–ray surface brightness maps presented in Fig. 3.1 definitely suggests
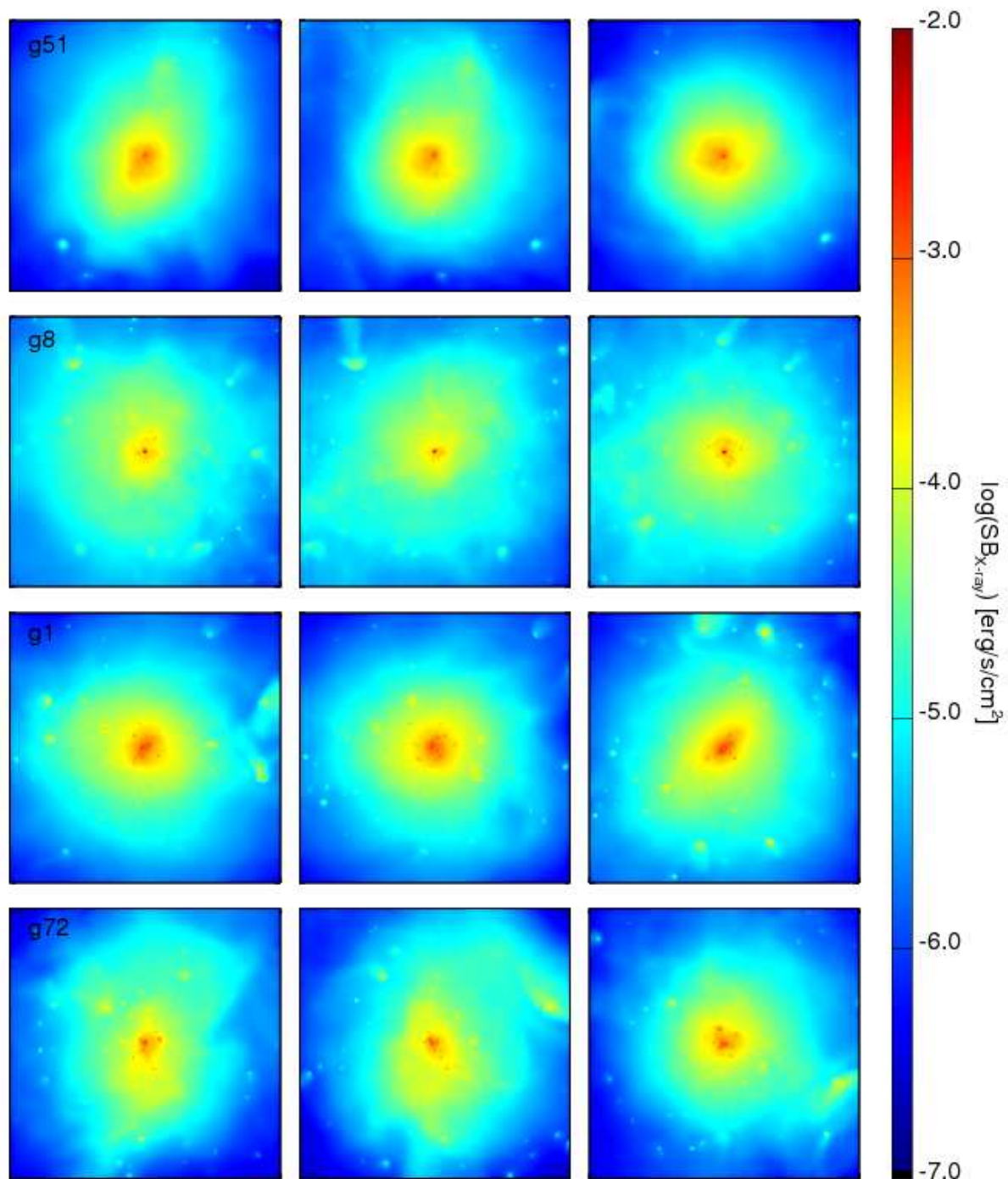
Figure 3.1: X–ray surface brightness maps along the three projection axis for the four most massive cluster–like haloes in Set 1 (from top to bottom: g51, g8, g1, g72). Each map is 2 Mpc–side, enclosing therefore the region of about $\sim R_{500}$.
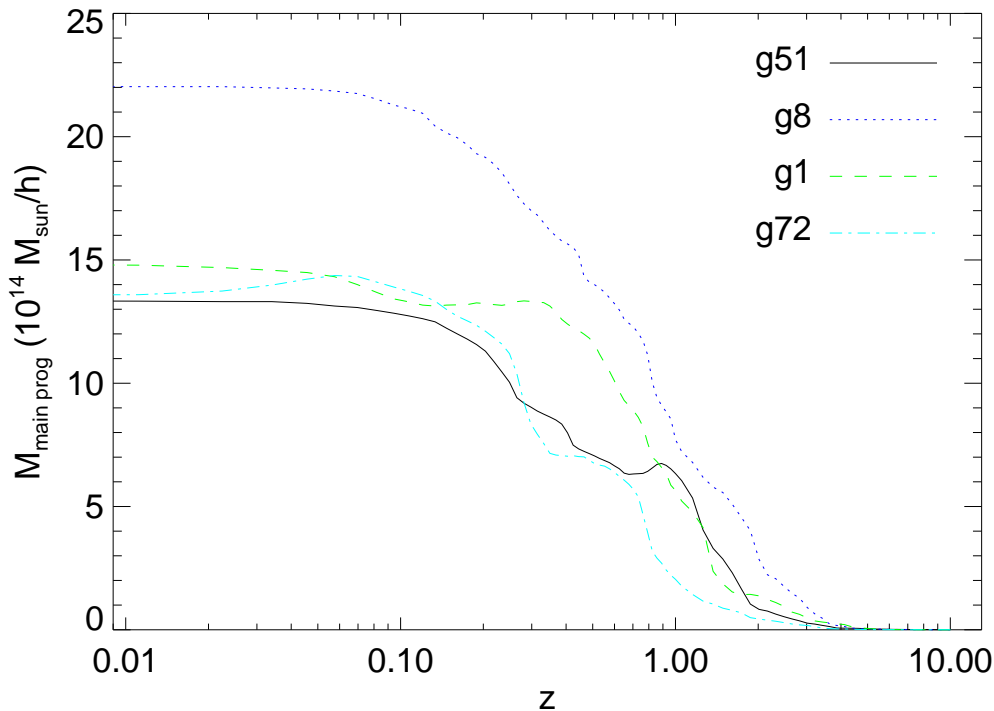
Figure 3.2: Main halo mass accretion history for the four most massive clusters in Set 1: g51 (solid, black line), g8 (dotted, blue), g1 (dashed, green), and g72 (dot–dashed, light–blue). The mass of the main halo is plotted in units of $10^{14}h^{-1}\,\mathrm{M}_{\odot}$ as function of redshift.

g51 to be the less sub-structured halo.

In this perspective, we address g51 as the best case of study to explore the build–up of rotational motions in the cluster central region as a consequence of the cooling of the core. Among the other clusters also g1 shows interesting features in its velocity field that are worth to be investigated in more detail and compared to the case of g51 to better characterize the occurrence of ordered rotational motions in the intracluster gas (see Appendix 3.7.2 for a comment on the isophote ellipticities of g51 and g1 among the four most massive haloes from Set 1 and how the gas shapes relate to intrinsic rotational gas motions).

3.3.1 Rotational patterns in the ICM

The two cases analyzed in detail (the isolated regular cluster, g51, and the disturbed massive halo g1) are particularly interesting for our purpose, since their velocity structure at redshift $z = 0$ shows two opposite pictures, namely strong rotational patterns for g1 and almost no gas rotation for g51.

In the classic cooling flow model, gas rotation is expected near the center of the flow because of mass and angular momentum conservation (e.g. Mathews and Brighenti, 2003). Though, the rate of cooling gas predicted by the classical paradigm of cooling flows is rarely observed in real clusters, implying that feedback processes must play a role in preventing cooling (McNamara and Nulsen, 2007). In contrast, in simulations, the strong cooling in the central region of the simulated cluster–like haloes suggests that relaxed objects should build up significant rotational motion in the innermost region where gas is infalling and contracting under the conservation of angular momentum. As reported in the literature (e.g. Fang et al., 2009) this effect is expected to be particularly evident in simulated clusters that can be identified as relaxed objects. Therefore it is interesting to point out that, in our sample, not even in the object with the smoothest accretion history and less substructured morphology significant rotational patterns establish in the ICM velocity structure as a consequence of collapse.

Dealing with hydrodynamical simulations though, the build–up of rotation in the central region of clusters can be also enhanced by an excess of gas cooling that has been found to overproduce the observed cosmic abundance of stellar material (e.g Katz and White, 1993; Balogh et al., 2001) in absence of very strong, not yet fully understood feedback processes. In our simulations, the implementation of a multi–phase model for star formation (e.g. Katz et al., 1996; Springel and Hernquist, 2003) and the treatment of the thermal feedback process, including also galactic winds associated to star formation, is able to partially reduce the over–cooling problem (Borgani et al., 2006). This fact plausibly contributes to prevent significant rotation.

In order to study in detail the rotational component of the ICM velocity for a halo, we first define a "best equatorial plane" on which we can calculate the tangential component of the velocity, v_{tan}. This plane is taken to be perpendicular to the direction of the mean gas angular momentum, $\mathbf{j}$, calculated averaging over the gas particles within the region

where we want to investigate the rotational motion within the ICM, i.e. $< 0.1 R_{500}$ (here, the overdensity of 500 is defined with respect to the critical density of the Universe). This definition of the "best equatorial plane" allows us to emphasize and characterize the rotation of the gas in an objective way for all clusters, whenever it appears.

To perform our analysis, we rotate the halo such that the new z–axis is aligned with the direction of $\mathbf{j}$ and the new xy plane easily defines the best equatorial plane. After subtracting an average bulk velocity for the gas component within the region corresponding to R_{500}, we compute the tangential component of the velocity on this plane. We consider a $40 h^{-1}$ kpc slice of the simulation box containing this plane for all the calculations hereafter.

3.3.2 A case study: g51 vs. g1

As a case study, we particularly focus on g51, an isolated massive cluster with gravitational mass of $M_{200m} = 1.34 \times 10^{15} h^{-1} \, \mathrm{M_\odot}$ and a size of $R_{200m} = 2.28 h^{-1} \, \mathrm{Mpc}$ at $z = 0$, and we compare it with the other extreme case mentioned, g1, which is instead a strongly disturbed system with $M_{200m} = 1.49 \times 10^{15} h^{-1} \, \mathrm{M_\odot}$ and $R_{200m} = 2.36 h^{-1} \, \mathrm{Mpc}$. Here, R_{200m} is defined as the radius enclosing the region with density equal to 200 times the mean density of the Universe, and M_{200m} is the mass within R_{200m}. M_{200m} has been used throughout our study as reference quantity to select haloes, but we always carry out our calculations by referring to R_{500} and M_{500}, where the overdensity of 500 is instead defined with respect to the critical density of Universe, motivated by a possible comparison to real X–ray observations. In the case of g51 and g1, we have $R_{500} = 1.09, 1.20 h^{-1} \, \mathrm{Mpc}$ and $M_{500} = 7.46 \times 10^{14}, 9.98 \times 10^{14} h^{-1} \, \mathrm{M_\odot}$ respectively, at $z = 0$.

From the considerations made in Section 3.3 about its shape and accretion history, g51 is likely to be, in a global sense, the most relaxed object in the sample. In spite of this, at $z = 0$ the velocity structure of the ICM in the innermost region is far from showing a clear rotational pattern as expected from a nearly homogeneous collapse process. However it shows some rotational pattern at intermediate redshift.

In Fig. 3.3 we plot the rotation velocity profile, $v_{tan}(r)$, for the two interesting cases (at $z = 0$) out to R_{500}. As explained in the previous Section, v_{tan} is the tangential component of the ICM velocity, calculated in the best equatorial plane. In order to compute the radial profile displayed in Fig. 3.3, we make use of radial bins in the plane to calculate
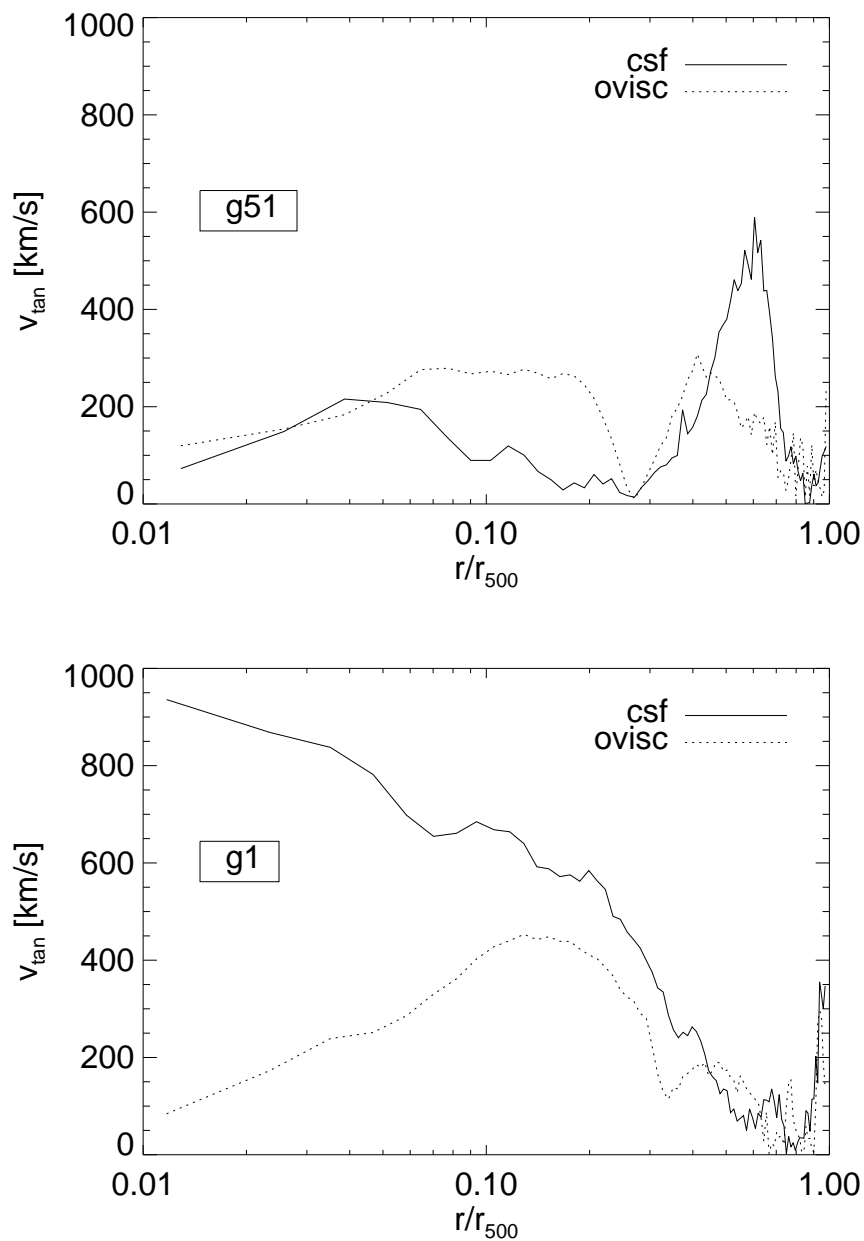
Figure 3.3: Rotational velocity as function of the radius out to R_{500} for a relaxed cluster (g51, upper panel) and for a highly disturbed system (g1, lower panel), at $z = 0$. The tangential component of the ICM velocity is calculated on the best equatorial plane, i.e. the plane perpendicular to the direction of the mean gas angular momentum in the region within $0.1R_{500}$. Two runs are compared: the *csf* simulation (solid line), including radiative cooling, star formation and supernova feedback, and the *ovisc* simulation (dashed line), in which all these physical processes are omitted and only a treatment for artificial viscosity is considered.

the mass–weighted average value of v_{tan} of the gas particles at each r. We have chosen $14h^{-1}$ kpc, as optimal bin width on the base of both resolution and statistical motivation.

The radial profiles for the rotational component of the gas velocity reflect the presence of a non–negligible rotational pattern in the ICM of the disturbed system, while no significant rotation is built up in the relaxed one. The profile of g51 (upper panel in the Figure, solid curve) shows relatively low values at small radii, and increases significantly only at radii larger than $\sim 0.3R_{500}$, where the rotational component of the velocity is likely to be dominated by some bulk rotational motions, plausibly related to a subhalo orbiting in the main halo close to R_{500}. The value of v_{tan} decreases instead with increasing r for g1 (lower panel in the Figure, solid curve), where the rotational velocity reaches almost 1000 km/s in the innermost region. Also, it is interesting to compare with the rotational velocity profile for two counterpart haloes, simulated without including star formation and cooling (dashed curves). In such simulation, referred to as *ovisc* simulation (see Dolag et al., 2009, as an overview) the overcooling problem is completely avoided because no stars are formed at all, and no significant rotation is expected to build up in the center of the cluster–like haloes. Let us note that for g51, the curves referring to the two simulations have a significantly similar trend, while for g1 the *csf* simulation (solid curve) and the non–radiative one diverge towards the center, increasing in the former and decreasing in the latter. While major events occurring close to $z = 0$ in the merging history of g1 could explain the high values found for v_{tan} in the innermost region, no major mergers happen to characterize the history of g51 at late time. Therefore a further zoom onto g51 is required in order to understand the details of the processes that lead to the build–up or to the disruption of gas rotation in the halo core.

Rotational velocity evolution

The possibility to track back the history of the cluster–size haloes given by simulated data, allows us to follow the redshift evolution of the rotational component of the ICM velocity in the innermost region of g51, taken to be $0.1R_{500}$. Up to $z = 2$, a mass–averaged value of the tangential component of the ICM velocity has been calculated in the best equatorial plane, so that rotation can be emphasized best whenever there is one. At each redshift, the orientation of the best equatorial plane has been adjusted to be perpendicular to the direction of the mean gas angular momentum, as previously defined.

While in the literature we find an inspiring work (e.g. Fang et al., 2009) where values for the rotational velocity in the central region of a relaxed cluster–like halo rise above $1000 \, \text{km/s}$, in our study this never happens and values generally increase up to $650 \, \text{km/s}$ as a maximum, except for high peaks probably related to major merging events. These differences are likely to be related to the different amount of baryon cooling that characterizes the simulations analyzed in the work by Fang et al. (2009) (extensively described in Kravtsov et al., 2005, 2006; Nagai et al., 2007) with respect to those discussed here. The stellar fraction $f_*(< r) = M_*(< r)/M(< r)$ in the central part of our Set 1 clusters (i.e. $< R_{500}$) is estimated to be smaller than in Fang et al. (2009) simulations, by about a factor of ~ 1.5. Though, it is definitely higher than expected from observations of real clusters (e.g. Lin et al., 2003). The implementation of cooling in GADGET–2 reduces the overcooling problem, naturally preventing strong rotation to get established.

In Fig. 3.4 we plot the variation of v_{tan} with redshift, calculated in the innermost region of g51. The peak shown around redshift ~ 1.5 is likely to be driven by the last major merger occurring to g51, and is not related to a quiescent build–up of mass and
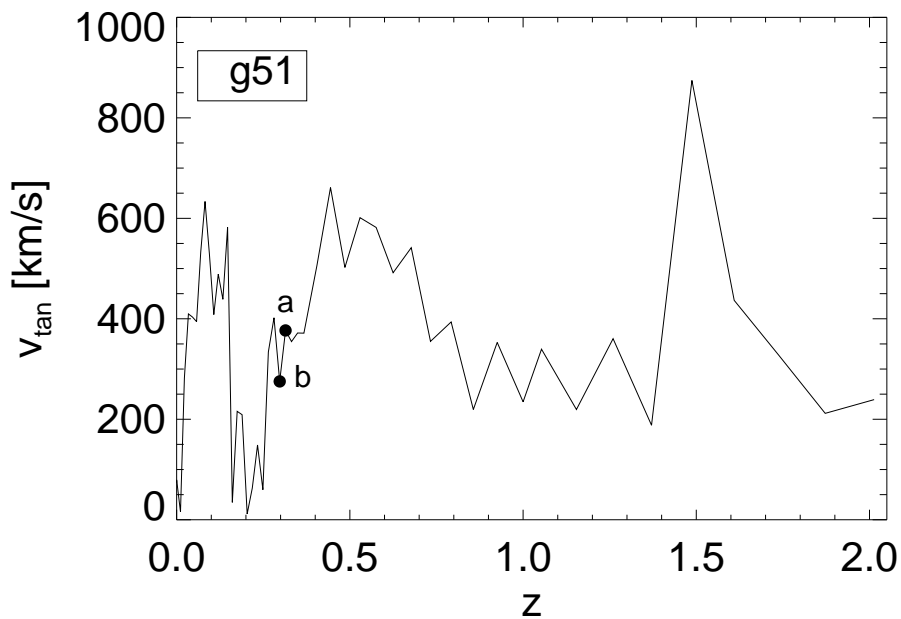
Figure 3.4: Evolution with redshift of the tangential component of the ICM velocity in the innermost region ($< 0.1R_{500}$) of g51.

therefore of rotation. Instead, within the redshift range $\sim 1.5 - 0.5$, a general, although not smooth, increasing trend of v_{tan} can be seen in the plot, which is likely to be explained as the result of the collapsing process under angular momentum conservation, although it is difficult to show it quantitatively. At lower redshift, it is worth to point out an interesting feature, that is the sudden drop of v_{tan}, steeply decreasing twice at $z \sim 0$ and ~ 0.3. The breaks in this expected general trend are not directly related to any major event, and a deeper investigation of the ICM internal dynamics has then been performed in order to understand the possible origin of this unexpected behavior.

ICM velocity maps

The panels in Fig. 3.5 show the two–dimensional velocity field in the best equatorial plane in the central slices of g51. Each velocity vector has a length proportional to the absolute value of the velocity in that point of the plane. The dashed circles mark the innermost region enclosed within $0.1R_{500}$ (smaller circle) and R_{500} (larger circle).

The velocity maps catch one of the two major decreases in the curve of v_{tan}, in particular the one at roughly $z \sim 0.3$, which is the first significant break in the increasing trend shown up to redshift ~ 0.5. Clearly, one can see the passage of a gas–rich subhalo (thicker circle) through the best equatorial plane, onto which the gas velocity field has been projected in the Figure. The subhalo is the only gas-rich subhalo approaching the central region of the simulated cluster.

The two panels in Fig. 3.5 refer to redshift $z \sim 0.314$ (upper panel) and $z \sim 0.297$ (lower panel), and show the best moment right before and after the first passage of the substructure through the equatorial plane. The steep decrease of v_{tan} does not start at this moment nor does it reach the lowest value, but these two redshift snapshots have been judged to best show a plausible explanation of the suppression of rotation while it is happening. In fact, from the velocity fields we notice that the gas shows a rotational motion with velocities of $\sim 380\,\mathrm{km/s}$ in the innermost region, close to the smaller dashed circle, while the subhalo is approaching (upper panel). This rotational pattern is evidently disturbed in the lower panel, where the subhalo has already passed through the plane, its gas particles get probably stripped by the main halo gas and contribute to decrease the velocity values to $\sim 275\,\mathrm{km/s}$.

Let us stress that there are several DM–only substructures permanently moving within

the cluster and close to the innermost region, but they do not disturb the build–up of rotation as gas–rich subhaloes do. The decrease of v_{tan} at redshift ~ 0 shows an analogous behavior.
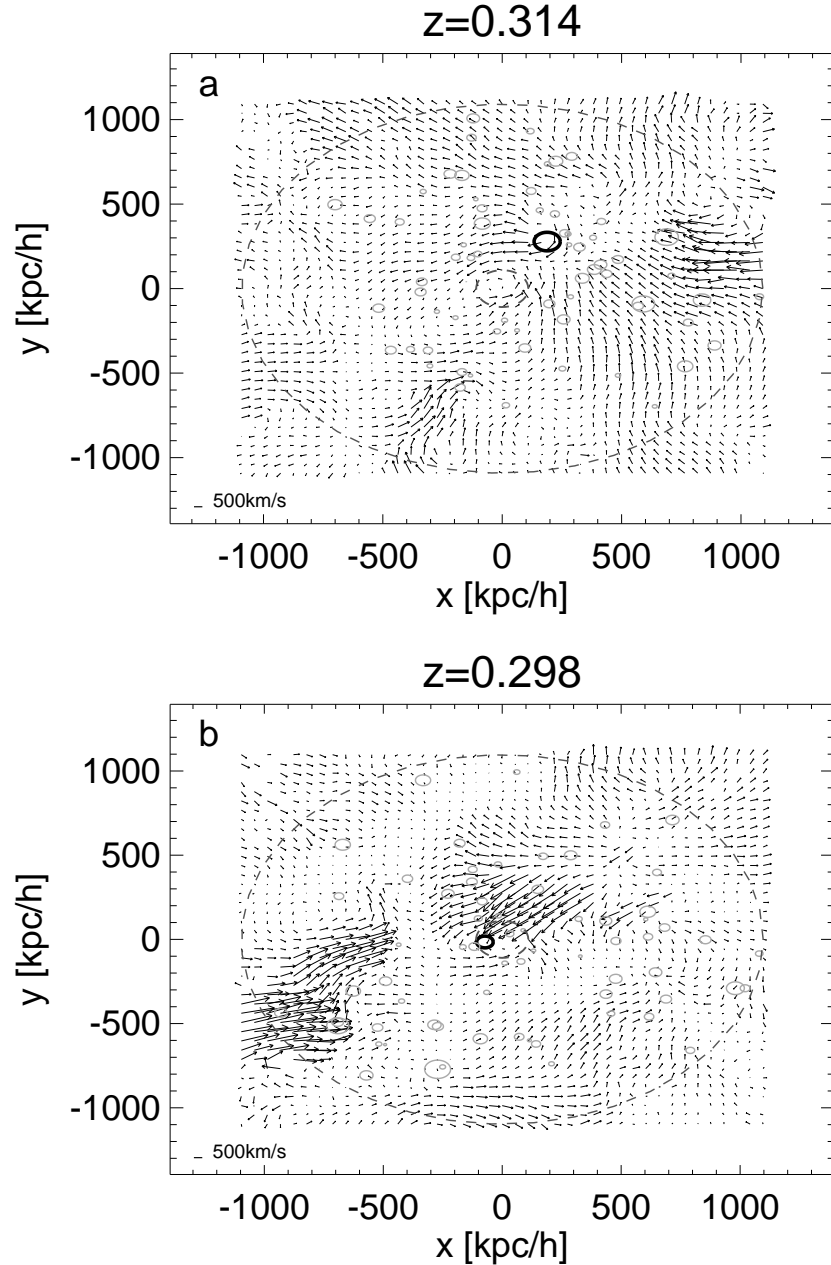
Figure 3.5: Gas velocity fields at $z \sim 0.314$ (upper panel) and $z \sim 0.298$ (lower panel) projected onto the plane perpendicular to the direction of the gas mean angular momentum in the innermost region. The smaller and larger dashed circles mark respectively the regions of $0.1R_{500}$ and R_{500}, while the grey ones are DM–only subhaloes and the black circle is the gas–rich halo passing through the equatorial plane. The coordinates in the graphs are in comoving units.

3.4   Rotational contribution to total mass

In this section we compare the contribution coming from rotational motions that should be considered in the estimation of total mass with the total mass calculated for the simulated clusters. Formally, the total cluster mass M enclosed within a closed surface $\mathbf{S}$ is given by Gauss's Law

$$M = \frac{1}{4\pi G} \int \nabla\Phi \cdot d^2\mathbf{S}, \tag{3.1}$$

where Φ is the cluster gravitational potential and G is the gravitational constant. Under the assumptions that the ICM is a steady–state, inviscid, collisional fluid, we can replace the term $\nabla\Phi$ with the terms involving gas pressure and velocity using Euler's equation as follows:

$$M = \frac{1}{4\pi G} \int \left[-\frac{1}{\rho_g}\nabla P_g - (\mathbf{v}\cdot\nabla)\mathbf{v} \right] \cdot d^2\mathbf{S}, \tag{3.2}$$

where ρ_g and P_g are the gas density and pressure respectively. While the pressure term within the integral represents the contribution of the gas random motions, both thermal and turbulent, the velocity term includes the ordered motions in the ICM, i.e. rotational and streaming motions. For the purpose of our work, we are mainly interested in the contribution to the pressure support given by the rotational motions of the hot intracluster gas, and we therefore separate the velocity term in Eq. 3.2 into

$$M_{rot} = \frac{1}{4\pi G} \int \left(\frac{v_\theta^2 + v_\phi^2}{r} \right) d^2 S \tag{3.3}$$

and

$$M_{str} = -\frac{1}{4\pi G} \int \left(v_r \frac{\partial v_r}{\partial r} + \frac{v_\theta}{r}\frac{\partial v_r}{\partial\theta} + \frac{v_\phi}{r\sin\theta}\frac{\partial v_r}{\partial\phi} \right) d^2 S, \tag{3.4}$$

by evaluating $(\mathbf{v}\cdot\nabla)\mathbf{v}$ in spherical coordinates (Binney and Tremaine, 2008; Fang et al., 2009). In particular, the term due to streaming motion, M_{str}, is likely to be less relevant than M_{rot}, especially for relaxed clusters. Therefore we explicitly calculate the rotation term for our clusters g51 and g1 at several redshifts. In our analysis we compare this term with the total "true" mass of gas and dark matter for the cluster, M_{true}, computed directly by summing up all the particle masses.

In Fig. 3.6 we show the radial profiles of both M_{rot} and M_{true}, and their ratio, for g51 (upper panel) and g1 (lower panel) at $z = 0$. In order to evaluate Eq. 3.3 we consider the full three–dimensional structure of the velocity field without any assumption of spherical symmetry, as stated in Gauss's theorem, so that our calculation is completely independent
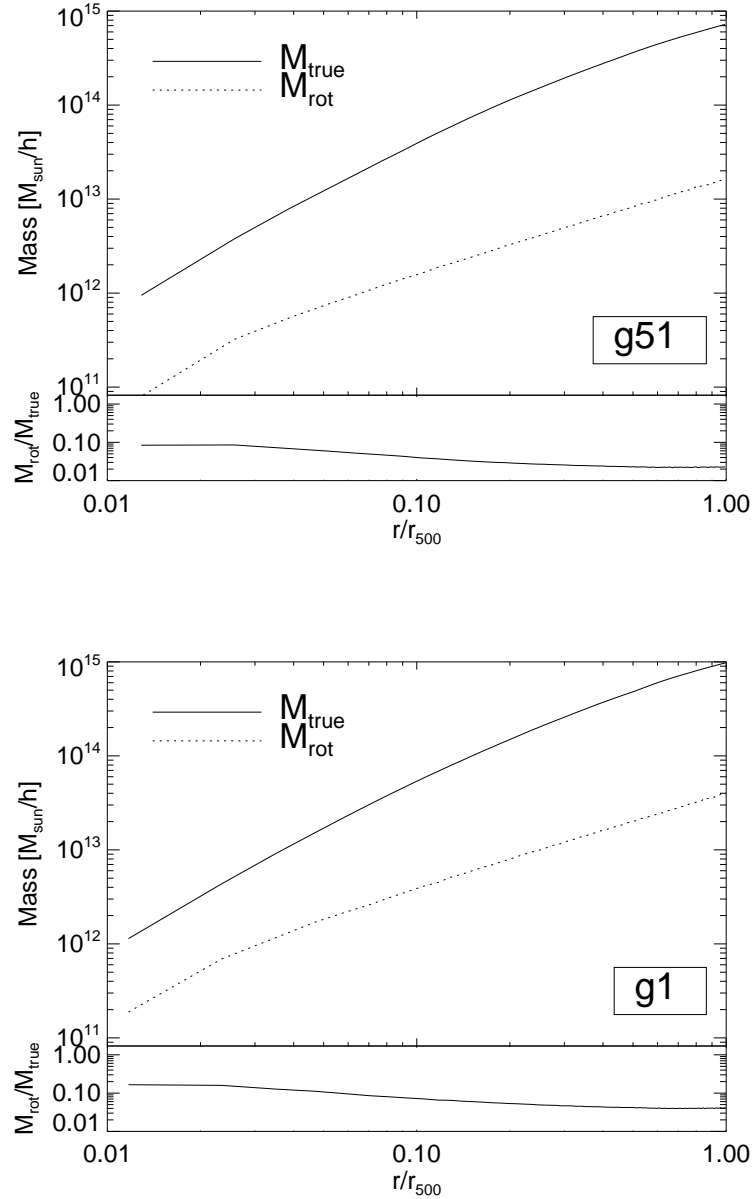
Figure 3.6: Mass profiles of the relaxed cluster g51 (upper panel, upper frame) and of the disturbed system g1 (lower panel, upper frame), at $z = 0$. Top frame: in each panel, the radial profiles of the true mass, M_{true} (solid line), and of the component estimated from the gas rotation, M_{rot} (dotted line), out to R_{500} are shown. Bottom frame: ratio of the two mass terms M_{rot}/M_{true} as function of radius for g51 (left–hand panel) and g1(right–hand panel).

of the cluster geometry. In our approximation of the integral that appears in Eq. 3.3, the closed surface **S** has been replaced with a spherical shell at each radial bin, and we sum over the single particle contributions in the shell instead of dividing the surface in cells.

Specifically, at each radial bin we associate an effective area to each gas particle in the shell and compute the integrand term considering the velocity $(v_\theta^2 + v_\phi^2)$ of the particle. We make use of a radial binning up to R_{500}, each bin of $14h^{-1}\,$kpc, consistent with the profiles of $v_{tan}(r)$ discussed in Section 3.3.2.

The profiles shown in Fig. 3.6 have similar trends for both g51 and g1, but one can clearly notice that the more significant rotational pattern found in the innermost region of the disturbed cluster g1 with respect to g51 is reflected here in a more significant contribution to the total mass of M_{rot}. In general, the rotation appears to be more important in the innermost regions than in the cluster outskirts. Indeed, out to R_{500} the rotational component of the total mass accounts for $\sim 2\%$ of the true mass, M_{true}, in g51 and slightly more in the case of g1 (4%). In contrast, M_{rot} plays a more significant role at radii $< 0.1R_{500}$, where its contribution can be up to $9 - 17\%$ of M_{true}, the highest value reached in the core region of g1. Although we consider purely rotational motions, other non–thermal motions should be accounted for as well and we can conclude that, if rotation establishes, it can significantly contribute to the total pressure support to the cluster weight.

3.5 Extending the statistics to a larger simulated sample

In order to gain a more reliable overview of the phenomenon of the appearance of rotational patterns in the innermost regions of cluster–like haloes, our analysis has also been performed for Set 2, a larger sample of simulated objects spanning a range of M_{200m} from $\sim 5 \times 10^{14}h^{-1}\,\mathrm{M}_\odot$ to $\sim 2.2 \times 10^{15}h^{-1}\,\mathrm{M}_\odot$.

The selection of the sample has been carried out such that we isolate all the haloes in the cosmological box with virial mass above a mass threshold, chosen to keep a statistically reliable number of objects throughout the redshift range explored. At $z = 0$, we selected 26 haloes with $M_{200m} > 5 \times 10^{14}h^{-1}\,\mathrm{M}_\odot$, for which a visual representation is given in Fig. 3.7. At higher redshift, the mass threshold is lower in order to have a fair sample to investigate statistically. We calculate the distribution of the rotational velocity on the best equatorial plane in the innermost region (i.e. $< 0.1R_{500}$) of each selected halo, sampling the redshift range $[0, 0.5]$.
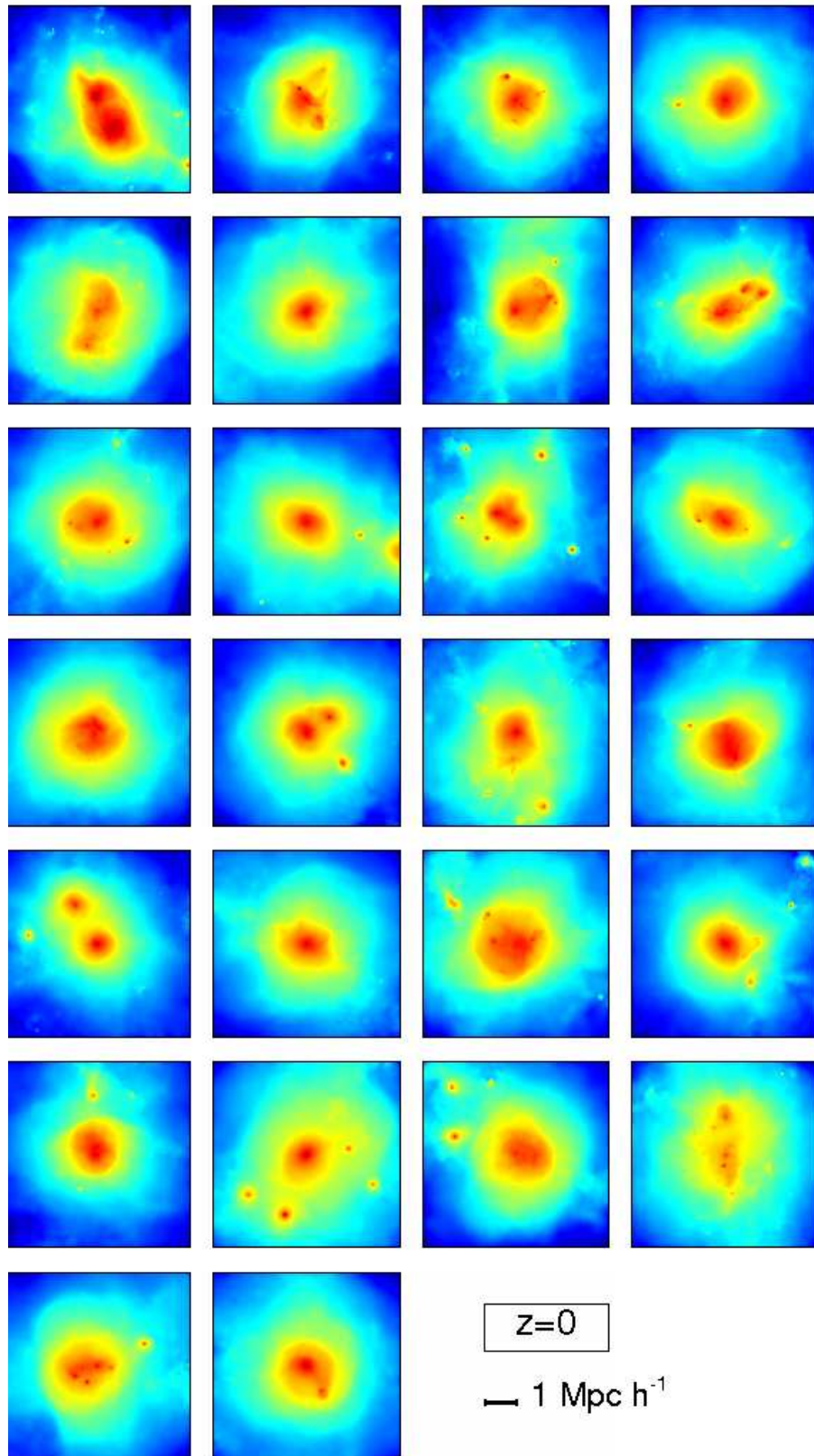
Figure 3.7: Visualization of the gas SB, in arbitrary units, for the 26 cluster–size haloes selected at $z = 0$ from the Set 2.

3.5.1   Distribution of rotational velocities at various redshifts

In Fig. 3.8 we show the distribution of v_{tan}, calculated $< 0.1R_{500}$ in the same way as for g51, for the sample of cluster–like haloes belonging to the Set 2. The histograms show how significant rotation is over the range of masses and redshifts, confirming the intermittent nature of the phenomenon. Starting form the upper–left panel to the bottom–right one, redshift increases from 0 to ~ 0.5 and the sample consists of a number of objects varying between 26 and 44. The mass threshold chosen, M_{th}, is $5 \times 10^{14}, 4 \times 10^{14}, 3 \times 10^{14}, 2 \times 10^{14} h^{-1} \, \mathrm{M_\odot}$ for the four redshift values considered ($z = 0, 0.1, 0.3, 0.5$, respectively). We notice that in general the velocity distributions
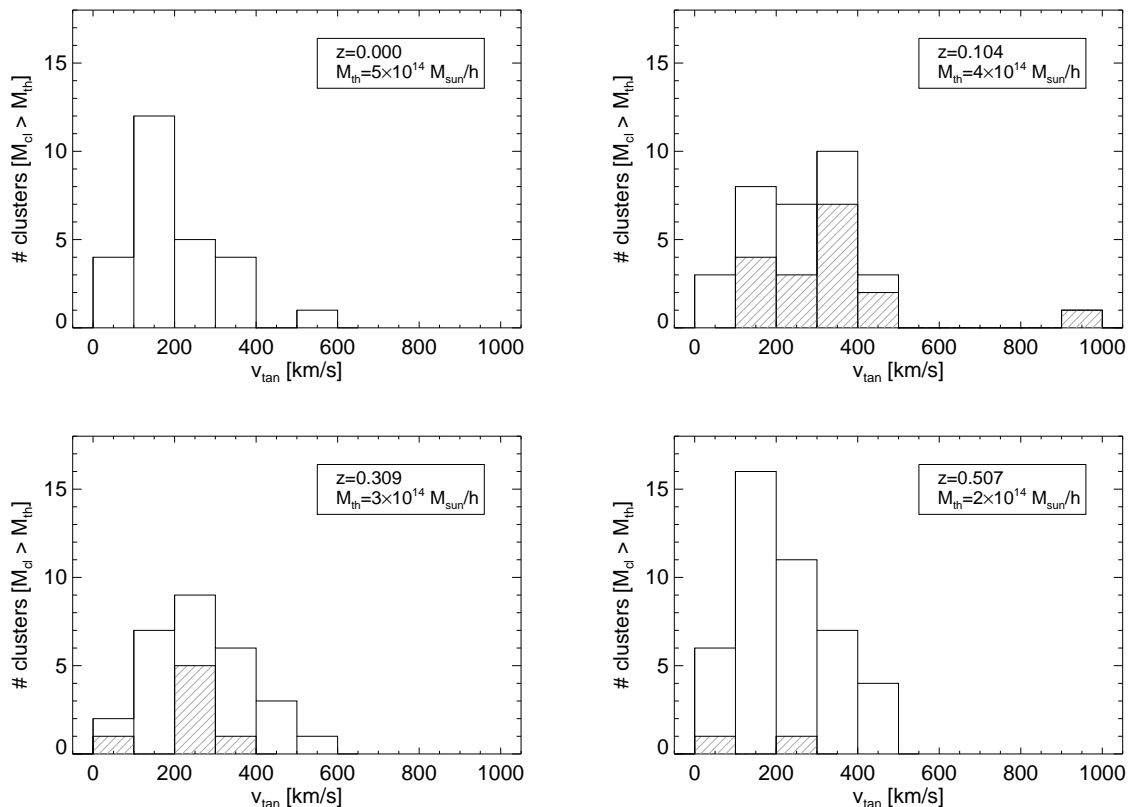
Figure 3.8: Distribution of the rotational velocity for a sample of simulated clusters extracted from the Set 2. The tangential component of the gas velocity, v_{tan}, is the mean value within $0.1R_{500}$, calculated in the plane perpendicular to the mean gas angular momentum in the same region. Top left–hand to bottom right–hand panel: the panels refer to a sample of objects from the Set 2 at different redshifts, sampling the range $[0, 0.5]$. The sample of objects has been selected according to a threshold in mass, M_{th}, which is lower at higher redshift in order to keep a fair statistics. While M_{th} is different at each redshift, the shaded regions represent subsamples of haloes selected to be more massive than $5 \times 10^{14} h^{-1} \, \mathrm{M_\odot}$, as a comparison to the distribution at $z = 0$.

are mainly centered around values of $200 - 300\,\mathrm{km/s}$, with a mild, though not substantial, shift towards higher values for intermediate redshift. The shaded histograms on top of the ones plotted for redshifts $z = 0.1, 0.3, 0.5$ refer to subsamples of haloes with $M_{200m} > 5 \times 10^{14} h^{-1}\,\mathrm{M}_\odot$ (the same as the one used at $z = 0$). This comparison is meant to show a clear evidence that also the higher–mass subsample actually agrees with the general trend. Although the number of objects in these subsamples decreases for increasing redshift, this has been done in order to confirm the idea that indeed the distribution of the rotational velocities is peaked around quite low values. Except for some outliers, we can generally exclude any clear monotonic increase of the typical value of v_{tan} in the cluster innermost region (always kept to be $< 0.1 R_{500}$) associated to the assembling of the cluster–size haloes. In our simulations we cannot find any quiescent build–up of rotation as a consequence of mass assembly, and the distribution among the volume–selected sample is not dramatically changing with redshift.

3.6   Discussion and conclusion

In this work, we have presented the result of a study over two sets of hydrodynamical simulations performed with the TreePM/SPH code GADGET–2. The simulations include radiative cooling, star formation, and supernova feedback and assume slightly different cosmological models, a ΛCDM one and a WMAP3 one. The main target of this analysis has been the importance of rotational gas motions in the central regions of simulated cluster–like haloes, as it is thought to be a crucial issue while weighing galaxy clusters and identifying them as relaxed systems. The objects selected from our samples guarantee a wide variety of virial masses and dynamical structures, so that a reliable investigation of this phenomenon is allowed.

Our main results can be summarized as follows:

- As main conclusion, we notice that the occurrence of rotational patterns in the simulated ICM is strictly related to the internal dynamics of *gas–rich* substructures in a complicated way, so that it is definitely important to take it into account as contribution to the pressure support, but it's not directly nor simply connected to the global dynamical state of the halo.

- In the first part of our analysis we focused on g51, a simulated cluster with a very

smooth late accretion history, isolated and characterized by few substructures in comparison to the other massive objects within Set 1. Also, we compare it with a highly disturbed system (g1). Even in the radiative simulation of this cluster, likely to be considered relaxed in a global sense, *no clear rotation* shows up *at low redshift because of some minor merging events* occurring *close to the innermost region*: the rotation of the core is found to be an intermittent phenomenon that can be easily destroyed by the passage of gas–rich subhaloes through the equatorial plane. Gas particles stripped from the subhalo passing close to the main–halo innermost region ($< 0.1R_{500}$), are likely to get mixed to the gas already settled and contribute over few orbits to change the inclination of the best equatorial plane, suppressing any pre–existing rotational pattern.

- The velocity maps plotted in Fig. 3.5 show several DM–only subhaloes moving close to g51 central core. In our study, they have been found not to disturb in any significant way the ordered rotational gas motions created in the innermost region. The central gas sloshing is mainly set off by gas–rich subhaloes, especially if they retain their gas during the early passages through the core. Interesting work on numerical simulations have been found to be relevant for the result presented here, as the study from Ascasibar and Markevitch (2006) on the origin of cold fronts and core sloshing in galaxy clusters.

- Mass measurements based on HEH are likely to misestimate the total mass of galaxy clusters because of contributions by non–thermal gas motions that have to be considered. In agreement with previous works, we also find that significant rotation of the ICM can contribute to the pressure support. While several studies have been carried out on turbulent motions in the ICM and on their effect on the cluster mass estimates (e.g. Rasia et al., 2004; Fang et al., 2009; Lau et al., 2009; Zhuravleva et al., 2010), only lately the work by Fang et al. (2009) and Lau et al. (2009) have been addressing the ordered rotational patterns that could establish in the innermost region ICM as the result of the cluster collapse. Therefore, a comprehensive analysis of the details of rotation build–up and suppression both in single high–resolution case–studies and in larger, statistically significant samples is extremely interesting, especially for relaxed objects where this should be more important than turbulence.

Focusing on rotation specifically, we calculated the corresponding mass term, M_{rot}, for the two clusters g51 and g1. As expected from the tangential velocity profiles at redshift $z = 0$, the mass term coming from ICM rotational motions contributes more in the case of g1 than in g51, providing evidence that rotational support of gas in the innermost region is more significant in the former than in the latter. While M_{rot} accounts for few percents at radii close to R_{500} in both cases, in the central regions up to $\sim 17\%$ of the total true mass in g1 is due to rotational motions of the ICM. As regards g51, this contribution is less important, as no strong rotation has been found at $z = 0$, but it still reaches a value of $\sim 10\%$ for the pressure support in the cluster core.

- Extending the analysis to a larger sample, we have investigated the statistical distribution of rotational velocity over dynamically–different clusters, isolated in a limited–volume simulated box such that their virial mass (M_{200m}) is above a chosen threshold. At $z = 0$ as well as at higher redshift up to ~ 0.5, a fair sample of cluster–size haloes let us infer that, on average, no high–velocity rotational patterns show up in the halo cores (i.e. in the region $< 0.1R_{500}$). Also for the clusters of Set 2, we find typical values of $\sim 200 - 300\,\mathrm{km/s}$ for the rotational velocity in the innermost region.

- We do not find any increasing trend of the rotational velocity distribution peak with decreasing redshift, that can correspond to the smooth mass assembly of the cluster–like halo through collapse. Although such trend is generally expected, it must be easily suppressed by internal minor events disturbing the halo central region.

We conclude that the build–up of rotational patterns in the innermost region of galaxy clusters is mainly related to the physical processes included in the *csf* run to describe the intracluster gas. On the contrary, numerical effects such as different implementations of artificial viscosity (Dolag et al., 2005) do not affect in any significant way our results (see Appendix 3.7.1, for a detailed discussion).

An analogous conclusion can be drawn with respect to the differences between the two samples introduced by cosmology and resolution. For both Set 1 and Set 2 the build–up and suppression of rotational patterns in the halo central part is found to be mainly related to the physics included in the radiative run. In fact, comparable subsamples of

the two sets in the *csf* simulations show very similar distributions of rotational velocities for the ICM component in the halo innermost region, meaning that the shape of the distribution is essentially dominated by the physics of the gas. Usually, relaxed clusters are assumed to have little gas motions. Therefore they are likely to be the best candidates for the validity of the HEH, on which mass estimations are based. Nevertheless, rotational motions should establish preferentially in relaxed clusters with respect to disturbed systems as a consequence of the assembling process, potentially representing a danger for relaxed cluster masses. Here, however, we find that the processes described in the paper save the reliability of the HEH–based mass determinations in most of the cases. In fact, rotational motions are not significant enough to compromise dramatically mass determinations with the exception of few outliers. In our simulation, the identification of relaxed or non–relaxed clusters according to the presence of gas rotation in the central region is not straightforward, since it has been shown to appear and disappear periodically. Its contribution has to be considered whenever is present, but it is not directly related to the global state of the simulated halo. Also, it is likely to be strongly influenced by the overcooling problem affecting hydrodynamical simulations, which has the effect to enhance the process of building up rotational patterns in the ICM in the innermost regions of simulated clusters.

Although various theoretical and numerical studies in addition to the present work have been investigating the existence of gas bulk, non–thermal motions and the possible ways to detect them in galaxy clusters (e.g. Fang et al., 2009; Lau et al., 2009; Zhuravleva et al., 2010), little is known from observations. In a recent study, Laganá et al. (2010) have made use of assumptions from theoretical models and numerical simulations about cosmic rays, turbulence and magnetic pressure to consider these non–thermal contributions to the total mass measurement for five Abell clusters. From a pure observational point of view, previous work has been able to confirm only indirect indications of bulk gas motions associated to merging events in galaxy clusters (see Markevitch and Vikhlinin, 2007, for a review) or evidences for turbulent gas motions, like the ones found in the Coma cluster in Schuecker et al. (2004) or those inferred, on the scale of smaller–mass systems, from the effects of resonant scattering in the X-ray emitting gaseous haloes of large elliptical galaxies (Werner et al., 2009). Although not possible so far, the most direct way to measure gas motions in galaxy clusters would be via the broadening of the line profile of

heavy ions (like the iron line at $\sim 6.7\,\mathrm{keV}$ in X–rays) for which the expected linewidth due to impact of gas motion is much larger than the width due to pure thermal broadening. The possibility to use the shape of the emission lines as a source of information on the ICM velocity field as been discussed in detail in Inogamov and Sunyaev (2003) and Sunyaev et al. (2003), and lately in Rebusco et al. (2008). Though, the investigation of the imprint of ICM motions on the iron line profile requires high–resolution spectroscopy, which will become possible in the near future with the next–generation X–ray instruments such as ASTRO–H and IXO. This will allow us to directly detect non–thermal contributions to the cluster pressure support, such as rotational patterns in the ICM, and enable us to take this correctly into account as contribution to the total mass estimate. Ultimately, this is likely to be an important issue to handle in order to better understand deviations from the HEH, on which scaling laws are usually based.

3.7 Appendix

3.7.1 Effects of artificial viscosity

The runs studied in the present work are the *csf* simulation, including radiative cooling, star formation and supernova feedback, and the non–radiative simulation (labelled as *ovisc*), where the original parametrization of artificial viscosity by Monaghan and Gingold (1983) is used. We comment here on the effects of the artificial viscosity on our study by considering two additional non-radiative runs of our simulations, carried out with alternative implementations of the artificial viscosity scheme. In particular, we label as *svisc* the non-radiative run with slightly less numerical viscosity based on the signal velocity approach of Monaghan (1997), and as *lvisc* the modified artificial viscosity scheme where each particle evolves with its own time–dependent viscosity parameter (as originally suggested in Morris and Monaghan (1997)). For a detailed description of these non–radiative runs we refer the reader to Dolag et al. (2005).

In Fig. 3.9 the distribution of the value of v_{tan} for the Set 1 is presented for the different runs. With the solid black line we refer to the *csf* simulation, while the other histograms represent the non-radiative runs: *ovisc* (dotted red line), *svisc* (green dashed) and *lvisc* (blue, dot–dashed). As one can see from the Figure, the *csf* simulation shows a different distribution of rotational velocity in the innermost regions of the cluster–like haloes with
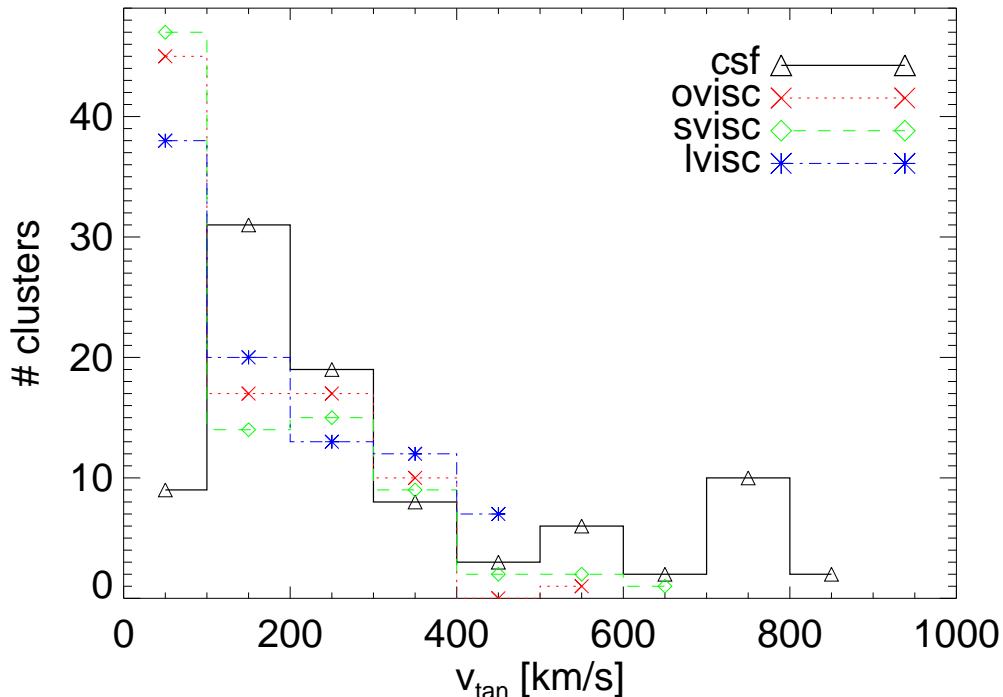
Figure 3.9: Distribution of rotational velocity (calculated in the region $< 0.1R_{500}$) for Set 1 in the redshift range $[0 - 0.5]$. The different runs are plotted: *csf* (solid, black line with triangles), *ovisc* (dotted, red with crosses), *svisc* (green, dashed with diamonds), *lvisc* (blue, dot–dashed with asterisks).

respect to the non–radiative runs, in which the difference in the implementation for the artificial viscosity does not produce significant differences in the three distributions. In Fig. 3.9 is evident that the difference between the radiative and non–radiative runs is much larger than the difference among the non–radiative runs themselves. All the non–radiative runs similarly show that the largest fraction of clusters have very low values of v_{tan}, and differ mostly in the lack of a high-velocity end of the distribution from the *csf* case. The cooling of the core allowed by the physics included in the *csf* run is plausibly responsible for the presence of a significant fraction of clusters with high velocity values, which do not exist in the non–radiative runs.

From Fig. 3.9 we can confirm that, accordingly to what is expected, the overcooling problem coming along with numerical simulations of galaxy clusters leads to a more significant build–up of rotation in the core, reflected in an overall shift towards higher values of the distribution of v_{tan}.

For the purpose of our study, we can conclude that the main effects in the establishment

of rotational patterns in the central region of simulated clusters are introduced by the physical processes describing the gaseous component, included in the *csf* simulation. The amount of turbulence, referring in particular to small scale chaotic motions, was found to strongly differ among the non–radiative runs investigated here (e.g. Dolag et al., 2005). However, the effect of artificial viscosity on rotation does not depend strongly on the specific numerical scheme implemented, and we safely confirm our conclusions about the more significant effect that minor events occurring close to the cluster central region have on the survival of gas rotational motions.

3.7.2 Ellipticity of ICM

As interestingly suggested in a recent work by Lau et al. (2011), certain observable features of the cluster X–ray emission, like a flattening of cluster shapes, could unveil the presence of rotationally supported gas, especially in the innermost region. Referring to the X–ray surface brightness maps in Fig. 3.1, we compare here the ellipticity profiles extracted from the maps in the three projections to the rotational velocity profile, for the two cases of study extracted from Set 1 (namely, g51 and g1) at redshift $z = 0$. The ellipticity was calculated by means of the IRAF task `ellipse` and the reported error bars are those obtained by the fitting method. In Fig. 3.10 the v_{tan} profile is marked by the solid curve for each cluster, while the dotted, dashed and dot–dashed lines refer to the ellipticities from the three projected maps. Let us note that the ellipticity profiles do not extend to the very central part, since the complex structure in the innermost region does not allow for a simple determination of ellipticities. We can conclude that only a mild relation between ellipticity and rotation is found in these clusters and the difference in the trends shown by the rotational velocity profiles is stronger than the difference among the ellipticity profiles of the two clusters. Nevertheless, comparing the *csf* run (upper panels) to the *ovisc* run (lower panels) we can confirm that the cluster shape is actually marked by the physics included in the radiative run, especially in the g1 case, where some rotation establishes in the *csf* simulation. In conclusion, gas cooling can affect the gas shape by flattening the X–ray isophotes but we do not find a strong significant evidence for that in our case–study clusters, in agreement with the milder rotation found and the nature of such rotational patterns (like in the g1 example), which are likely to be temporary effects driven by major merging events.
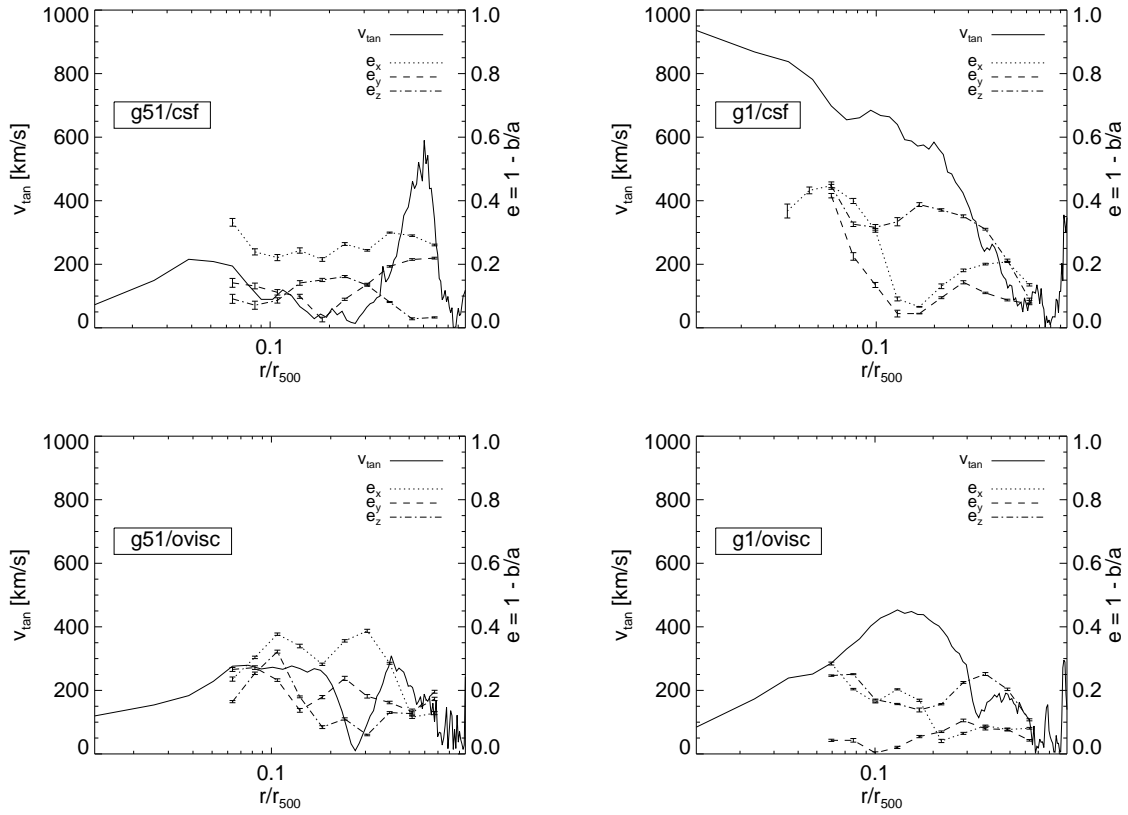
Figure 3.10: Radial profiles of ellipticity (left–hand side y–axis; dotted, dashed and dott–dashed curves) for the three projection axis compared with the radial profile of the gas rotational velocity (right–hand side y–axis; solid curve). The panels refer to the *csf* and the *ovisc* simulations (upper and lower panels, respectively) of g51 (left–hand panels) and g1 (right–hand panels) at $z = 0$.

Chapter 4

Observing simulated galaxy clusters with PHOX: a novel X–ray photon simulator

Veronica Biffi, Klaus Dolag, Hans Böhringer & Gerard Lemson

We present a novel, virtual X–ray observatory designed to obtain synthetic observations from hydro–numerical simulations, named PHOX. In particular, we provide a description of the code constituting the photon simulator and of the new approach implemented. We apply PHOX to simulated galaxy clusters in order to demonstrate its capabilities. In fact, X–ray observations of clusters of galaxies continue to provide us with an increasingly detailed picture of their structure and of the underlying physical phenomena governing the gaseous component, which dominates their baryonic content. Therefore, it is fundamental to find the most direct and faithful way to compare such observational data with hydrodynamical simulations of cluster–like objects, which can currently include various complex physical processes. Here, we present and analyse synthetic *Suzaku* observations of two cluster–size haloes obtained by processing with PHOX the hydrodynamical simulation of the large–scale, filament–like region in which they reside. Taking advantage of the simulated data, we test the results inferred from the X–ray analysis of the mock observations against the underlying, known solution. Remarkably, we are able to recover the theoretical temperature distribution of the two haloes by means of the multi–temperature fitting of the synthetic spectra. Moreover, the shapes of the reconstructed distributions allow us to trace the different thermal structure that distinguishes the dynamical state of the two haloes.

4.1   Introduction

As optimal laboratories for both cosmology and astrophysics, galaxy clusters have been thoroughly investigated with large surveys as well as via dedicated single–object observations. In this respect, X–ray measurements still represent one of the best ways to fully study their structure, traced by the hot plasma filling their potential wells. In particular, the most important and difficult quantity to infer is the total gravitating mass, which can be determined from measurements of the intra–cluster medium (ICM) temperature and density profiles, assuming hydrostatic equilibrium to hold. So far, studies of the X–ray–emitting ICM have been mainly limited to the innermost region, where the investigation of the baryonic physics is observationally less challenging than in the outskirts. Although very difficult to map in the X rays, a characterization of the outer region of clusters is in fact crucial to understand the formation and evolution of this structures and to use them as cosmological probes, since it encloses a significant fraction of the cluster volume, where the properties of the accreting gas and of the dark matter halo are still uncertain (e.g., see Ettori and Molendi, 2011). Only very recently, X–ray observations performed with the Japanese satellite *Suzaku* have reached the virial radius for a few clusters of galaxies (e.g. Fujita et al., 2008; Bautz et al., 2009; George et al., 2009; Reiprich et al., 2009; Hoshino et al., 2010; Kawaharada et al., 2010; Simionescu et al., 2011; Akamatsu et al., 2011), promisingly taking a step forward on the temperature profile debate and indirectly opening new perspectives in controlling the biases on cluster–based cosmological investigations. These results are just one example of the improvements by which X–ray observations continue to provide us with an increasingly detailed picture of galaxy clusters, for which a clear interpretation of the underlying physical processes is very challenging.

On the theoretical side, many interesting issues on cluster formation and evolution are addressed by means of hydro–numerical simulations, which represent a powerful tool to investigate in detail the nature of these complicated astrophysical objects (e.g. Borgani and Kravtsov, 2009, for a recent review). Simulations of large cosmological boxes that include several massive cluster–like haloes can now be performed incorporating not only the dominating dark matter component but also baryonic matter, in the form of gas– and star–like particles (or cells), governed by hydrodynamical processes. With particular

concern for galaxy clusters, current simulations are not only able to account for basic gas hydrodynamics, but implement also more complicated models for star formation from multi–phase medium (e.g. Katz, 1992; Katz et al., 1996; Springel and Hernquist, 2003; Marri and White, 2003) and thermal or kinetic feedback from supernovae–driven winds (Navarro and White, 1993; Scannapieco et al., 2006; Dalla Vecchia and Schaye, 2008), chemical enrichment, metal and molecule cooling (e.g. Mosconi et al., 2001; Yoshida et al., 2003; Tornatore et al., 2004, 2007; Scannapieco et al., 2005; Maio et al., 2007, 2010), thermal conduction (Cleary and Monaghan, 1999; Jubelgas et al., 2004; Ruszkowski et al., 2010), AGN feedback (e.g. Springel et al., 2005a; Di Matteo et al., 2005; Sijacki and Springel, 2006; Sijacki et al., 2007, 2008; Puchwein et al., 2008; Fabjan et al., 2010; Dubois et al., 2010; Teyssier et al., 2011), cosmic rays (Pfrommer et al., 2007; Jubelgas et al., 2008) and magnetic fields (Phillips and Monaghan, 1985; Dolag et al., 1999; Brüggen et al., 2005; Price and Monaghan, 2005; Dolag and Stasyszyn, 2009), to name the most important effects.

The ideal achievement would be the combination of both these sources of information, by directly comparing simulated clusters to X–ray observations of real objects. Devoted to this goal, sophisticated numerical codes, such as X–MAS/X–MAS2 (Gardini et al., 2004; Rasia et al., 2008) and, more recently, XIM (Heinz and Brüggen, 2009; Heinz et al., 2010), have been developed in the last years in order to turn hydro–simulation outputs into mock images with a given X–ray telescope. In particular, the X–MAS virtual telescope is explicitly designed to process outputs obtained from SPH codes like GADGET, whereas XIM is particularly dedicated to grid–based hydrodynamical simulations, e.g. performed with the AMR code FLASH (Fryxell et al., 2000), which makes them fundamentally complementary. Similarly, both X–MAS and XIM use a plasma thermal emission code by which they calculate the projected emission associated to the gas component in the simulation. The computational effort, required to calculate this, is usually reduced by interpolating among the model spectra externally stored in a library of templates. Essentially, the emissivity integrated along the chosen line of sight is calculated in terms of flux, depending on the properties of all the gas at a given projected position. Lastly, the convolution with instrumental response is performed and the final photon event file is generated. Such virtual telescopes represent an important step forward with respect to visualization tools used to produce surface brightness maps from simulation outputs, since

they properly calculate the emission associated to the gas component accounting for the structure of the simulated source along the line of sight. Moreover, they are able to include accurate calculations required to obtain realistic mock X–ray observations, for instance convolving the simulated spectra with any given instrument response and telescope PSF. In fact, it is vital that the synthetic observations produced by such simulators are as much as possible similar to the standards commonly used by observers, so that the comparison can be the most faithful. As such, this advanced approach easily leads to a challenging increase of the parameters to handle in order to realistically model the plasma emission and the detailed three–dimensional structure of the simulations.

Analogous in the scope, the virtual telescope presented in this paper, PHOX, is also dedicated to convert hydro–numerical outputs into mock X–ray observations. However, the novelty of our simulator lies in the method adopted, by which the spectral emission calculated singularly for each gas element in the simulation is immediately converted into a discrete sample of photons, collected and stored before projecting along any line of sight and convolving with any desired instrument. With this strategy we are able to significantly gain in computational effort, since it requires to process the original simulation only once, independently of the specific synthetic observation to be performed afterwards. Furthermore, the guarantee for high spatial and spectral resolution, preserved without dramatically increasing the computational cost, offers the possibility to anticipate the observational achievements of upcoming X–ray missions, such as *IXO/ATHENA*, in which the high–resolution spectroscopy will allow us to explore the intrinsic structure of galaxy clusters through the study of their spectral features. In fact, it has been suggested in the last decade that the diagnostics of the broadening of heavy–ion emission lines in highly–resolved X–ray spectra of galaxy clusters could actually provide valuable information about the underlying structure of the ICM and its velocity field (see Pawl et al. (2005), for a preliminary, interesting work in this field), useful for the dynamical classification of these objects. The expectations for such line diagnostics are related in particular to the most prominent emission line in X–ray spectra, namely the $\sim 6.7\,\mathrm{keV}$ line from helium–like iron. In fact, the large atomic mass of the FeXXV ion significantly reduces the thermal line broadening, so that the line width turns out to be definitely more sensitive to turbulent or bulk gas motions (Inogamov and Sunyaev, 2003; Sunyaev et al., 2003). This kind of studies can eventually help constraining the detectability of

non–thermal motions that are likely to establish in the ICM (e.g. Rebusco et al., 2008) and can compromise X–ray mass measurements (Rasia et al., 2006; Fang et al., 2009; Lau et al., 2009; Biffi et al., 2011).

The paper is structured as follows: Section 4.2 is devoted to the description of the method implemented in the photon simulator and the fundamental units of the code. In Section 4.3 we apply PHOX to the hydrodynamical simulation of a filament–like structure, describing in detail each phase, from the photon generation till the mock *Suzaku* observation of two massive galaxy clusters residing in the filament and the spectral analysis of the synthetic spectra. Results about the recovering of the ICM emission measure distribution of the two cluster–like haloes from the multi–temperature fitting are presented in Section 4.4. Finally, we discuss the results obtained, summarise and draw our conclusions in Section 5.5.

4.2 PHOX: the technique

The novelty of our photon simulator arises from the method implemented. In this Section we describe the three main parts of the code that constitute the virtual telescope, PHOX[1], for which a schematic overview is also presented in Fig. 4.1. PHOX consists of a C code, which makes use of the publicly available X–ray package `XSPEC` (see Arnaud, 1996) to calculate model emission spectra, and of the GSL[2] and CFITSIO[3] external, auxiliary libraries.

With respect to the structure of the code, the first unit is the most general, essential one, in which the emission associated to the gaseous component in the simulation is generated without including any additional specification, neither about the observation to be simulated nor about the characteristics of the X–ray instrument, but the theoretical emission model. Ideally, the spectral model assumed can be very complicated and account for more realistic descriptions of the emitting gas which are included in up–to–date sophisticated hydro–simulations, such as metallicity, chemical composition and sub–grid turbulent broadening of the emission lines. Conveniently, this first unit can be executed independently from the others just once per simulation output, enormously reducing

---

[1]The source code of the presented version of PHOX is made available by request to the authors (see http://www.mpa-garching.mpg.de/ kdolag/Phox/). We also plan to make the code available directly for anonymous download in the near future.

[2]See http://www.gnu.org/s/gsl/.

[3]See http://heasarc.gsfc.nasa.gov/fitsio/.

the computational effort and time. The second unit of the code takes into account the geometry of the problem: the projection along a given line of sight is applied and photon energies are corrected for the Doppler Shift. The order of first and second unit basically reverses the approach of publicly available X–ray virtual telescopes and this has also the main advantage of delaying any limitation on spectral resolution as much as possible, preserving the possibility for any single photon to contribute to the final spectrum.

4.2.1   Numerical hydro–simulation input

PHOX requires as input the output of a hydrodynamical simulation. For the snapshots of the simulations we use, the redshifts and cosmological parameters are provided as well as the main quantities characterising the gas elements, such as density, temperature, metallicity, position and velocity. Currently, the simulator is best–suited to process simulations performed with SPH, particle–based codes, in particular outputs of the N–body/SPH code GADGET–2 (e.g. Springel et al., 2001; Springel, 2005). Nevertheless, the approach is very general and the code can be easily adapted to process also grid–based simulations, for instance performed with Adaptive Mesh Refinement codes like ART (Kravtsov, 1999; Kravtsov et al., 2002), ENZO (Norman et al., 2007, and references therein) or FLASH (Fryxell et al., 2000). In the description of the technique, we will preserve this generality and refer to the gaseous component in terms of more general emitting volumes, namely "gas elements", meaning that these could be either particles, as in the application presented in the following Sections 4.3 and 4.4, or grid cells.

4.2.2   Unit 1: generation of the box of photons

The first, essential unit is devoted to convert the simulation snapshot from a box of gas elements into a *box of photons*. It is crucial to perform this step before the projection is chosen and the emission is integrated along the line of sight in order to achieve and guarantee a very high spatial and spectral precision, accounting for the details of the three–dimensional structure of the source.

Given the density, temperature and metallicity (or abundances), the spectrum associated with each gas element of the simulation input is generated by means of the public available XSPEC package (v.12) [4]. In particular, since the ICM of galaxy

---

[4]See http://heasarc.gsfc.nasa.gov/xanadu/xspec/.
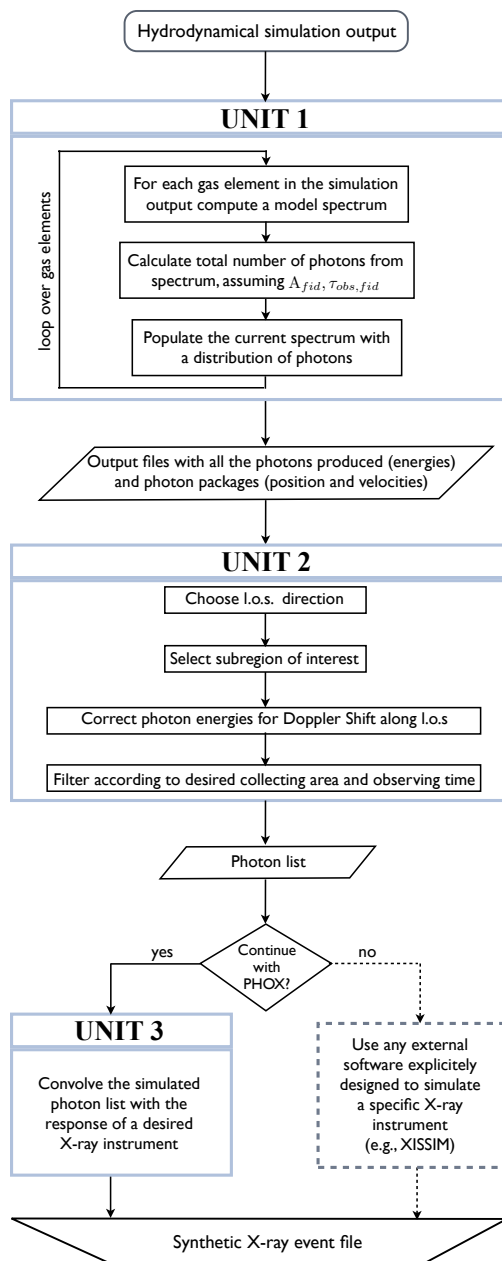
Figure 4.1: Flow chart illustrating the structure of PHOX. The dashed box represents the possibility to couple PHOX with any external software specifically designed to simulate observations with a certain X–ray telescope (e.g. the XISSIM simulator developed for the *Suzaku* satellite).

clusters is our primary target, the code assumes either a `MEKAL` (e.g. Mewe et al., 1985; Kaastra and Mewe, 1993; Liedahl et al., 1995) or an `APEC` (Smith et al., 2001) single–temperature, thermal emission model for the hot plasma, with the possibility to add an absorption component given by the `WABS` model (e.g. Morrison and McCammon, 1983). Nonetheless, the code can be readily adapted to account for any desired emission model that is suitable for the considered X–ray source (e.g. `VMEKAL`, `VAPEC`, `BAPEC`, `BVAPEC`, for more sophisticated descriptions of the ICM emission including also element abundances or velocity broadening for emission lines). At this stage, we do not convolve the model with any specific instrumental response but we use instead an identity matrix to provide very fine binning over a wide energy band. The choice of the model spectrum adopted, as well as of the energy limits and number of channels for the spectral binning, is left to the user, who can directly specify them in an input parameter file accepted by the code. Additionally, a fiducial angular–diameter distance to the source ($D_{A,fid}$) can be specified for convenience as an input parameter, instead of calculating it accordingly to the cosmological redshift of the simulation output.

The main calculation of this first unit consists of computing the emission associated to the gas component processing element per element, which even makes the code naturally suitable to parallelization. Our simulator directly populates the spectrum of each gas element with a distribution of photons, without storing every spectrum or building a library of template spectra. Specifically, we calculate a cumulative spectrum and perform a Monte–Carlo–like simulation to sample it with a total number of photons, N_{ph}, determined by the total counts expected from the spectral model (in units of photons/s/cm²) and the collecting area (A_{fid}) and observing time ($\tau_{obs,fid}$) specified by the user, so that

$$N_{ph} \propto A_{fid} \times \tau_{obs,fid}. \tag{4.1}$$

Ideally, the fiducial values for (A_{fid}) and ($\tau_{obs,fid}$) have to be assumed in a convenient way such that the spectra are largely over–sampled.

The photons are therefore characterised by energy (in the emitting element rest–frame), position and velocity. In order to reduce the amount of memory required to store the photon data, photons are organised in terms of packages, each package being associated to an emitting gas element. In this way, photon energies can be stored in a separate output file with respect to position and velocity, which in this first version of the code are

equal for all the photons emitted by the same gas element and therefore stored just once per package. Moreover, the data are therefore naturally compressed, since positions and velocities need to be recorded only for gas elements that indeed emit photons. The total number of photons produced from the whole gaseous component in the snapshot processed by PHOX is meant to be largely over–abundant in order to permit a dramatic reduction in the following units because of geometrical selection, projection and instrumental response.

The data generated from this basic part of PHOX represent a "cube of photons" associated to the input hydro–simulation. From this stage on, the simulator has all the information required to proceed with the synthetic observation and the original input is no longer needed. Therefore, it is worth to remark that this first unit can be processed once per output *independently* of the specific study to be performed.

4.2.3 Unit 2: projection and preparation for the observation

PHOX second unit takes into account the geometry of the observation to be simulated. It accepts the output data produced by the first unit and a parameter file with user–specified parameters for the sub–region of the cube that has to be selected, direction corresponding to the line of sight (l.o.s.), real collecting area and time for the mock observation.

After selecting geometrically the photons, the energies have to be corrected for the Doppler Shift in order to account for the line–of–sight velocity of the gas element that originally emitted them. In particular, the correction from the emitted to the observed frame is expressed as

$$E_{ph}^{obs} = E_{ph}^{em} \sqrt{\frac{1-\beta}{1+\beta}}, \tag{4.2}$$

where $\beta = v_{l.o.s.}/c$ and $v_{l.o.s.}$ is the velocity component along the line of sight. For the sake of simplicity, the line of sight is assumed to be aligned with the z–axis. Nevertheless, any different, desired direction only requires a simple rotation of the package positions and velocities before running this second unit of the code.

The sample of photons obtained has also to be further filtered according to the specified collecting area, A, and a realistic exposure time, $\tau_{\rm obs}$, chosen to simulate the observation. Accordingly to Eq. 4.1, this is done by calculating the re–scaling factor between these values and the fiducial quantities assumed in the first unit as

$$fak = \frac{A \ \tau_{\rm obs}}{A_{fid} \ \tau_{\rm obs,fid}} \times \frac{D_{A,fid}^2}{D_A^2}, \tag{4.3}$$

and by assuming it as a probability factor for each photon to be actually observed. Eq. 4.3 explicitly accounts for the possibility of re–scaling the number of observable photons by the angular–diameter distance to the source, D_A, whenever this parameter differs from the fiducial value, $D_{A,fid}$, adopted in Unit 1.

Lastly, the photon list has to be stored in the most convenient format either to be convolved with the technical response of the specific instrument or to interface with an external software dedicated to simulate specific X–ray satellites.

This second unit already takes into account the characteristics of the study to be performed but no longer requires the original simulation data, processed by Unit 1. Therefore, any change in the specification of the mock observation can be easily included in this post–processing phase. As such, a straightforward consequence is the unique possibility to investigate the same astrophysical source from many different line of sights, handily processing with Unit 2 the cube of virtual photons obtained with the first unit.

4.2.4   Unit 3: simulating the observation

At the third and last stage the mock X–ray observation is completed by eventually considering a real telescope. The photon list obtained from the second unit is convolved with the technical characteristics of a specific instrument, defined by the redistribution matrix file (RMF) and the ancillary response file (ARF). Such a process produces final event files which satisfy the standards of real X–ray observations, so that they can be analysed with the same procedures and tools used for real data.

In the most general perspective this last unit assumes the RMF and ARF files supplied by the user and it is not constructed a priori for a specific instrument. Particular attention, in general, has to be payed to the normalization of the effective area defined by the ARF file of the instrument with respect to the effective area assumed during the projection phase, in order to avoid unphysical overabundance of observed photons.

The third unit of the simulator, being independent of the others, can be conveniently replaced by any desired X–ray instrument simulator, like the sophisticated tool `XISSIM`[5], which has been developed especially to obtain synthetic observations of the *Suzaku* X–ray Imaging Spectrometer (Ishisaki et al., 2007).

---

[5]See http://heasarc.nasa.gov/docs/suzaku/prop_tools/xissim/xissim_usage.html.

4.3 Synthetic observation of the cosmic web: two cases of study

We present here an optimal application of PHOX to the hydro–numerical simulation of a filament–like structure. The large–scale region provides indeed a study case to test the remarkable gain in computational cost and time for the post–processing of large data sets; also, the cluster–like haloes residing in this simulated filament offer various science cases to perform the spectral analysis of the mock X–ray observations.

4.3.1 The simulated region

The high–resolution simulated region containing the supercluster–like structure extends for about $50 \times 50 \times 70 \, \mathrm{Mpc}^3$ and consists of 27 haloes at present epoch, four of them being massive cluster–size haloes. This filamentary region has been originally extracted from a cosmological, N–body simulation (Jenkins et al., 2001; Yoshida et al., 2001) of a ΛCDM universe with $\Omega_0 = 0.3$, $\Omega_b = 0.044$, $\sigma_8 = 0.9$ and $h = 0.7$, within a box of $479 h^{-1}$(comoving) Mpc a side. Using the "zoomed initial condition"(ZIC) technique (Tormen et al., 1997), the overdense region has been re–simulated at higher resolution and a hydrodynamical run with these new initial conditions has been performed with the TreePM/SPH code GADGET–2 (Springel et al., 2001; Springel, 2005), including cooling, star formation and feedback from supernova winds. The simulation output contains approximately 1.2×10^7 gas particles and 1.7×10^7 DM particles, at $z = 0$, and the final resolution is $m_{DM} = 1.30 \times 10^9 h^{-1} \, \mathrm{M}_\odot$ and $m_{gas} = 1.69 \times 10^8 h^{-1} \, \mathrm{M}_\odot$, for the DM and gas particles, respectively. For an extensive and detailed description of the simulation run and analysis we refer the reader to the paper by Dolag et al. (2006).

4.3.2 Suzaku mock observations with PHOX

We applied PHOX to the whole simulation output corresponding to redshift $z = 0.07$ and obtained from the first unit a list of all the photons emitted by the sufficiently–hot gas particles in the simulated region. In order to compute the model spectra, we adopted an `APEC` model with fixed metallicity, set for simplicity to $Z = 0.3 \mathrm{Z}_\odot$ for all the particles, and assumed the solar abundances by Anders and Grevesse (1989). The value assumed for the Galactic equivalent column density for the `WABS` absorption model was $N_H = 7 \times 10^{20} \, \mathrm{cm}^{-2}$. The values for fiducial collecting area and exposure time were initially

Table 4.1: Typical computational time scales and output storage memory for the hydrodynamical numerical simulation and different units of PHOX. As a representative case, the data reported here refer to the science application[†] presented in Section 4.3.

Sim	PHOX		
	Unit 1	Unit 2	Unit 3/XISSIM
	$\sim$1h 40min[*]	$\sim$few min	$\sim$few min
1.8 GB	827 MB	176 MB (CL2)	$\sim$100 MB (CL2)
		60 MB (CL1)	$\sim$35 MB (CL1)

[*]The run reported here has been performed by binning in temperature the particles (assuming $\Delta(kT) \sim 5eV$) and calculating a spectrum per bin, rescaling afterwards the expected total number of photons by the specific normalization calculated for each particle in the temperature bin. Since no varying metallicities have been considered in this run, this approach has been used to further reduce the computational effort.

[†]The results are obtained for serial runs performed on standard work station (2300 MHz, AMD Opteron).

set to $2000 \, \text{cm}^2$ and 1Ms, respectively. This first stage was the most computationally demanding (see Table 4.3.2 for time scales and memory requirements referring to the application presented here) and permitted to generate approximately 1.8×10^8 photons, for the whole simulation output.

In Unit 2, we assumed to observe the large–scale region from a physical distance[6] of $313.9 \, \text{Mpc}$, which corresponds to the luminosity distance at the snapshot redshift $z = 0.07$. Similarly, with the given cosmological parameters, the angular–diameter distance at this redshift is $274.4 \, \text{Mpc}$, which gives a physical scale of $1.33 \, \text{kpc/arcsec}$. In this projection phase, we select two specific sub–regions of the simulation box, containing two cluster–like haloes among the four most massive ones. In particular, we consider for the present analysis a regular, massive cluster (*hereafter*, CL1) with $M_{500} = 3.97 \times 10^{14} \, \text{M}_\odot$ and $R_{500} = 1070.5 \, \text{kpc}$ and a massive, disturbed system with $M_{500} = 9.24 \times 10^{14} \, \text{M}_\odot$ and $R_{500} = 1417.3 \, \text{kpc}$ (*hereafter*, CL2). The region geometrically selected around both haloes is a cylinder along the z–axis, enclosing R_{500} in the xy plane. Planning to simulate a Suzaku observation, the collecting area assumed for the mock observation equals the physical area of the *Suzaku* X–ray Imaging Spectrometer (XIS), A $= 1152.41 \, \text{cm}^2$, and the exposure time is $\tau_{obs} = 500 \text{ks}$, in order to have good statistics. This allows to extract 3.1×10^6 photons for CL1 and 9.2×10^6 photons for CL2.

In the left–hand panel of Fig. 4.2 we show the filament–like structure at $z = 0.07$, projected along the z–axis (i.e. the observation l.o.s.). The map represents the emission–weighted temperature of the simulated filament enclosed in the high–resolution region.

[6]We set the observer on the positive part of the z–axis, assumed to be aligned with the l.o.s..
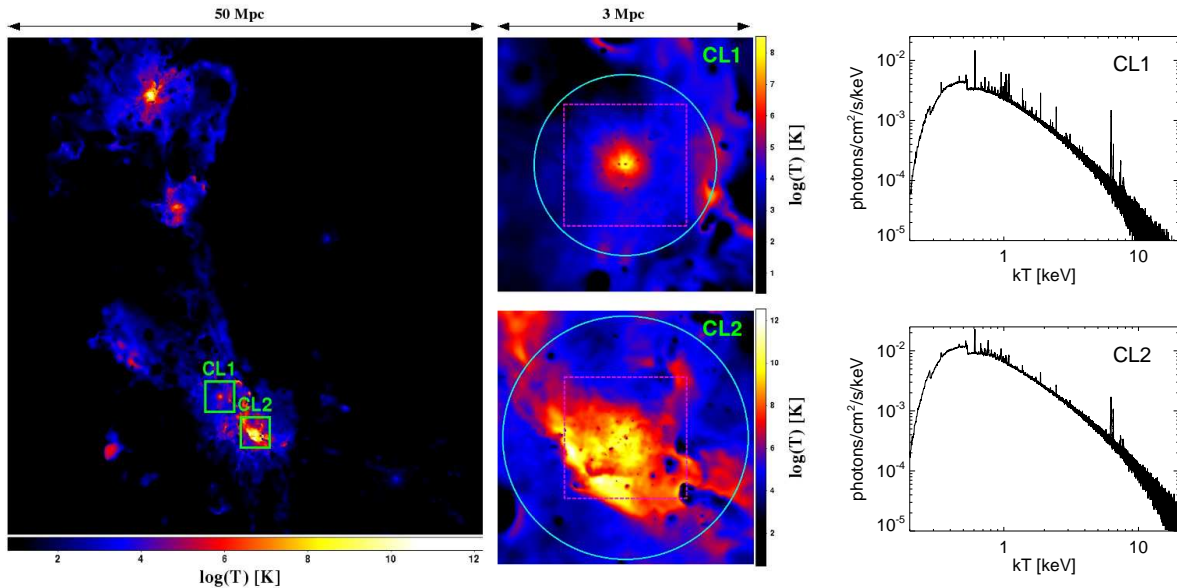
Figure 4.2: Filament–like region and zoom onto the haloes CL1 and CL2, at $z = 0.07$. Left–hand panel: projection along the z–axis of the emission–weighted temperature, in a logarithmic color scale. The map is $50\,\mathrm{Mpc}$ a side and encloses the high–resolution region of the box containing the filament. The $3 \times 3\,\mathrm{Mpc}^2$ regions centered on CL1 and CL2, respectively, are marked with the green squares. Central column: zoom onto CL1 (top panel) and CL2 (bottom panel). The maps are $3\,\mathrm{Mpc}$ a side and show the logarithm of the emission–weighted temperature, projected along the z-axis. The R_{500} region (cyan circle) and the XIS FOV (magenta dashed square) are overplotted for both haloes. Right–hand column: theoretical spectra obtained from Unit 1 and 2 of PHOX for the R_{500} region of both haloes.

Overplotted in green, we mark the zoom onto the selected haloes, which are shown in the central column of Fig. 4.2. The two panels contain in fact the $3 \times 3\,\mathrm{Mpc}^2$ maps of the emission–weighted temperature projected along the l.o.s., for CL1 and CL2. For comparison, we overplot also the R_{500} region (cyan circle) and the XIS field of view (magenta dashed square). Instead, in the right–hand column of Fig. 4.2 we show the ideal integrated spectra for CL1 and CL2, as obtained from Unit 1 and 2 after selecting the photons coming from the region enclosed within R_{500}. These spectra are obtained purely through a regular binning of the photon energies with bins of $\Delta E = 0.001\,\mathrm{keV}$, without including any sensitivity or effective area.

For the purpose of this paper, we present PHOX by taking advantage of the public package `XISSIM` (Ishisaki et al., 2007), designed to simulate observations with the XIS spectrometer on board the *Suzaku* X–ray satellite. By adapting the second unit of our code to produce the output photon list in a format best–suited for `XISSIM`, we test our novel technique and demonstrate its capabilities through a simple science application.

Specifically, we use `XISSIM` to process the simulated photons generated by PHOX with the real responses and calibration characteristics of different XIS CCDs. Given the high statistics offered by our simulation, we decide to consider the back–illuminated (BI: XIS-1) sensor and the two combined, front–illuminated CCDs (FI: XIS-0, -3) separately. The combination of two 500ks observations with the XIS-0 and XIS-3 detectors additionally improves the statistics for the final FI spectrum.

The event files obtained for the two cluster–like haloes of the filament, CL1 and CL2, without any addition of physical background emission, were then analysed following the standards of X–ray data analysis.

4.3.3   Spectral Analysis

In Fig. 4.3 we show the simulated photon images (left–hand column) of the 500ks XIS observations, with the BI and FI sensor, for CL1 and CL2. The images, as well as the spectra, were extracted from the original event files using `Xselect` (v.2.4) from the FTOOLS[7] package (Blackburn, 1995), and correspond to the central region in both clusters. In particular, the *Suzaku* XIS covers a field of view (FOV) of roughly $18' \times 18'$, which corresponds to a physical scale of 1436.6 kpc at the distance of our sources and encloses therefore the region within $\sim 0.67 R_{500}$ of CL1 and $\sim 0.51 R_{500}$ of CL2 (we refer to the central panels of Fig. 4.2 for a visual representation of the R_{500} region and the XIS FOV in the two haloes).

Simulations of cluster–like haloes provide the possibility of precisely knowing the intrinsic dynamical and thermal properties of the ICM. From a visual inspection of the temperature maps shown in Fig. 4.2 (central column), the different structure of the two haloes studied is already evident. As we will discuss in more detail in Section 4.4 (see Fig. 4.4), the further investigation of the emission measure (*hereafter*, E.M.) distribution as function of temperature, for the gas particles in the simulation that reside in the FOV of *Suzaku* both in CL1 and CL2, let us unveil the halo intrinsic thermal structures. Especially, CL1 is mainly dominated by one temperature component, although the E.M. distribution is not very narrow, whereas the second halo, CL2, clearly has a complex thermal structure, which cannot be well described by a single temperature.

Therefore, we fit a multi–temperature model to the BI and FI XIS spectra, restricting

---

[7]See http://heasarc.gsfc.nasa.gov/ftools/.
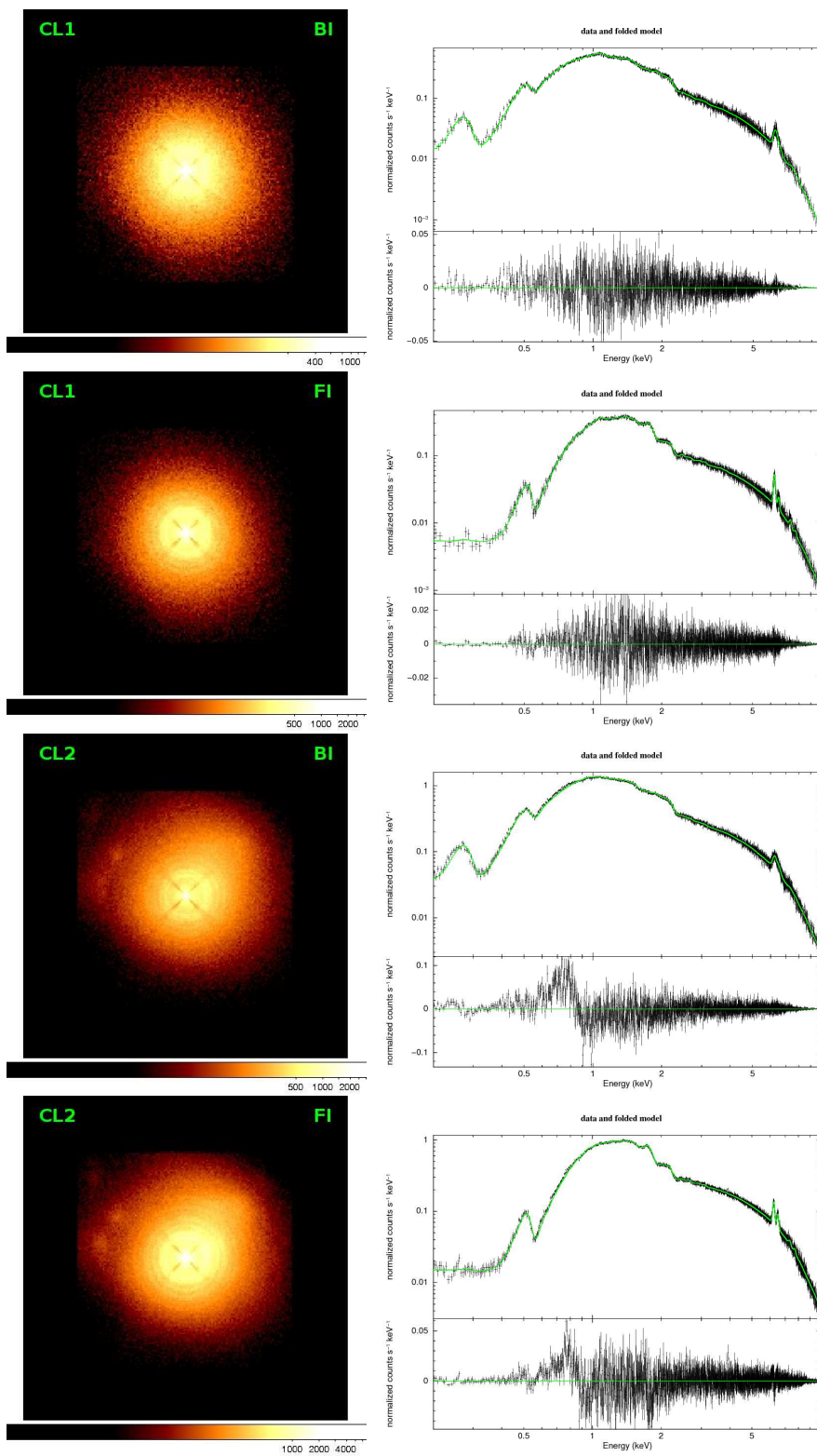
Figure 4.3: Simulated *Suzaku* images (left–hand column) of CL1 and CL2 and corresponding spectra (right–hand column). Also the models fitted to the spectra are shown. For each halo the BI XIS and the combined FI XIS sensors are presented.

our analysis to the $0.2 - 10$ keV energy band and requiring a minimum of 50 counts per energy bin. The spectral fit was performed with XSPEC 12.6.0 (Arnaud, 1996). The response files (RMFs) used in the fit were the same as in the run of XISSIM, while we generated the ARF files for each halo and detector by means of the ftool XISSIMARFGEN (Ishisaki et al., 2007).

For our spectral modelling of the simulated data, we considered a WABS $\times$ (APEC$_1$ + APEC$_2$ + APEC$_3$ + APEC$_4$ + APEC$_5$) model, describing each component by an APEC model, as assumed in Unit 1 for the emission associated to each gas element. The equivalent hydrogen column density for the Galactic absorption model WABS was frozen to $N_H = 7 \times 10^{20}$ cm^{-2}, as in the original run of Unit 1. For analogous reasons, we adopted fixed values for redshift, $z = 0.07$, and metallicity $Z = 0.3 Z_\odot$, always assuming the Anders and Grevesse (1989) solar abundances.

In both haloes, we assigned to the first temperature component, T_*, a value fairly close to the emission–weighted temperature estimated from the gas particles in the simulation. Then, following a strategy similar to what is suggested by Peterson et al. (2003) or Kaastra et al. (2004), we assigned to the other components temperatures of $2T_*$ and $\frac{1}{2}T_*$, $\frac{1}{4}T_*$, $\frac{1}{8}T_*$, for the cooler ones. The five normalizations of the APEC components where free parameters in the fit.

The spectra and best–fit models are shown in the right–hand column of Fig. 4.3, for the two haloes and the two XIS sensor kinds. The results of the spectral fit are presented in Table 4.3.3. The five temperatures, frozen in the fit, are different for CL1 and CL2 and therefore reported in the table for clarity reasons. Overall, the resulting χ^2_{red} is always very good, meaning that the five–temperature model provides a fair description of the thermal structure for both clusters in the central observed region.

Table 4.2: Multi–temperature best–fit results for *Suzaku* XIS simulated spectra of haloes CL1 and CL2. The model adopted is WABS × (APEC$_1$ + APEC$_2$ + APEC$_3$ + APEC$_4$ + APEC$_5$), where only the normalizations K_i are free in the fit.

XIS	$K_1^\star$	K_2	K_3	K_4	K_5	$\chi^2/d.o.f.$
			CL1			
	$(kT_1 = 0.69\,\text{keV})$	$(kT_2 = 1.38\,\text{keV})$	$(kT_3 = 2.75\,\text{keV})$	$(kT_4 = 5.5\,\text{keV})$	$(kT_5 = 11\,\text{keV})$	
BI	$0.21(\pm0.04) \times 10^{-3}$	$0.15(\pm0.16) \times 10^{-3}$	$2.03(\pm0.60) \times 10^{-3}$	$8.17(\pm0.63) \times 10^{-3}$	$1.38(\pm0.54) \times 10^{-3}$	1693.2/1700
FI	$0.27(\pm0.04) \times 10^{-3}$	$0.12(\pm0.14) \times 10^{-3}$	$2.00(\pm0.44) \times 10^{-3}$	$8.12(\pm0.43) \times 10^{-3}$	$1.47(\pm0.36) \times 10^{-3}$	1713.2/1998
			CL2			
	$(kT_1 = 1\,\text{keV})$	$(kT_2 = 2\,\text{keV})$	$(kT_3 = 4\,\text{keV})$	$(kT_4 = 8\,\text{keV})$	$(kT_5 = 16\,\text{keV})$	
BI	$0.99(\pm0.09) \times 10^{-3}$	$0.0(\pm0.91) \times 10^{-3}$	$7.87(\pm1.70) \times 10^{-3}$	$16.44(\pm2.28) \times 10^{-3}$	$7.87(\pm1.41) \times 10^{-3}$	2762.0/2167
FI	$1.16(\pm0.09) \times 10^{-3}$	$0.0(\pm0.70) \times 10^{-3}$	$7.49(\pm1.21) \times 10^{-3}$	$16.14(\pm1.52) \times 10^{-3}$	$8.32(\pm0.90) \times 10^{-3}$	2557.3/2435

*The normalization of an APEC component is defined as $K = 10^{-14} \int n_e n_H dV / [4\pi D_A^2 (1+z)^2]$ cm^{-5}, where D_A is the angular–diameter distance to the source.

4.4   Results: recovering the emission measure distribution

The interesting purpose of our multi–temperature modelling is the reconstruction of the thermal structure of the emitting ICM. This is pursued by directly comparing the distribution of the best–fit normalizations at the corresponding, fixed temperatures with the expected values calculated from the simulation. Dealing with simulated data, we can faithfully test the results of the spectral analysis against the underlying solution in a straightforward way, which is not possible for real data.

By definition, the normalization of each `APEC` component is

$$K = 10^{-14}\text{E.M.}/[4\pi D_A^2(1+z)^2] \ \text{cm}^{-5}, \qquad (4.4)$$

where D_A is the angular–diameter distance to the source and z is the redshift. This implies that the normalization is directly proportional to the E.M. of the hot emitting plasma, defined as

$$\text{E.M.} = \int n_e n_H dV, \qquad (4.5)$$

where n_e and n_H are the electron and hydrogen number densities of the plasma, respectively. In order to map the distribution of E.M. in the simulated haloes to the corresponding K values at fixed temperatures, the theoretical temperature binning has to be determined in the most faithful way possible.

The shape of the E.M. distribution extracted from the simulation is presented for the two haloes in the left–hand panels of Fig. 4.4. This has been calculated considering all the gas particles of the simulated haloes, for which the projected position on the xy plane is enclosed in the *Suzaku* field of view. A lower temperature cut has been artificially set to $T_{min} = 0.2\,\text{keV}$, which is the lower boundary of the energy band used in the spectral fit. Nevertheless, this continuous distribution has to be reduced to the five fixed temperatures adopted for the spectral fit. The most consistent and independent way of choosing the boundaries between the different temperature components, is by requiring that the value of the E.M.–weighted temperature for each bin equals the fixed value adopted for the fitting (we follow here an approach analogous to the one adopted by Kaastra et al. (2004)). Specifically, we iteratively adjust the division boundaries until the match between the E.M.-weighted temperature in the bin and the fixed value is reached, starting from the lower–temperature component and proceeding towards the higher ones.

Finally, the total E.M. calculated in each bin can be converted into an expected value for the `APEC` normalization via Eq. 4.4.

The direct comparison between simulation and mock–observation results is presented in the right–hand panels of Fig. 4.4, for both CL1 and CL2. The original E.M. distribution for the two haloes is plotted in the left–hand panels of Fig. 4.4, where it is clear that none of them is strictly isothermal, although the CL1 cluster has a narrower thermal distribution with respect to CL2. The theoretical expectations for the fixed temperature components are plotted as black asterisks on the right–hand panels, where the best–fit values are reported as well.

Interestingly, the agreement between simulated and "observed" values is quite good
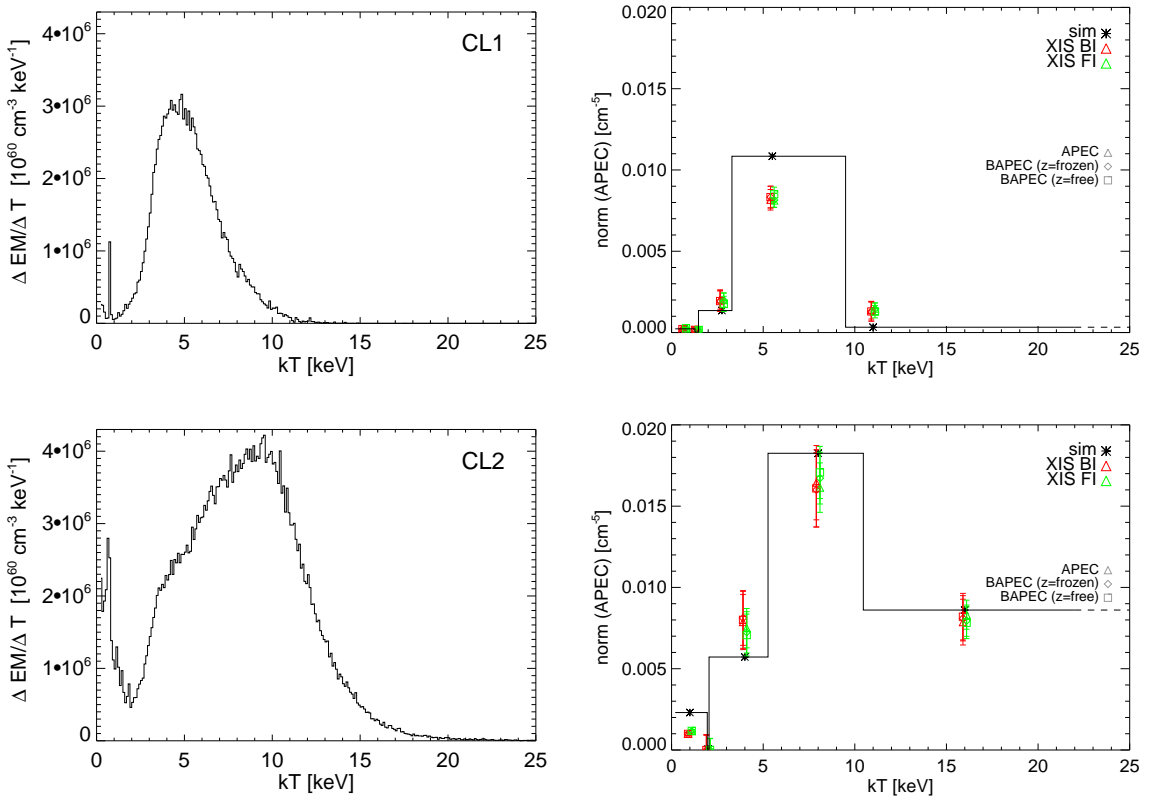
Figure 4.4: Left–hand column: emission measure (E.M.) distribution as a function of temperature for gas particles contained in the FOV of Suzaku XIS (projected along the z–axis), for haloes CL1 and CL2 at redshift $z = 0.07$. Right–hand column: comparison between best–fit values of APEC (triangles) and BAPEC (–1, diamonds and –2, squares) normalizations and corresponding theoretical values (asterisks), computed from the E.M. distribution of emitting gas particles. Different colors for the best–fit values refer to spectra obtained with different XIS detectors: BI XIS (red), and FI XIS (sum of XIS-0 and XIS-3, green). In both columns, the upper row refers to CL1 and the lower row refers to CL2.

and the overall shape of the thermal distribution in both clusters is recovered reasonably well. This result is found to be true for both the BI and FI XIS sensors. Moreover, the differences between the thermal structures of the two haloes are reflected by a different width and extension of the E.M. distribution over temperature, which is definitely broader in the CL2 case.

We notice that the dominant component at $kT_4 = 5.5\,\mathrm{keV}$ is underestimated by the fit for the halo CL1. Nonetheless, it is worth to notice that the determination of the most consistent temperature binning of the theoretical E.M. distribution is expected to be sensitive to the definition of temperature assumed to match the temperature of the thermal component in the spectral fit. For instance, it is known that there is a discrepancy between the emission–weighted temperature, as usually calculated in the analysis of numerical simulations, and the projected spectroscopic temperature obtained from X–ray observations (see, for instance, Mazzotta et al., 2004). In this respect, our choice for the theoretical temperature calculated from the simulation, which is weighted by the E.M., is believed to be the most consistent. However, we also tested the results against a different definition of temperature, namely the emission–weighted[8] one, which resulted in a slightly different set of theoretical values for the five `APEC` normalizations. Even in this case, our conclusions are not affected in any significant way and the overall shape of the underlying E.M. distribution is equally well traced by the multi–component spectral fit.

In the right–hand plots of Fig. 4.4 we also show two alternative five–temperature models adopted to fit the synthetic spectra. Specifically, we perform two spectral fits with a multi–temperature model consisting of five `BAPEC` components. The `BAPEC` spectral model is a velocity– and thermally–broadened emission spectrum, where the velocity broadening is parametrized by a Gaussian velocity dispersion σ_v. In fact, the technique implemented in our simulator allows to preserve the very high energy resolution of the integrated spectrum till the final convolution with the instrument. Since every photon energy carries the imprint of the emitting particle velocity, the

---

[8]The emission–weighted temperature is defined as

$$T_{ew} = \frac{\int n^2 \Lambda(T) T dV}{\int n^2 \Lambda(T) dV},$$

where n is the gas density and $\Lambda(T)$ is the cooling function. As usually done, we consider here $\Lambda(T) \propto T^{\frac{1}{2}}$, assuming the gas to emit mainly via Bremsstrahlung.

spectral features like metal emission lines could include a non-thermal broadening due to peculiar non–thermal motions of the gas particles of the ICM and the velocity–broadened `APEC` is a valid choice to take this into account. In the two cases explored with the $\mathtt{WABS} \times (\mathtt{BAPEC_1} + \mathtt{BAPEC_2} + \mathtt{BAPEC_3} + \mathtt{BAPEC_4} + \mathtt{BAPEC_5})$ model, every frozen parameter was assumed in the same manner as in Section 4.3.3 and the five `BAPEC` normalizations were let be free. In addition, in the first model (`BAPEC`–1), we fit for another free parameter, which is the velocity dispersion σ_v linked across the five components, whereas in the second case (`BAPEC`–2) both σ_v and the redshift are left free in the fit. As shown in the plots, the results for the normalizations are definitely consistent with the standard case, where the five thermal components are described by the `APEC` model. However, the best–fit values for σ_v, in particular, turn out to have very large errors, meaning that this additional parameter is not reliably fitted. We interpret this as an evidence that the energy resolution of the *Suzaku* XIS spectrometer is not sufficiently high to capture the details of the emission lines and therefore a velocity–broadened model like `BAPEC` is not improving the fit to the synthetic data.

Moreover, the results look generally stable against metallicity, which could in principle compete with normalization in order to reproduce the spectral features associated to metal emission lines. In particular, we tested the fit with five `APEC` models, both for CL1 and CL2, allowing for the metallicity value to be free, although linked across the five components, in addition to the five normalizations. Generally, this converges to values within few percents from the expected metallicity of $Z = 0.3 Z_\odot$, used in the simulation of the X–ray observation. Comparing to the results of the standard fit reported in Table 4.3.3, the `APEC` best–fit normalizations, for initial metallicity values set to $[0.2, 0.3, 0.5] Z_\odot$, are found to be consistent with the original values, within the error bars associated to them.

4.5   Discussion and conclusion

In this paper, we have presented a novel X–ray photon simulator, named PHOX[9], dedicated to obtain synthetic X–ray observations from the output of hydrodynamical numerical simulations.

---

[9]The source code of the presented version of PHOX is made available by request to the authors (see http://www.mpa-garching.mpg.de/ kdolag/Phox/). We also plan to make the code available directly for anonymous download in the near future.

The development of PHOX has been strongly motivated by the ultimate aim of comparing the output of hydrodynamical simulations of cluster–like objects to real X–ray observations in the most faithful and reliable way possible. In fact, X–ray observations still provide us with increasingly detailed data that require a deep understanding of the underlying structure of galaxy clusters. Numerical simulations, on the other side, continuously improve in describing not only the dark matter but also the complex physical processes governing the baryonic component. Therefore, a strategy devoted to combine the advances and results in both observations and simulations can be promisingly successful.

In the past, software packages like X–MAS (Gardini et al., 2004) or XIM (Heinz and Brüggen, 2009) have been developed to produce synthetic observations of astrophysical sources simulated with particle– and grid–based codes, respectively. The existence of such tools is definitely complementary to our simulator in order to test the robustness of comparison studies between state–of–the–art hydrodynamical simulations including different physical phenomena and real observations. With respect to other codes, the novelty of our virtual telescope resides in the original method implemented. In particular, the order of the three main units that constitute the code offers a significant gain in computational cost and time, making PHOX extremely flexible and useful to process hydro–numerical simulations of several astrophysical objects, at various spatial scales, as well as simulated light–cones. Moreover, this method uniquely guarantees extremely high spatial and energy resolution. The more demanding phase is indeed the first one, where the output of a hydrodynamical simulation is processed and the X–ray emission of each gas element (either particle or grid cell) is simulated by using the spectral models available in the X–ray software `XSPEC`. Essentially, we perform the sampling of each spectrum with an expected number of photons, and we immediately store the sample of photons instead of constructing a library of template spectra to be populated afterwards. As such, the spectral model chosen to mock up the emission from the gas elements, regardless of its complexity, can be explicitly specified and suited to represent any desired astrophysical source. Also, the relatively reasonable requirements in terms of computational time and memory, make out of PHOX an ideal tool to process forthcoming large cosmological, hydrodynamical simulations as well as the usual smaller ones.

Concerning galaxy clusters, PHOX currently uses two possible models for the X–ray

emission of the ICM (namely, `MEKAL` and `APEC`) and accounts for the particular density and temperature of the simulated gas elements. However, the technique implemented offers the chance to account also for different metallicities, or even metal compositions, across the emitting gas elements, without increasing the memory requirements significantly.

Furthermore, PHOX postpones the projection along the line of sight and the convolution with a real instrument response till after the generation of the discrete sample of photons, permitting to each of them, in principle, to contribute to the final integrated spectrum. Requiring a high energy resolution in the model spectrum associated to every gas element, we can ideally combine the potential of PHOX with the characteristics of upcoming X–ray satellites, like IXO/ATHENA or ASTRO–H, in order to predict the detectability of fundamental spectral features. This could be of great help, for instance, in constraining the ICM non–thermal motions (e.g. turbulent, bulk, rotational motions) via the velocity broadening of heavy–ion emission lines. In general, the theoretical modelling of X–ray–emitting sources is a powerful way to predict and optimize the capabilities of future X–ray missions and to help in the interpretation of the data when the instruments are in operation.

As an interesting application of this new virtual telescope, we focused on the hydro–numerical simulation of a large–scale region, originally performed with the TreePM/SPH code GADGET–2 and then re–simulated including cooling, star formation and feedback from supernova winds. This filament–like structure is particularly worthy for presenting the simulator in each part and especially for demonstrating the advantages of our approach. From a purely technical perspective, the greatest gain was achieved in terms of computational cost since the entire, large data cube contained in the simulation output was processed with PHOX Unit 1 only once, providing an output of relatively compacted photon data (see Table 4.3.2). In fact, this first phase permitted to obtain the X–ray photons virtually emitted by all the gas particles in the filament. At a later stage, we restricted our analysis to two cluster–like haloes with different thermodynamical structure, CL1 and CL2, which were geometrically selected from two different regions of the simulation box. Conveniently, the projection and observation units of PHOX could be run separately for each halo processing the same output generated with Unit 1 and we finally obtained synthetic *Suzaku* images and spectra (Fig. 4.3). The convolution with the response of the X–ray Imaging Spectrometer (XIS) on board *Suzaku*, via the

public tool XISSIM, provided data that could be analysed with the standard procedures of X–ray analysis. An important aim of this application was the reconstruction of the intrinsic emission measure distribution by the multi–temperature fitting of the simulated spectra. The goal of setting spectroscopic constraints on the multi–phase ICM of galaxy clusters was pursued in X–ray observational studies reported by Peterson et al. (2003), Kaastra et al. (2004) and Fabian et al. (2006), although for real clusters it is intrinsically impossible to know the underlying multi–phase structure unambiguously. Instead, numerical simulations uniquely allow to model and predict the theoretical temperature distribution of the ICM (e.g., studied in Kawahara et al., 2007, 2008) and constitute therefore the ideal possibility to test the power of the method used to reconstruct the structure of the mock data. The direct comparison between the X–ray data and the theoretical thermal distribution of the input simulation is found to be overall faithful and robust for both CL1 and CL2 (see Fig. 4.4). Moreover, the different thermal structure that distinguishes the two selected haloes is remarkably highlighted by the multi–temperature fitting. This result promisingly suggests that the temperature distribution of the ICM can be in principle traced and unveiled by spectral analysis of X–ray observations. From the additional investigation of velocity–broadened fitting models (like the BAPEC model) for the *Suzaku* spectra, we can also conclude that a higher spectral resolution is required in order to reliably constrain the ICM velocity structure. In general, it is important to notice that the application discussed here does not include other emission components (e.g. a physical X–ray background) in addition to the ICM one and represents therefore an ideal case study.

With regard to technique, the main feature distinguishing PHOX from other virtual X-ray telescopes, such as XMAS and XIM, is the explicit creation and storage of a 3–dimensional box of photons from the raw simulation data cube itself. This step is performed *before* and without any reference to the observation process and its result is stored as a separate data product, which represents the ideal X–ray emission from all the gas volumes in the simulated region, allowing us to employ Unit 1 of PHOX to create a photon database associated to the simulation. In Unit 2 this photon cube is projected onto a particular observational plane and the photons are sampled according to the chosen aperture and observation time, as described in Eq. 4.3. With the photon box pre–calculated, this step is computationally trivial and can be performed very efficiently.

As such, it could in fact be made available through an on line web service. The result of this step is a photon list and is processed in this paper by means of the *Suzaku* simulator XISSIM. Similarly, we believe it should be possible for most such virtual telescopes to be adapted to the same format without undue difficulties.

This leads us to an interesting modular design, with a photon simulator producing a list of photons directly from a hydrodynamical simulation, and a virtual telescope receiving this list, and convolving it with the characteristics of a real X–ray instrument to produce a photon event file that can be directly compared in all its aspects to the analogous files resulting from real observations. This design presents a proper separation of concerns between theorists and observers, where each module is clearly independent from the others and can therefore be implemented and used separately. In a larger perspective, the well specified model for the data shared and exchanged between these units could represent a first step towards a standardised, interoperable way to publish simulation results in a way that is suitable for investigation by observers. In particular, this is very suitable for the kind of approach pursued by the International Virtual Observatory Alliance (IVOA[10]), and we indeed plan to deploy a web service that provides access to the results discussed in this paper in that context[11].

---

[10]http://www.ivoa.net
[11]Please check http://www.mpa-garching.mpg.de/HydroSims for updates on this service

Chapter 5

Observing simulated galaxy clusters with PHOX: the prospects of velocity diagnostics of the ICM

Veronica Biffi, Klaus Dolag, Hans Böhringer
To be submitted

Non–thermal motions in the intra–cluster medium (ICM) are believed to play a non–negligible role in the pressure support to the total gravitating mass of galaxy clusters. Future X–ray missions, such as ASTRO–H and ATHENA, will eventually allow us to directly detect the signature of these motions from high–resolution spectra of the ICM. In this paper, we present a study on a set of clusters extracted from a cosmological hydrodynamical simulation, devoted to explore the role of non–thermal velocity amplitude in characterising the cluster state and the relation between observed X–ray properties. In order to reach this goal, we apply the X–ray virtual telescope PHOX to generate synthetic observations of the simulated clusters with both Chandra and ATHENA. From Chandra spectra we extract global properties, e.g. luminosity and temperature, while we accurately estimate the gas velocity

dispersion achievable from the broadening of emission lines from heavy ions (e.g. Fe) resolved in ATHENA spectra. Given the good agreement found between simulations (true, intrinsic solution) and mock observations (detectable amplitude of non–thermal velocities), we further extend the analysis to the relation between non–thermal velocity dispersion of the gas and the $L_X - T$ scaling law for the simulated clusters. Interestingly, we find a clear dependence of slope and scatter on the selection criterion for the clusters based on the level of non–thermal motions. Namely, the scatter in the relation

is significantly reduced by the exclusion of the haloes, for which we estimate the highest turbulent velocities. Such velocity diagnostics appears therefore as a promising independent way to identify disturbed clusters, in addition to the commonly used morphological inspection.

5.1   Introduction

During the mass assembly in galaxy clusters, interactions between sub–haloes and merging events can generate substantial streaming motions and turbulence in the hot gas filling the cluster potential well. Additionally, a number of processes taking place in galaxy clusters, especially in the inner regions, are most likely responsible for the transfer of energy from large modes into smaller modes, causing rotation, streaming and, mainly, turbulent motions to establish in the intra–cluster medium (ICM). Among these physical processes, mergers and sloshing of dark matter cuspy cores are believed to cause large scale motions, and, in addition, the AGN activity and its interaction with the surrounding gas can cause turbulence in the central region.

Numerically, the non–thermal components of ICM motions have been investigated by means of hydrodynamical simulations of galaxy clusters, which uniquely provide full 3D information on the gas velocity field. The establishment of ICM bulk, streaming and rotational motions during the growth and assembly of simulated galaxy clusters is believed to contribute, especially in the central part of the systems, to the cluster pressure support and therefore to the virial estimate of the total mass up to significant fractions (e.g. Pawl et al., 2005; Fang et al., 2009; Lau et al., 2011; Biffi et al., 2011). Moreover, several studies on SPH and AMR simulations of cluster–like haloes have addressed the turbulent velocity field in clusters, estimating the pressure support due to chaotic motions to be of order of $\sim 20 - 30\%$ of the total pressure (e.g. Norman and Bryan, 1999; Dolag et al., 2005; Iapichino and Niemeyer, 2008; Iapichino et al., 2011; Vazza et al., 2009, 2011). Tighter constraints on the gas velocity field are necessary in order to obtain precise measurements of the total gravitating mass, which is the most important, intrinsic quantity to determine. In particular, the account for non–thermal motions is essential for mass estimates based on X–ray global properties (e.g. gas density and temperature), via the assumption of hydrostatic equilibrium (e.g. Rasia et al., 2006, 2012; Piffaretti and Valdarnini, 2008).

The presence of non–thermal motions in the gas velocity field within galaxy clusters is also suggested by several observational evidences, coming from radio observations of polarized synchrotron emission in cluster radio galaxies (e.g. Cassano and Brunetti, 2005; Bonafede et al., 2010), measurements of the resonant scattering effects (Churazov et al., 2010; Zhuravleva et al., 2010) and study of the fluctuations in pressure (Schuecker et al., 2004) and surface brightness (Churazov et al., 2011) maps, obtained with X–ray telescopes. However, mainly indirect indications of ICM turbulence have been possible so far. Only with the XMM–Newton RGS spectrometer weak upper limits have been set on the turbulent velocities in a set of galaxy clusters, as recently discussed in Sanders et al. (2011).

Future X–ray missions like ASTRO–H or ATHENA will allow us to achieve direct estimations of the ICM non–thermal velocities with great accuracy, thanks to the high spectral resolution expected to be reached. In fact, X–ray high–precision spectroscopy potentially offers one of the most promising ways to directly measure such gas motions, detectable from the detailed study of the shape and centroid of resolved spectral emission lines.

Theoretically, the non–thermal component of the gas velocity, along the line of sight (l.o.s.), can be very well constrained by studying the shape of heavy–ion emission lines in the X–ray spectra, for which the broadening can be significantly more sensitive to non–thermal velocities of the gas rather than to thermal motion (e.g. Rebusco et al., 2008). The expectations for such line diagnostics are related in particular to the most prominent emission line in X–ray spectra, namely the $\sim 6.7\,\mathrm{keV}$ line from helium–like iron. In fact, the large atomic mass of the FeXXV ion significantly reduces the thermal line broadening, so that the line width turns out to be definitely more sensitive to turbulent or bulk gas motions (Inogamov and Sunyaev, 2003; Sunyaev et al., 2003).

Here we discuss the prospect of using high resolution spectra to detect the amplitude of non–thermal gas motions with the aim of characterising more precisely galaxy clusters and observed relations between their X–ray properties, like the $L_X - T$ scaling relation.

To this scope, we employ a set of numerically simulated clusters, obtained with the TreePM/SPH parallel code P–GADGET3 including a large variety of physical processes to describe the baryonic component, and perform X–ray synthetic observations of the haloes with PHOX (Biffi et al., 2012). The paper is structured as follows: first, we

will describe the simulated dataset of galaxy clusters (Section 5.2) and the generation of mock X–ray spectra with the Chandra and the up–coming ATHENA telescopes. In Section 5.3, we will describe the analysis performed to obtain global properties, such as luminosity and temperature, from the Chandra spectra and to estimate the gas, non–thermal velocity dispersion, from the velocity broadening of the iron lines in the high–resolution ATHENA spectra. The analysis on the gas velocity dispersion, calculated directly from the simulation, is presented in Section 5.4.1. The comparison against the detectable velocities obtained from the synthetic ATHENA spectra is then discussed in Section 5.4.2. Using the Chandra mock observations, we explore the $L_X - T$ scaling relation for the simulated clusters in Section 5.4.3 and we discuss the effects on the best–fit relation and its intrinsic scatter, due to the non–thermal fraction of the ICM motions. Our conclusions are finally summarized in Section 5.5.

5.2   The sample of simulated clusters

The sample of simulated cluster–like haloes analysed here has been singled out from a cosmological, hydrodynamical simulation performed with the TreePM/SPH, parallel code P–GADGET3. In this extended version of GADGET2 (Springel et al., 2001; Springel, 2005), a vast range of baryonic physics, at a high level of detail, is included, such as cooling, star formation and supernova–driven winds (Springel and Hernquist, 2003), chemical enrichment from stellar population, AGB stars and SNe (Tornatore et al., 2004, 2007), thermal conduction (Dolag et al., 2004), low–viscosity SPH (Dolag et al., 2005), black–hole growth and feedback from AGN (Springel et al., 2005a; Fabjan et al., 2010). The simulated box has a side of $352h^{-1}$ Mpc, in comoving units, resolved with 2×594^3 particles, which results in a mass resolution of $m_{DM} = 1.3 \times 10^{10}$ and $m_{gas} = 5.2 \times 10^8$, for dark matter (DM) and gas particles, respectively. For the simulation, and throughout the following, the cosmology assumed refers to the 7–year WMAP estimates (Komatsu et al., 2011), i.e. $\Omega_0 = 0.268$, $\Omega_\Lambda = 0.728$, $\Omega_b = 0.044$, $\sigma_8 = 0.776$ and $h = 0.704$.

The sample of clusters consists of 43 objects, selected among the most massive haloes in the simulated box, for a snapshot of the simulation at $z = 0.213$. The selection criterion adopted requires the total mass, M_{500}, encompassed by R_{500}[1], to be $> 3 \times 10^{14} h^{-1} \, M_\odot$,

---

[1]Note that R_{500} is defined here as the radius enclosing the region of the cluster whose mean density is 500 times the mean density of the Universe. This encompasses therefore a larger region with respect to the usual definition of R_{500}, where the overdensity is instead defined with respect to the *critical* density of the Universe.

at the redshift considered.

5.3 X–ray synthetic observations

The mock X–ray observations have been performed for the selected haloes of the sample by means of the virtual X–ray simulator PHOX. For a detailed description of the method implemented in PHOX, we refer to (Biffi et al., 2012).

5.3.1 Generation of the virtual photon lists

The snapshot of the hydrodynamical simulation considered, referring to redshift $z = 0.213$, has been first processed with Unit 1 of PHOX as a whole, generating the virtual photon cube associated to the X–ray emitting gas component in the simulated cosmic volume.

For all the gas particles, model spectra have been calculated and sampled with packages of photons, each of them in the restframe of the corresponding emitting particle. The model adopted to calculate each theoretical spectrum was an absorbed, single–temperature `VAPEC`[2] model (Smith et al., 2001), implemented in `XSPEC`[3] (Arnaud, 1996). Temperature, density and chemical abundances (see Appendix 5.6.1, for details on the implementation of metal composition in PHOX) are obtained directly from the hydro–simulation output. Additionally, we fixed the redshift at the value of the simulated data cube and the equivalent hydrogen column density for the `WABS` absorption model (Morrison and McCammon, 1983) to a fiducial value of $10^{20}\,\mathrm{cm}^{-2}$. At the end of this first stage, the photon database associated to the simulation output contains roughly 10^7 photon packages ($\sim 10^9$ photons, in total), for fiducial values of collecting area and exposure time of $1000\,\mathrm{cm}^2$ and 1Ms, respectively.

With PHOX Unit 2 we then assume to observe the photons from a line of sight (l.o.s.) aligned with the z–axis of the simulation cube and correct photon energies for the Doppler Shift due to the emitting–particle motions along this l.o.s.. During this geometrical stage of the process, we also select cylindrical sub–regions along the l.o.s., corresponding to the selected 43 selected cluster–like haloes. For each cluster halo, the selected sub–region is centered on the centre of mass and encloses the region within R_{500}, in the xy plan, throughout the box depth (along the z–axis). For the time frame considered here and

---

[2]See http://heasarc.gsfc.nasa.gov/xanadu/xspec/manual/XSmodelApec.html.
[3]See http://heasarc.gsfc.nasa.gov/xanadu/xspec/.

the cosmology used, the luminosity distance between the observer, positioned along the positive z–axis, and the observed region is 1047.6 Mpc, in physical units. Typically, we obtain $1 - 2 \times 10^6$ photons per halo.

The photon lists produced in this general way, are convolved by PHOX with real instrumental responses of Chandra and ATHENA, assuming an exposure time of 100ks. The synthetic spectra are fitted by means of the X–ray package XSPEC v.12.6.0 (Arnaud, 1996).

5.3.2   Chandra synthetic spectra

To create Chandra synthetic spectra, we use the ARF and RMF of the Chandra ACIS–I3 detector aimpoint. The FoV of Chandra, which is $17' \times 17'$, corresponds to a physical scale of 3.52 Mpc per side, for the given cosmology and redshift. This encloses typically the region within $1 - 1.2R_{500}$ for most of the clusters in the sample, except for the 7 most–massive haloes, for which the Chandra FoV captures a region slightly smaller than the one out to R_{500}. In such cases, however, one can in principle compose a mosaic with multiple Chandra pointings in order to cover the clusters up to R_{500}. Therefore, we convolve the photon lists corresponding to the whole R_{500} region with the response of Chandra and analyse the corresponding spectra, for all the cluster in the sample.

Temperature and bolometric luminosity

We fit Chandra spectra either with an absorbed, single–temperature or with a two–temperature APEC model, depending on the goodness of the single–temperature fit. The spectra are re–grouped requiring a minimum of 10 counts per energy bin. Whenever the spectral fit was still poor, spectra were instead re–grouped with a minimum of 20 counts. The absorption is fixed to the fiducial value adopted to generate photons. Given the characteristics of the Chandra response, we assumed the redshift to be fixed at the initial value of the simulation and only temperature, metallicity and normalization were free in the fit.

From the spectral best fit in the $0.5 - 10$ keV range we directly obtain the temperature of the cluster[4].

---

[4]In the case of haloes fitted with a two–component model, we assume here the hotter temperature to be representative of the dominant gas component.
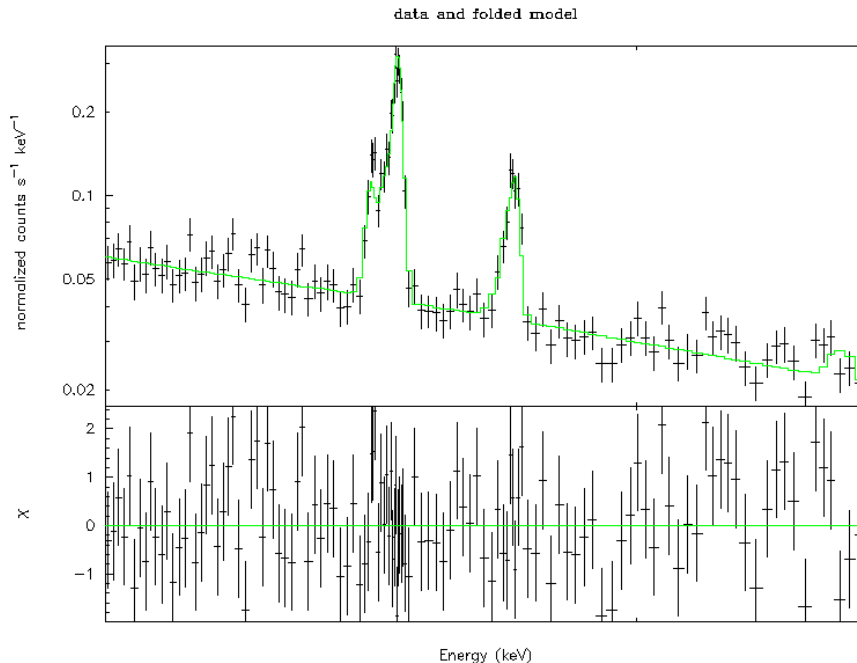
Figure 5.1: Zoom onto the $5 - 6.5$ keV energy band, containing the iron lines (at the rest–frame energy ~ 6.7 keV and ~ 6.96 keV), from the synthetic ATHENA XMS spectrum of one of the sample cluster. In the figure we show the best–fit `BAPEC` model to the data (green curve).

The total X–ray luminosity, L_X, is extrapolated from the best–fit spectral model out to the entire energy range defined by the ACIS–I3 detector response, to obtain an approximate bolometric luminosity.

5.3.3 ATHENA synthetic spectra

ATHENA spectra are simulated from the ideal photon lists of the 43 haloes in the sample by using the latest RSP response matrix designed for the X–ray Microcalorimeter Spectrometer (XMS) of the ATHENA satellite. For the given cosmological parameters and redshift, the FoV of ATHENA ($2.4' \times 2.4'$) encloses a region of 497.52 kpc per side, and we center the field of view on the centre of the cluster, probing therefore the very central part of the clusters.

Velocity broadening

Given the high energy resolution provided by the XMS spectrometer, ATHENA spectra are very well resolved and emission lines can be studied in fine detail. In fact, we restrict the spectral analysis to the $5 - 6.5$ keV energy band, containing the iron Kα

complex around $6.7\,\mathrm{keV}$ (rest–frame energy), and fit with an absorbed $\texttt{BAPEC}$[5] model (see Fig. 5.1 for an example with one of the presented haloes), a velocity– and thermally–broadened emission spectrum for collisionally–ionised diffuse gas. The model assumes the distribution of the gas non–thermal velocity along the l.o.s. to be Gaussian and the velocity broadening is quantified by the standard deviation, σ, of this distribution.

5.4   Results

5.4.1   Velocity statistics

Our first goal is to investigate the properties of the ICM velocity field in the simulated data directly, in order to establish the level of reliability of the mock data results. Gas particles in the simulated haloes have been selected to reside within R_{500} in the xy plane, excluding the low–temperature ($T_{gas} < 3 \times 10^4$ K)[6] and star forming (gas particles with $> 10\%$ of cold fraction) phase of the gas. This selection is done to resemble in the most faithful way possible the X–ray emitting gas residing in the region observed with the X–ray virtual telescope PHOX. In the following, we will always refer to regions in the xy plane, considering the cylinder–like volume along the line of sight, aligned with the z–axis of the simulated box.

By definition, we calculate the weighted value of the standard deviation of the gas velocities along the l.o.s., σ_w as

$$\sigma_w = \frac{\Sigma_i w_i (v_i - \overline{v}_w)^2}{\Sigma_i w_i}, \tag{5.1}$$

where w represents the quantity used to weight the velocity (e.g. the mass or the emission measure, EM, of the gas particle), v_i is the l.o.s. component of the velocity for each particle and $\overline{v}_w$ is the weighted mean value of the l.o.s. velocity.

From Fig. 5.2, the relation between the value of $\sigma_{500,m}$ (i.e. weighted by the particle mass), and M_{500} shows that, in general, more significant motions of the gas are indeed expected in more massive systems. Ideally, the mass–weighted value should trace in the most faithful way the intrinsic velocity field of the cluster, since it is expected to be determined mainly by the potential well of the halo. However, X–ray observations of the ICM are more likely sensitive to the emission measure (EM) of the emitting gas and rather

---

[5] See http://heasarc.nasa.gov/xanadu/xspec/manual/XSmodelBapec.html.
[6] The gas component with $kT < 2\,\mathrm{keV}$ is further excluded from the calculation of velocity dispersions, since the detectable signature from iron line broadening is mainly due to the hot gas phase.

provide estimates for an EM–weighted–like velocity dispersion. We therefore investigate the relation between mass–weighted and EM–weighted velocity dispersion, $\sigma_{500,m}$ and $\sigma_{500,EM}$ respectively.

The comparison is shown in Fig. 5.3, wherein both values of $\sigma_{500,w}$ are calculated for the gas residing within R_{500}, in the plane perpendicular to the l.o.s.. The relation found between the two definitions of $\sigma_{500,w}$ is not coincident with the one–to–one relation (overplotted in red in the figure), as the EM–weighted value is likely to be affected by the thermo–dynamical status of the gas[7], that is by processes such as turbulence, merging and substructures. Despite this, the difference is quite small and the two values are fairly well correlated.

For the purpose of our following analysis and the comparison against synthetic X–ray data, however, we decide to use the EM–weighted velocity dispersion, $\sigma_{500,EM}$, which is more directly related to the X–ray emission of the gas, because of the proportionality between the normalization of the X–ray spectrum and the gas EM itself.

In order to probe the global, dynamical structure of the ICM we would need to observationally measure the gas velocity dispersion within the whole R_{500} region. However, simulating observations for a telescope like ATHENA we would be able to infer information only about a smaller, inner region. Therefore, we explore the relation between the estimated value of the velocity broadening along the line of sight in different regions of the cluster, shown in Fig. 5.4. It is evident from the figure that the value calculated for the gas within R_{500} correlates linearly with the value computed in smaller, internal regions, namely for $r < 0.3R_{500}$ (upper panel) and for the region covered by the FoV of ATHENA, $\sim 0.15R_{500}$ (lower panel).

With respect to the one–to–one correlation (red line in Fig. 5.4), however, outliers are present in this sample, showing that prominent substructures in the velocity field of the gas must be present in these clusters. Therefore, the level of complexity in the spatial structure of the ICM velocity field can be singled out by such comparison between the velocity dispersion calculated in the R_{500} region and the values corresponding to smaller, inner regions.

Nevertheless, the relations discussed ensure that we can safely:

---

[7]We recall here that EM $= \int n_e n_H dV$.
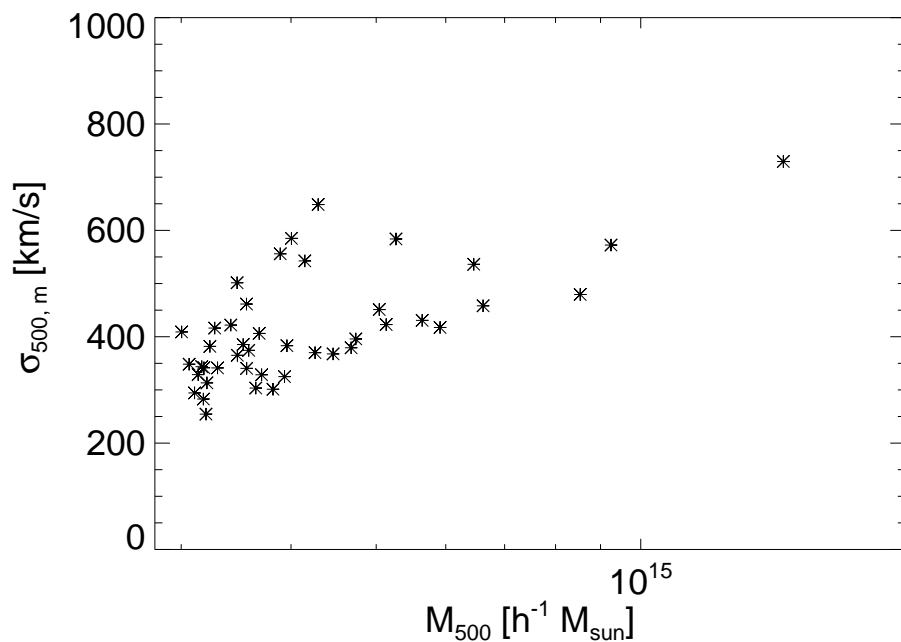
Figure 5.2: Theoretical value of the mass–weighted velocity dispersion, σ_m, calculated within R_{500} (in the plane perpendicular to the l.o.s. direction), reported as function of the halo mass M_{500}, in $h^{-1}\,\mathrm{M_\odot}$.
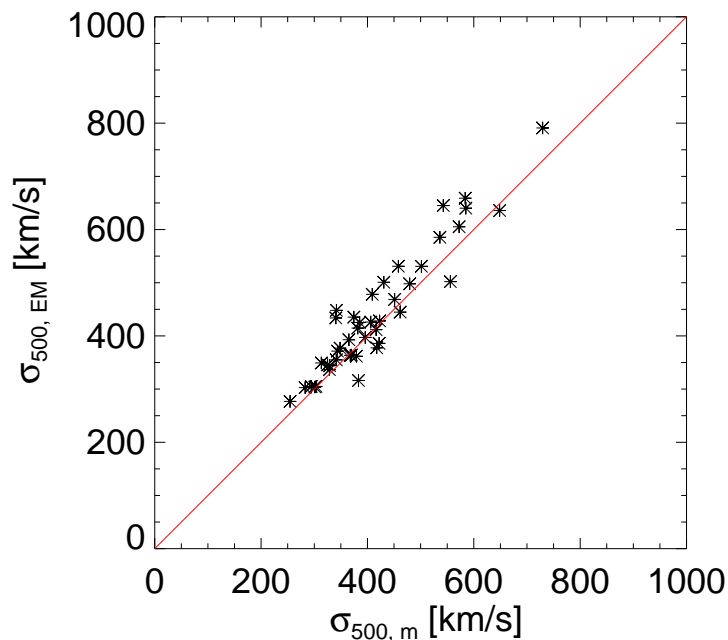
Figure 5.3: Theoretical value of the EM–weighted velocity dispersion, $\sigma_{500,EM}$ versus the mass–weighted value, $\sigma_{500,m}$, in km/s. Both values are calculated for the region within R_{500}, in the plane perpendicular to the l.o.s. direction. Overplotted in red is the curve referring to the one–to–one relation.
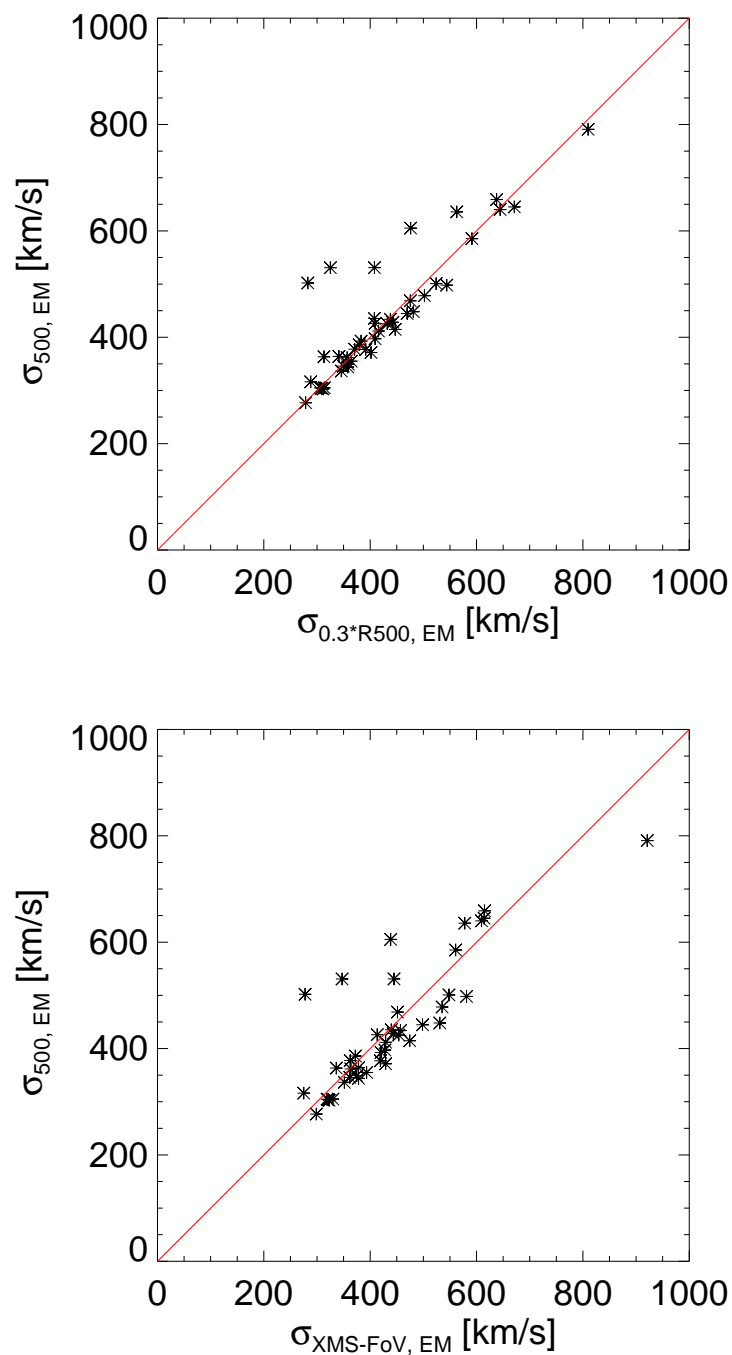
Figure 5.4: Relation between the EM–weighted velocity dispersion, $\sigma_{500,EM}$, within R_{500} and the analogous values calculated for: (top panel) the region within $0.3R_{500}$ and (bottom panel) the region covered by the FoV of ATHENA, (i.e. $\sim 0.15R_{500}$). Overplotted in red is the curve referring to the one–to–one relation.

(i) assume the EM–weighted velocity dispersion instead of the mass–weighted value to trace the intrinsic velocity structure;

(ii) focus on the expected value for the whole R_{500} region of the cluster, even though the velocity dispersion detectable with ATHENA probes a smaller, inner region, given by the XMS FoV.

5.4.2   Comparison against synthetic data

The ICM velocity dispersion calculated directly from the simulation can here be used to compare against the mock ATHENA data, from which we can use the high–resolution spectroscopy to measure the velocity dispersion of the gas along the line of sight. Fig. 5.5 shows the comparison between expectations provided by the simulated data (black diamonds) and results from analysis of the synthetic ATHENA spectra (blue asterisks).

The expected velocity dispersion of the gas particles residing in the region corresponding to the ATHENA FoV is calculated according to Eq. 5.1, weighted by

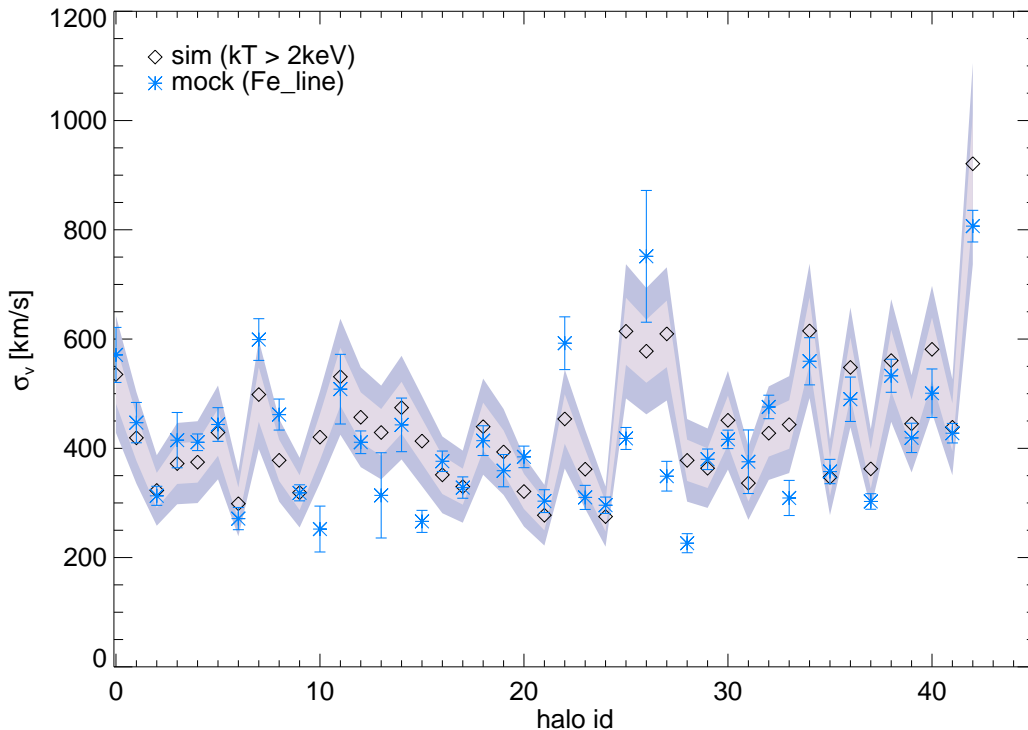Figure 5.5: Comparison between the theoretical expectation of the velocity dispersion σ_v, calculated directly from the simulation (black diamonds and shaded areas), and the value obtained from the spectral fitting of the synthetic XMS spectra obtained with PHOX (blue asterisks with error bars). The id numbers of the 43 haloes in the sample (x–axis) are ordered according to the increasing halo mass, M_{500}.

the EM, while the values derived from the X–ray spectra are obtained as described in Section 5.3.3, with error bars corresponding to the 1σ errors to the best–fit values. As shown in the Figure, we find very good agreement between simulation (intrinsic, "true" solution) and synthetic spectral data (observational detections), namely for $\sim 74\%$ of the haloes the spectral analysis of the iron lines provides a measure of the gas velocity dispersion, along the l.o.s., within 20% from the expected value (purple, shaded area). We find, in particular, that $\sim 50\%$ of the halos show agreement at a level better than $\sim 10\%$ (internal, pink shaded area in Fig. 5.5). We remark here that the reference number, or halo id in the Figure, is associated to the haloes of the sample in an increasing order for increasing M_{500}.

The deviation between expected and measured velocity dispersion, referring to the XMS FoV as in Fig. 5.5, has been quantified as

$$\delta = \frac{\sigma_v^{mock} - \sigma_v^{sim}}{\sigma_v^{sim}}, \tag{5.2}$$

and its distribution for the sample is reported in Fig. 5.6.

Clearly, the distribution of δ is peaked around the zero value, reflecting the very good
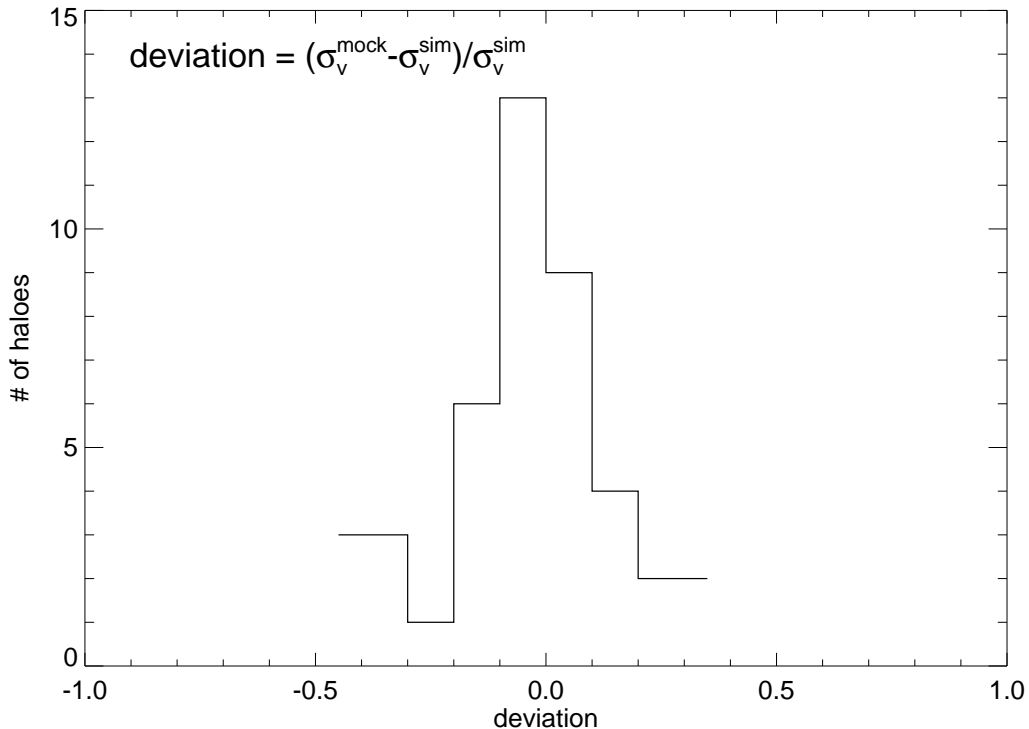

Figure 5.6: Deviation of the best-fit σ_v from the expected value for all the 43 haloes in the sample.

agreement previously discussed. However, we also find outliers in the sample that show deviations up to $\sim 43\%$.

Extreme cases in the sample

Given the distribution of the deviations, reported in Fig. 5.6, we here focus onto two sets of haloes in the sample for which the deviation between simulation and mock data is very minor and most prominent, respectively.
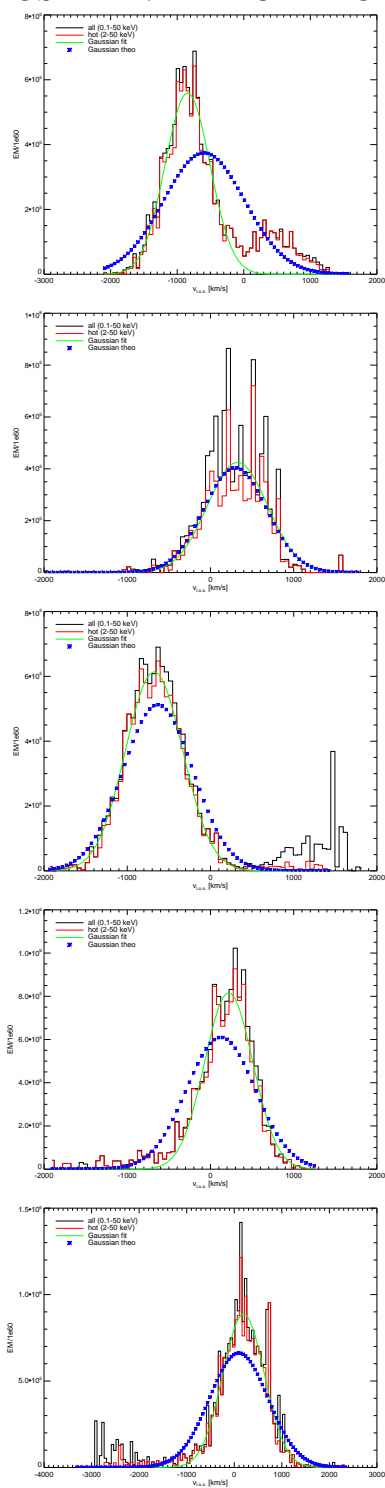
The EM distribution as function of the l.o.s. velocity, for the gas particles in the ATHENA FoV, is shown for the two sets of haloes in Fig. 5.7. The black histograms refer to all the gas in the region, while the overplotted red histograms only account for the hot–phase gas, i.e. particles for which $kT > 2\,\mathrm{keV}$. The reason for selecting the hot gas is that it mostly contributes to the iron line emission, from which the velocity broadening is measured.

It is clear from the left–hand–side column in the Figure, corresponding to the most–deviating haloes, that there are substantial substructures within the gas velocity field. The red histograms for the haloes that show best agreement (right–hand–side column), instead, reflect more regular distributions of the EM as function of the $v_{l.o.s.}$, indicating more regular velocity fields.

The value estimated from the broadening of the spectral lines is assumed to be the dispersion of the Gaussian distribution that best fits the line shape. Therefore, a more detailed comparison should involve the dispersion of the Gaussian function matching the (red) distribution shown, instead of the theoretical value calculated as in Eq. 5.1. The green curves in Fig. 5.7 define the Gaussian fits to the red distributions, whose σ_v^{gauss} is more directly comparable to the spectral results.

As an additional comparison, we also overplot the Gaussian curve (blue asterisks) constructed from the theoretical estimation of the EM–weighted values for gas velocity dispersion (Eq. 5.1) and mean l.o.s. velocity. In the most–deviating clusters, the evident differences among the different curves substantially reflects the deviations explored above (see, e.g., the halo with the largest deviation, top–left panel in Fig. 5.7). In particular, the green, best–fit Gaussian clearly fails to capture all the features of the multi–component velocity distribution, which is most likely what happens during the spectral fit. The low level of deviation found for the "best" haloes set (right–hand–side column) is indeed

5 MOST–DEVIATING HALOES   5 LEAST–DEVIATING HALOES
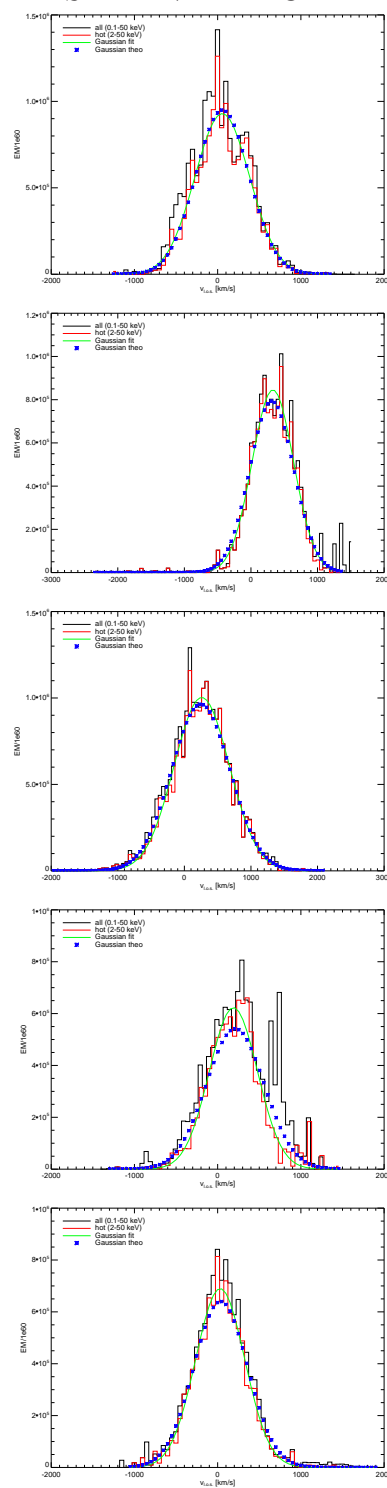
Figure 5.7: Distribution of EM as function of gas l.o.s. velocity, for the five most–deviating and least–deviating (best) haloes according to Fig. 5.6. Black: all the gas particles; red: hot–phase gas ($kT > 2\,$keV); green: Gaussian best–fit to the hot–gas (red) distribution; blue asterisks: theoretical Gaussian distribution reconstructed from the estimated dispersion of the hot–gas (red) distribution.

5 MOST–DEVIATING HALOES
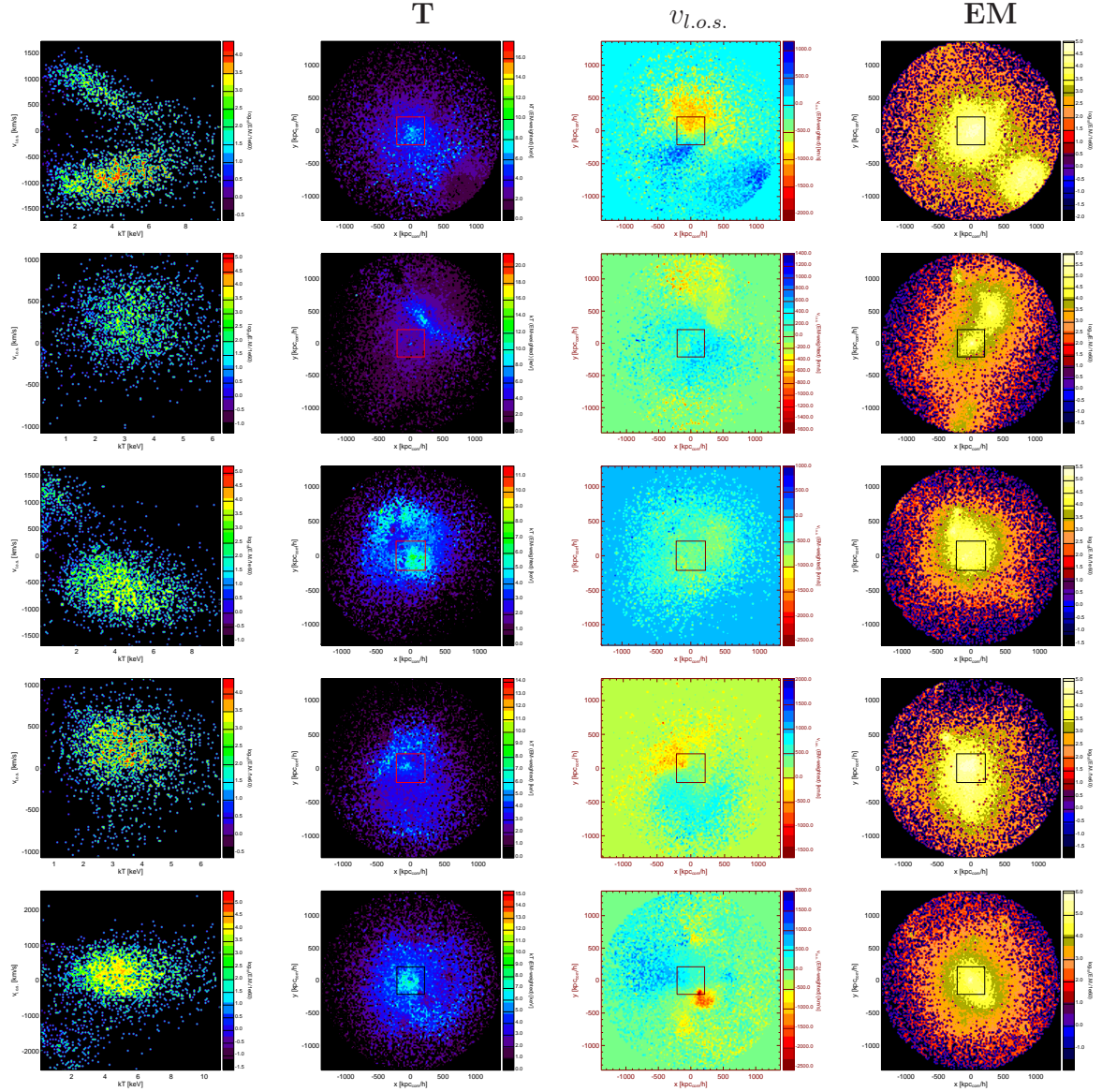
Figure 5.8: Maps of the ICM thermo–dynamical status for the five most-significant outliers with respect to the velocity–broadening diagnostics. Columns, from left to right: (1) $v_{l.o.s.} - kT$ map, color–coded by EM (considering gas particles within ATHENA FoV); (2) EM–weighted, temperature map, projected along the l.o.s.; (3) EM–weighted, l.o.s.–velocity map projected onto the xy plan (i.e. along the l.o.s.); (4) EM map projected along the l.o.s.. Spatial maps in columns (2)-(3)-(4) refer to the whole R_{500} region and, overplotted, is the ATHENA FoV for comparison. From top to bottom the haloes are ordered such that the level of *deviation* from the expected σ_v is *decreasing*.

shown by the good match between best–fit (green curve) and theoretical (blue asterisks) Gaussian overplotted to the EM–$v_{l.o.s.}$ distributions.

A visualization of the thermo–dynamical structure of these clusters is shown in Fig. 5.8

5 LEAST–DEVIATING HALOES
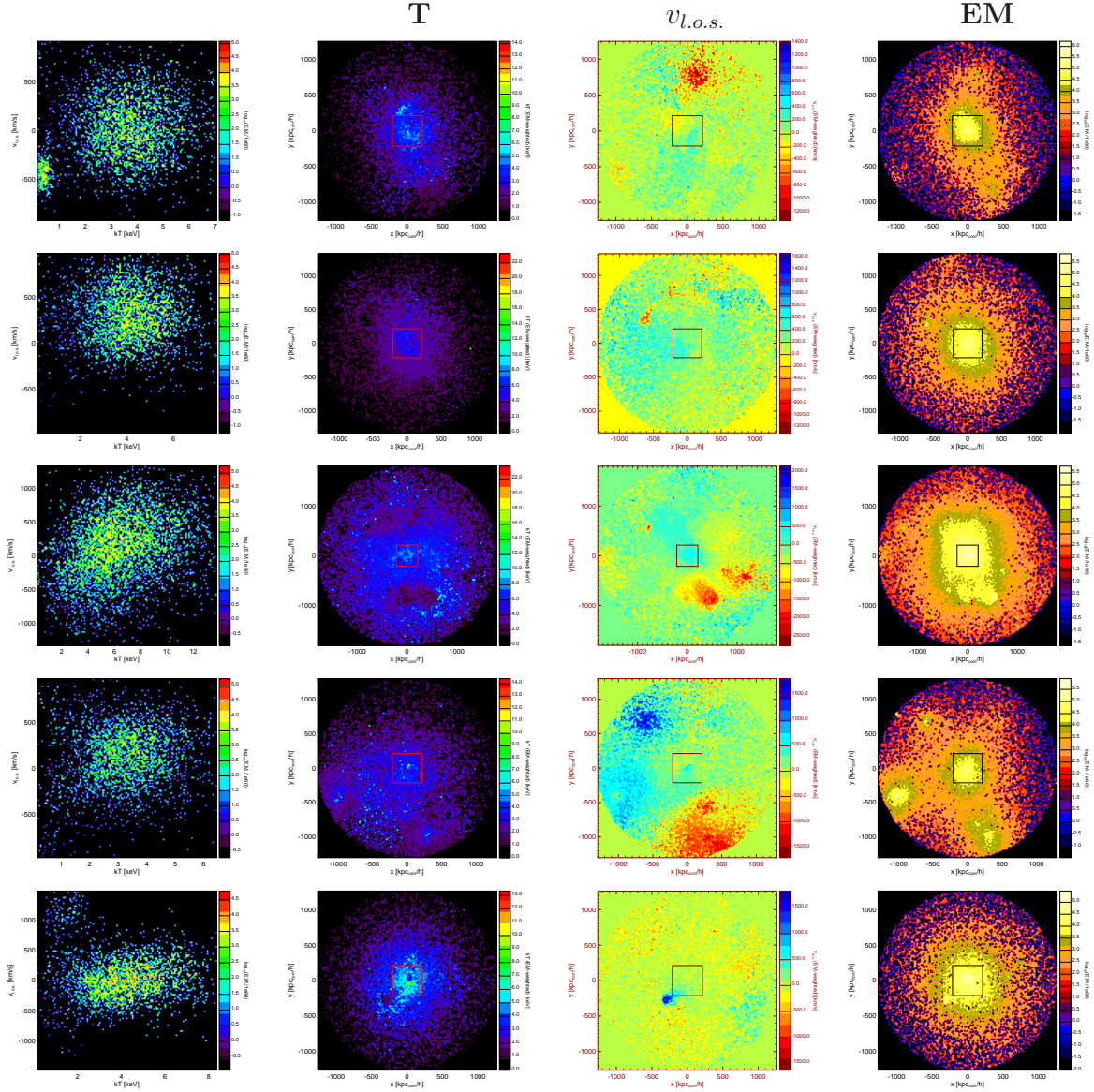
Figure 5.9: Same as Fig. 5.8, but for the five best cases: from top to bottom the haloes are ordered such that the level of *agreement* between best–fit and expected σ_v is *decreasing*.

and Fig. 5.9, for the set of most–deviating and best haloes, respectively. The rows in the two figures correspond to the same row in Fig. 5.7, where the level of deviation, or agreement, decreases from top to bottom. In the first column, we show the $v_{l.o.s.} - kT$ map of the gas residing within the ATHENA FoV, color–coded by EM. Especially for the most deviating haloes, the sub–structures in the velocity field unveiled by Fig. 5.7 are clearly visible, combined with the gas thermal structure. The other columns show the

spatial distribution of temperature, l.o.s. velocity and EM, for the gas contained within R_{500}, projected onto the plane perpendicular to the l.o.s. direction. Overplotted in black, we also show the $2.4' \times 2.4'$ FoV of the ATHENA XMS.

Despite the deviations discussed, an overall good agreement is found between the intrinsic amplitude of the gas velocity dispersion and the velocity broadening measured directly from mock spectra. Moreover, given that the analysis of the simulations suggests the velocity structure of the gas in the innermost region (e.g. that covered by the FoV of ATHENA) to be closely traced by that within R_{500} (Section 5.4.1), we will use the latter for our further investigation.

5.4.3 $L_X - T$ scaling relation

We investigate the impact of the ICM velocity structure on X–ray properties by focusing on the $L_X - T$ relation. The main motivation behind this choice is that, on one hand, the luminosity, L_X, is very well measured in X–ray surveys (e.g. with Chandra, XMM–Newton, or the up–coming eRostita), and, on the other hand, the temperature T provides a good mass proxy, since it is tightly related to the total gravitating mass, which is the most fundamental quantity to characterise a cluster.

L_X, also denoted as "bolometric X–ray luminosity ", is usually the X–ray luminosity extrapolated to the whole X–ray band, $0.1 - 100$ keV, instead of being calculated in a narrow energy band. Although, in our case, the computation of the luminosity is limited to the largest energy band defined by the ACIS–I3 response matrix (i.e. $0.26 - 12$ keV), the difference introduced with respect to the expected bolometric X–ray luminosity is found to be minor.

In Fig. 5.10 we show the $L_X - T$ relation calculated for the simulated haloes (asterisks), from the Chandra synthetic observations of the R_{500} regions, obtained with PHOX. As a comparison, we also show the data presented in Pratt et al. (2009) for a sample of 31 nearby galaxy clusters (black diamonds), selected only in X–ray luminosity from the Representative XMM–Newton Cluster Structure Survey (REXCESS).

Fitting procedure

The $L_X - T$ relation was fitted with a power–law functional form, that is

$$h^{-1}(z)L_X = C\,(T/T_0)^{\alpha},\tag{5.3}$$

Figure 5.10: $L - T$ scaling relation from Chandra mock spectra (green asterisks), for the region of the clusters encompassing R_{500}. Overplotted are the results from Pratt et al. (2009) (P09) (black diamonds). Best–fit relations are also overplotted (solid lines for P09; dotted lines for simulated haloes of the present work) and correspond to the two linear regression fitting methods adopted: BCES (L|T) (red) and BCES Orthogonal (blue).

where L_X is given in units of 10^{44} erg/s, $T_0 = 5$ keV and the assumed cosmology is accounted for in $h^2(z) = \Omega_0(1 + z)^3 + \Omega_\Lambda$. The fit was performed using linear regression in the log–log plane.

As done in Pratt et al. (2009), as well as in several similar works (e.g. Reiprich and Böhringer, 2002; Arnaud et al., 2005; Mittal et al., 2011), we adopted the BCES (Bivariate Correlated Errors and intrinsic Scatter) regression method by Akritas and Bershady (1996), which accounts for both the errors in L_X and in T, as well as the intrinsic scatter in the data. The BCES algorithm allowed us to calculate the best–fit values of slope (α) and normalization (C) for four different regression methods, amongst which we restrict our attention to the BCES (L|T) and the BCES Orthogonal methods. Our primary goal is to find the best fit which minimizes the residuals of both variables at the same time, orthogonally to the linear relation. This is given by the BCES Orthogonal

method. Additionally, we also explore the results given by the BCES (L|T) fitting method (analogously to Pratt et al. (2009)), which minimises the residuals in L_X. Reasons for this rely on the fact that L_X can be treated as the dependent variable, while the temperature can be assumed to be closely related to the cluster mass, which is the most fundamental quantity characterizing the system.

Given the statistical uncertainties[8] on both variables, σ_{Y_i} and σ_{X_i}, the raw scatter was estimated using the orthogonal distances to the regression line, weighted by the errors. Namely, for a linear relation of the form $Y_i = \alpha X_i + \beta$ in the log–log space, the raw scatter is

$$\sigma_{raw}^2 = \frac{N/(N-2)}{\Sigma_{i=1}^N 1/\sigma_i^2} \sum_{i=1}^N (1/\sigma_i^2)(Y_i - (\alpha X_i + \beta))^2 \tag{5.4}$$

where N is the number of data points in the sample, $Y_i = \log(L_{X,i})$, $Y_i = \log(T_i)$, $\beta = \log C$, and

$$\sigma_i^2 = \sigma_{X_i}^2 + \alpha^2 \sigma_{Y_i}^2. \tag{5.5}$$

The intrinsic scatter was estimated from the difference between the raw and the statistical scatter, in quadrature ($\sigma_{raw}^2 = \sigma_{stat}^2 + \sigma_{intrinsic}^2$).

Best–fit relations are overplotted in Fig. 5.10 for both observational data (solid red and blue lines, for the BCES (L|T) and the BCES Orthogonal method respectively, from Pratt et al., 2009) and for Chandra synthetic observations of the simulated sample (dotted lines). The linear relations found for the simulated clusters are overall shallower than the observed ones, and, among the two fitting methods considered, the BCES (L|T) method still provides a shallower slope than the BCES Orthogonal case. We note, however, that our cluster sample probes a smaller dynamical range with respect to observations and, in particular, lacks low–temperature haloes, whose presence might be important to provide tighter constraints on the slope of the relation.

The implications due to velocity structure

In Fig. 5.11 we include an additional parameter to further characterize the cluster state. In particular we show the $L_X - T$ relation for the simulated haloes, as in Fig. 5.10, color–coding the data points according to the increasing ratio of

$$\mu = \sigma_v / \sigma_{thermal}, \tag{5.6}$$

---

[8]In the log space, errors are transformed as $\Delta \log x = \log e \times (\Delta x)/(2x)$, where Δx is the difference between the upper and lower boundary of the error range around the quantity.
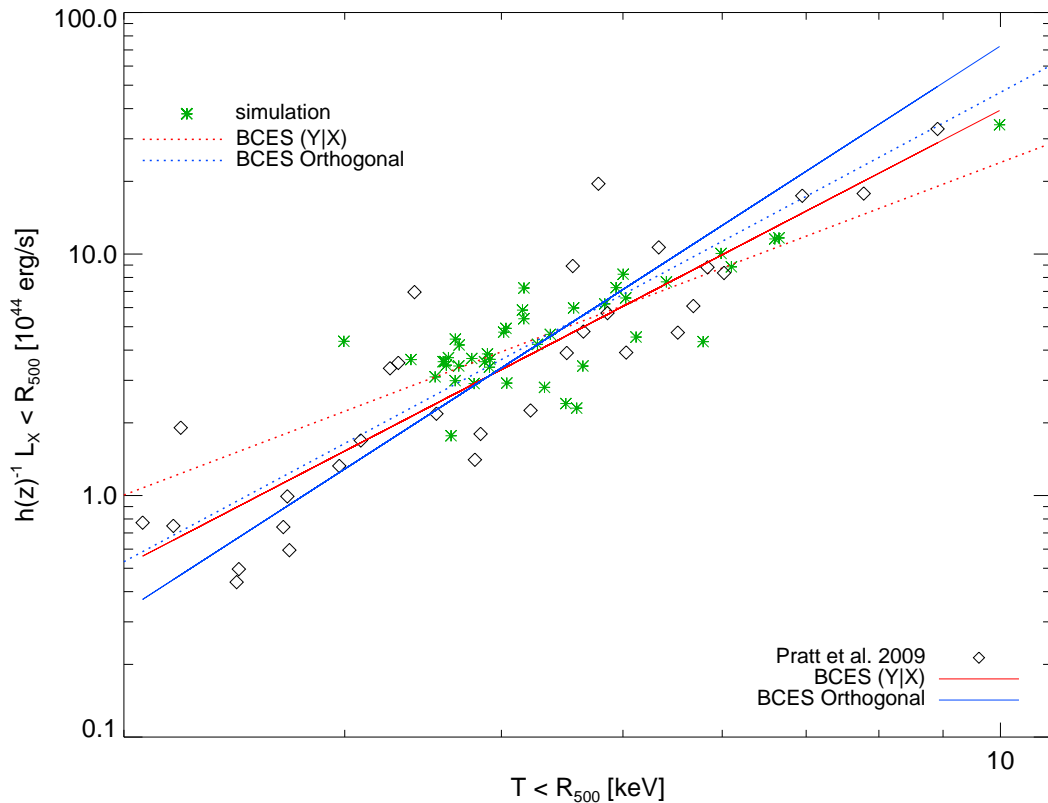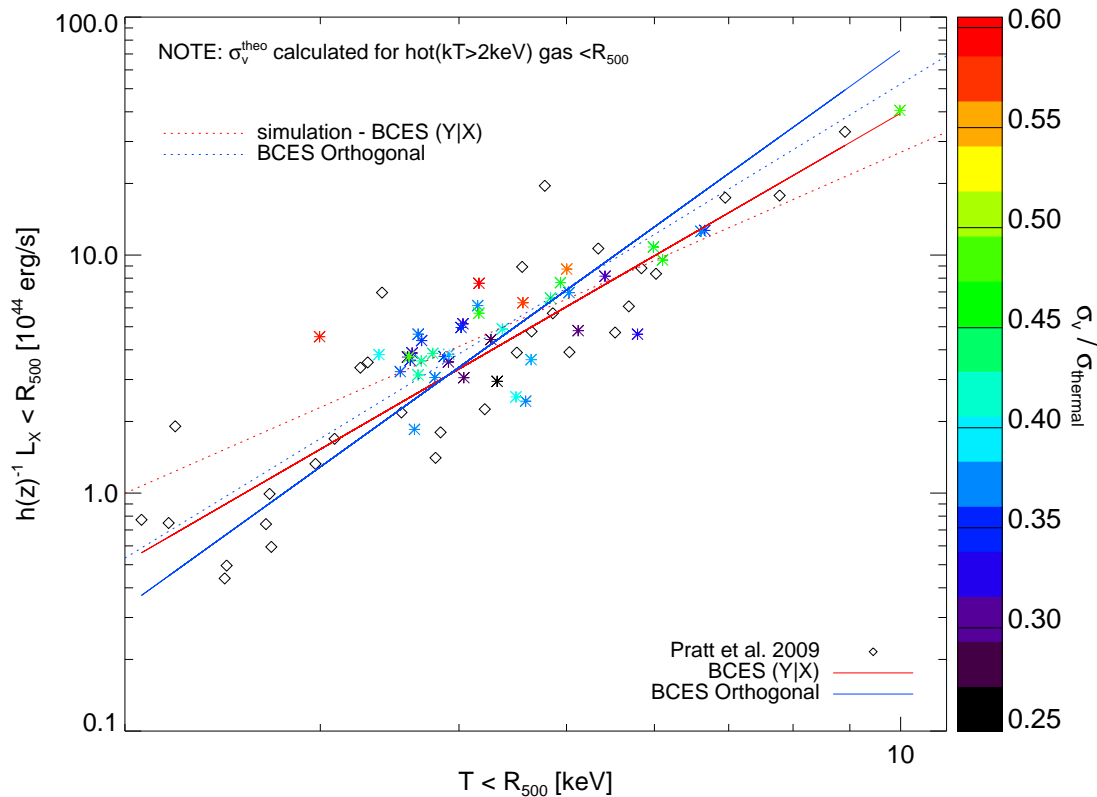
Figure 5.11: $L-T$ scaling relation from Chandra mock spectra, for the region of the clusters encompassing R_{500}. Observational data from Pratt et al. (2009) and best–fit relations for both observations and simulated haloes are reported as in Fig. 5.10. Color code: value of $\sigma_v/\sigma_{thermal}$, calculated from gas velocities in the region encompassed by R_{500}.

calculated for the region encompassed by R_{500}.

The velocity dispersion σ_v corresponds to the EM–weighted value calculated directly from the gas particles in the simulation (see Section 5.4.1). The thermal velocity dispersion, $\sigma_{thermal}$, is the expected value for the ICM temperature T, reported in the x–axis of the relation. Small values of μ indicate a low level of non–thermal velocity with respect to the characteristic thermal velocity dispersion of the gas. For the extreme case of $\mu \sim 1$, the non–thermal velocity dispersion would equal the thermal value.

In order to quantify the effects of l.o.s. velocity structure on the resulting scaling relation, we investigated the dependences of best–fit slope, normalization and scatter on the value of μ (see Eq. 5.6).

The distribution of μ for the 43 simulated clusters is shown in Fig. 5.12 (top–left panel, upper in–set). A significant number of haloes ($\sim 35\%$) are characterised by a
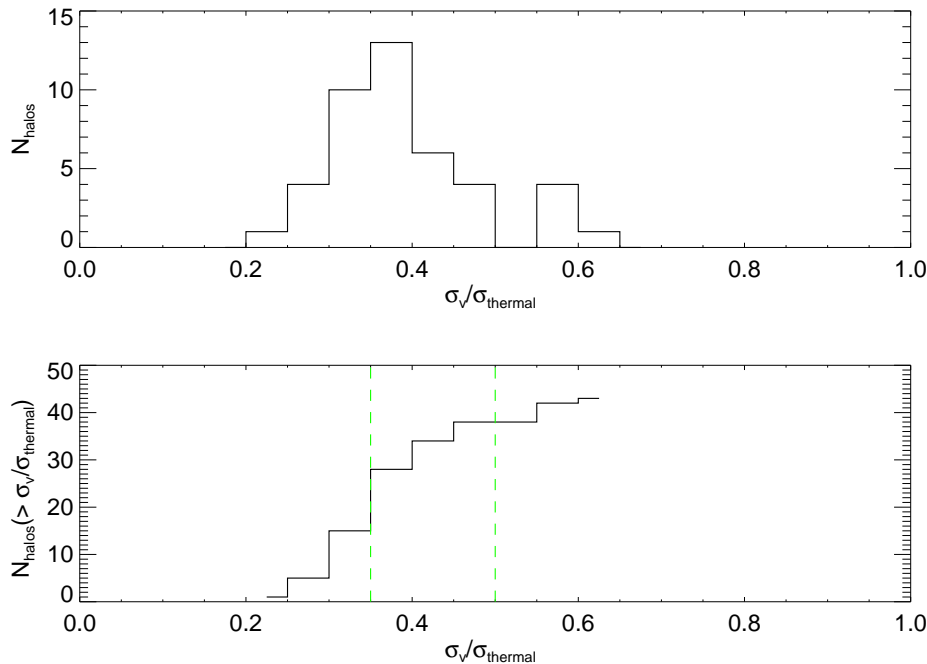
Figure 5.12: Distribution (upper in–set) and cumulative distribution (lower in–set) of $\mu = \sigma_v(< R_{500})/\sigma_{thermal}$, for the sample of 43 simulated clusters. Green, dashed lines correspond to the values $\mu_{max} = 0.5, 0.35$ used to identify the two sub–samples.

gas velocity dispersion which is larger than $0.4\sigma_{thermal}$.   In particular, by examining the cumulative distribution of μ within the sample (Fig. 5.12, lower panel), we decide to extract two additional sub–samples from the 43 haloes, selected to have a maximum of $\mu_{max} = 0.5, 0.35$, respectively. The first sub–sample is intended to exclude the most prominent outliers in the μ distribution, for which the velocity dispersion σ_v exceeds 50% of $\sigma_{thermal}$. The smaller sub–sample contains the haloes with the smallest fraction of μ, indicating that their expected thermal velocity is dominant with respect to σ_v. We then fit the $L_X - T$ relation for the original sample and for the two sub–samples. Results are shown in Fig. 5.13, where we report both the BCES (L|T) (red squares) and the BCES Orthogonal (blue squares) values.

For all the quantities studied, the best–fit values generally increase with the increasing amplitude of velocity dispersion, relative to the characteristic thermal value.   This has significant implications for the intrinsic scatter (calculated here for the luminosity, $\sigma_{\ln L,intrinsic}$[9]). In fact, the trend found reflects how the scatter in luminosity of the $L_X - T$

---

[9]We report the final value by considering the natural logarithm, ln, for comparisons to Pratt et al. (2009), although the equations and the logarithm space mentioned in the paper usually refer to $\log = \log_{10}$

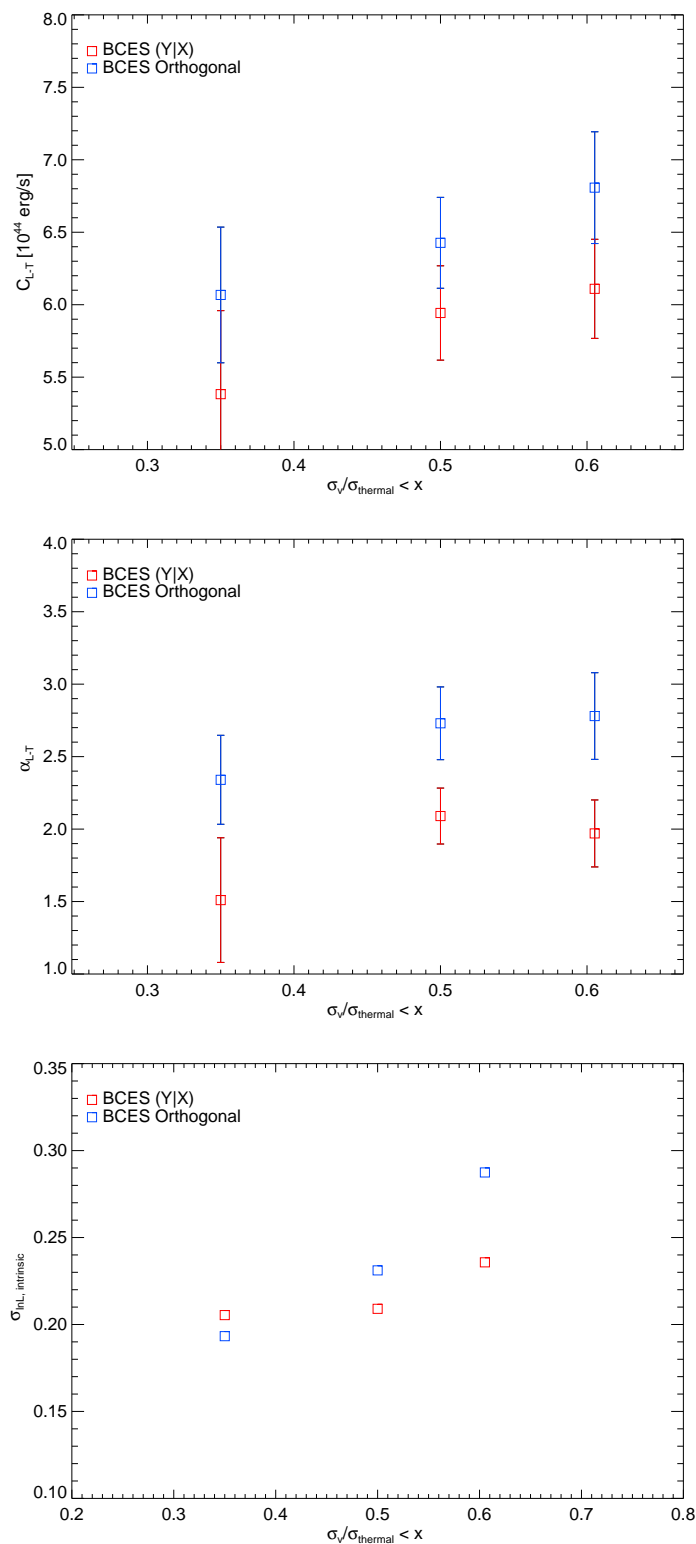Figure 5.13: Dependence of normalization (C, top), slope (α, middle) and intrinsic scatter ($\sigma_{\ln L, intrinsic}$, bottom) of the $L-T$ relation on the maximum μ used to select the corresponding sub–sample of clusters.

scaling relation is sensitive to the baryonic physics and can be closely related to complex or disturbed configurations of the ICM velocity field, which are quantified by large values of μ. Essentially, *the introduction of clusters with significant non–thermal velocity dispersion, with respect to their typical thermal velocity, augments the scatter in the sample about the best–fit $L_X - T$ relation.*

5.5   Discussion and conclusions

In this paper we have presented the study of the ICM velocity structure and its impact on the $L_X - T$ scaling relation, from hydrodynamical simulations and synthetic X–ray observations of a set of galaxy clusters. Numerical simulations have been performed by means of the treePM/SPH, parallel code P–GADGET3, including a number of physical processes describing the baryonic component in the simulation with a level of detail never reached so far. The set of 43 simulated cluster–like haloes has been selected from a medium–resolution cosmological box by requiring $M_{500} > 3 \times 10^{14} h^{-1} \, \mathrm{M}_\odot$. The mock X–ray observations have been obtained with the virtual photon simulator PHOX (Biffi et al., 2012) for both Chandra ACIS–I3 and the XMS high–resolution spectrometer designed to be on board ATHENA.

From the direct analysis of the gas component in the central part of the simulated haloes, in the projection plane perpendicular to the chosen line of sight, we find tight relations among different definitions and selection criteria used to calculate the gas velocity dispersion. In order to consistently compare and use results from simulations and mock observations, we always referred to cylinder–like regions which extend throughout the z coordinate of the simulated box, i.e. along the l.o.s. direction. In particular, we find that mass– and emission–measure–weighted velocity dispersion calculated for the gas particles with R_{500} both correlate closely to the halo M_{500} and, therefore, can be equivalently employed to trace the halo mass. Between the two definitions, we concentrate on the EM-weighted velocity dispersion since it is more sensitively related to the gas X–ray emission.

We also find that $\sigma_{500,EM}$ probes fairly well the velocity dispersion in inner, smaller regions of the clusters, such as the region covered by the FoV of ATHENA. As a fair approximation, we can safely assume the results to be representative of the whole region out to R_{500}, even though single–pointing ATHENA observations of clusters at

the considered redshift would only cover their innermost part. On the other hand, small–scale spatial features of the ICM velocity field could be possibly unveiled by the detailed comparison between the large–scale amplitude of the l.o.s. velocity dispersion and the value detectable with ATHENA observations. By applying our virtual telescope, PHOX, to the simulated haloes, the l.o.s. velocity dispersion is derived from the velocity broadening of the Kα iron complex around 6.7 keV in the synthetic X–ray spectra, provided the high energy resolution expected to be reached by the XMS spectrometer.

Within the FoV of the ATHENA XMS, moreover, predictions on σ_v provided by the simulation and detections mimicked with PHOX show a level of deviation of less than 20%, for 74% of the clusters in the sample. The largest deviations of observed velocities from expected values are significantly dependent on the complicated distribution of the gas velocities (see Fig. 5.7). In principle, a more detailed modelling of the shape of the spectral emission lines, such as the iron complex used here, rather than the standard Gaussian fit, should allow us to derive more accurate measures of the l.o.s. velocity dispersion of the gas, accounting for multiple components in the velocity field.

For the scope of our investigation, the good agreement between mock data and simulation further suggests the possibility to utilise the $\sigma_{500,EM}$ obtained directly from the simulation to constrain the impact of velocity structure onto X–ray observables, such as luminosity and temperature. In principle, this also suggests that as soon as high–precision X–ray spectroscopy will become available, for instance with the up–coming ATHENA mission, we will be able to safely employ the detected values of the ICM non–thermal velocity dispersion for studies of real galaxy clusters as well.

From the synthetic Chandra spectra obtained with PHOX, we were able to estimate observed bolometric luminosity, extrapolated to the entire X–ray band, and cluster temperature, for the ICM residing within R_{500}. The $L_X - T$ scaling relation constructed from these mock data generally agree with real observations, e.g. from Pratt et al. (2009). By using the BCES linear regression fitting method (Akritas and Bershady, 1996), we assume a linear relation between L_X and T in the log–log space and determine the best–fit slope and normalization of the $L_X - T$ for our 43 simulated clusters, finding a shallower slope with respect to the results reported in Pratt et al. (2009). In the fitting procedure, we explore both the BCES (L|T) and BCES Orthogonal methods, where the former treats the luminosity as dependent variable and minimizes its residuals, while the latter implies

both variables, L and T, as independent variables and minimizes the orthogonal distances to the linear relation.

As a step forwards, we include the information obtained about the ICM velocity dispersion along the l.o.s. in order to investigate the effects on slope, normalization and intrinsic scatter of the best–fit $L_X - T$ relation.

Interestingly, the exclusion from the original sample of the haloes with largest velocity dispersion (normalized to the characteristic thermal value associated to their temperature) allows us to reduce significantly the scatter in the $L_X - T$ relation, as clearly shown by the trend in Fig. 5.13 (right–hand–side panel). The increasing trend of slope and scatter, in particular, suggests a dependence on the contamination of the sample by haloes which show significant fraction of non–thermal velocity, although the results would need a larger statistics to be more strongly confirmed, especially at the low–temperature end of the relation, which is not probed by our sample.

As a promising, future perspective, we expect high–precision X–ray spectroscopy to provide valuable information on the non–thermal velocity structure of the ICM in galaxy clusters along the line of sight, which can be safely assumed to trace the intrinsic gas motions of the cluster despite the effects due to projection and instrumental response. This will be certainly fundamental to correctly determine the total mass in clusters and characterise in more detail the deviation of real clusters from the hydrostatic equilibrium at the base of X–ray mass estimates as well as the divergence from the self–similarity of the haloes expected from theoretical models.

5.6   Appendix

5.6.1   Treatment of chemical abundances in PHOX

Dealing with galaxy clusters, the main emission components in the X–ray regime are constituted by bremsstrahlung continuum and emission lines from heavy elements.

Usually, simulations of the X–ray emission from hydrodynamically simulated clusters assume the average value of one third the solar metallicity, consistently to the average metallicity measured for real clusters. With respect to previous hydro–simulations, however, the run analysed here provides full information on the chemical enrichment of the gas, tracing its composition with 10 elements, namely: He, C, Ca, O, N, Ne, Mg,

S, Si, Fe. An additional field for each gas particle accounts also for the total mass in all the remaining metals.

Therefore, the available abundances of the individual elements, He included, are read and used to calculate the contribution of each element to the final spectrum.

This is done, in PHOX, via the external package XSPEC, assuming a single–temperature VAPEC (or VMEKAL[10] Mewe et al., 1985; Kaastra and Mewe, 1993; Liedahl et al., 1995) model for each element, where the corresponding abundance is fixed at $1Z_{\odot}$. The total spectrum (S) of a gas particle, at its temperature T, will then be obtained as the sum of the continuum, due to H, plus the contribution of each element, weighted by its abundance in solar units (set, here, according to the values given by Anders and Grevesse (1989)). Explicitly:

$$S(T, Z_{tot}) = S(T, \mathrm{H}) + \Sigma_i Z_i \left[S(T, \mathrm{Z}_i) - S(T, \mathrm{H}) \right] \tag{5.7}$$

The abundances of the VAPEC (VMEKAL) elements which are not explicitly treated in the hydro–simulation are set to a fixed value, estimated from the remaining mass in metals associated to the particle.

---

[10]See http://heasarc.nasa.gov/xanadu/xspec/manual/XSmodelMekal.html.

Chapter 6

Final remarks

In this thesis I studied the velocity and thermal structure of the intra–cluster medium (ICM) in galaxy clusters, by means of hydrodynamical simulations and X–ray observable properties. In more detail, the goal of this investigation was to extract results from simulations of clusters in a form which is directly and faithfully comparable to real X–ray observations, with the future perspective of high–precision measurements of ICM velocity and temperature.

Numerical simulations uniquely provide direct insights on the full 3D structure of clusters, at any time during their formation history. This allows us to study the details of the ICM velocity field, not yet constrained by current X–ray observations. In Chapter 3, I studied in particular the establishment of rotational patterns in the ICM in the very central part of numerically simulated clusters, where the quiescent assembly of mass during the formation process is claimed to allow for such non–thermal, ordered motions. This is of extreme importance in the case of relaxed clusters, where only thermal motions of the gas are usually invoked to contribute to the pressure support. The phenomenon has been demonstrated to have an *intermittent nature*, both for two high–resolution re–simulations of isolated clusters, with different formation histories, and for a statistically significant sample of clusters. For clusters with a smooth accretion history I found that thermal motions indeed dominate, since the settling of rotational patterns in the core is definitely temporary and unstable, leading only to a minor contribution to the pressure support. By exploring the occurrence and destruction of these motions during the formation history, I found that even minor merging events, such as the passage of a gas–rich sub–halo close to the cluster core can substantially destroy any ordered pattern in the gas. However, major merging can drive rotation in the cluster gas and affect the total mass estimate

significantly (up to $\sim 20\%$).

In the case where significant rotational patterns, and non–thermal motions in general, are present, they should be taken into account in order to correctly measure the pressure and, consequently, accurately derive the total gravitating mass from X–ray properties of the ICM.

The concrete possibility to detect such velocities with observations is strictly related to the improvement of X–ray spectroscopy. In fact, X–ray spectra show the imprints of gas motions through the velocity broadening of emission lines coming from heavy elements in the ICM. Especially for these lines, such as the Fe K line complex around $6.7\,\mathrm{keV}$, this velocity broadening can be dominant with respect to thermal broadening, and a sufficiently high energy resolution can allow for direct measurement of the line of sight component of the gas non–thermal velocity. Precise measures of the centre shift of the emission line also permits to estimate the bulk motion of the gas. Instruments designed for up–coming X–ray missions, such as ASTRO–H and ATHENA (formerly, IXO), are expected to provide very good precision for this line diagnostics, reaching a spectral resolution of a few eV at $\sim 6\,\mathrm{keV}$.

Nonetheless, the interpretation of observational results and comparison against hydro–simulations of galaxy clusters is not straightforward. To this purpose, I developed and applied a novel tool to fully employ large and high–resolution hydro–simulations of galaxy clusters and obtain synthetic X–ray observations as similar as possible to real ones. The virtual X–ray photon simulator, PHOX, has been comprehensively described in Chapter 4, where I presented the new approach implemented in the code. The methodology adopted makes it extremely efficient to process large simulation outputs, maintaining high energy and spatial resolution and limiting the computational effort.

Taking advantage of the virtual X–ray telescope, I discussed the results from Suzaku mock observations of two simulated clusters residing in a filament–like region (see Chapter 4). The thermal structure of the two haloes has been shown to be different, with good precision, from the reconstruction based on X–ray analysis of the synthetic Suzaku spectra. Indeed, the multi–temperature fit of the synthetic spectra made it possible to recover the intrinsic emission measure distribution of the ICM as function of temperature, marking clearly the difference between the hot, multi–component cluster and the more regular, lower–temperature one. Through this application I was able to link

numerical and observational studies devoted to reconstruct the ICM thermal structure, via its emission measure distribution. The direct comparison to the ICM of simulated clusters has been used to probe the validity of the spectroscopic constraints on the emission measure distribution, which has been successfully reconstructed via a multi–temperature fit of the synthetic X–ray spectra. Here, the multi–component thermal structure has been treated as the sum of five fixed–temperature phases of the gas, but more sophisticated models for the theoretical shape of the EM distribution can be in principle adopted to fit the data, as in the SPEX package developed by Kaastra and collaborators to perform high–level X–ray spectroscopic analyses.

X–ray synthetic observations of numerically simulated clusters can also be used to anticipate the results of up–coming spectrometers, whose high energy resolution will allow for direct measurements of the ICM velocity field. Assuming the characteristic response of the ATHENA XMS spectrometer, I was able to obtain X–ray mock spectra of a sample of simulated clusters and constrain with standard observational analysis the non–thermal velocity amplitude along a chosen line of sight (see Chapter 5). I have shown the very good agreement between the velocity amplitudes estimated from the mock data and the true values computed directly from the simulations. This first of all ensures that such estimations can be very reliable to unveil the ICM non–thermal velocity, despite of projection and instrumental effects.

As the last issue addressed, I investigated the impact of ICM velocity structure onto the scaling law between X–ray bolometric luminosity and temperature, also derived from mock X–ray observations of the simulated clusters. The motivation for studying the $L_X - T$ relation is that the luminosity is very well measured by X–ray surveys and the temperature closely traces the total gravitating mass, which is the most important quantity characterising a cluster. Interestingly, the non–thermal velocity dispersion of the ICM has been found to correlate with the resulting functional form of the $L_X - T$ scaling law. In particular, the intrinsic scatter in the relation does depend on the maximum value of the non–thermal velocity in the cluster sample. By excluding the most turbulent clusters, having a non–thermal velocity component exceeding 50% of the characteristic thermal velocity, the scatter of the resulting $L_X - T$ scaling relation was reduced by a significant amount. This result suggests that the observed scaling relation can be biased by outliers in the sample, for which the non–thermal contribution to the pressure support

is prominent. The usual assumption of the gas motions to be completely thermal would be in these cases violated, and this can be a source of scatter in the expected self–similarity of the X–ray properties. Also, the velocity diagnostics can be employed as a method to classify clusters according to the dynamical state, which is independent of the usual morphological classification.

The picture unveiled by this thesis work shows that combining the predicting power of numerical hydro–simulations and the advances reachable in X–ray (spectroscopic) observations can indeed provide reliable constraints on the ICM intrinsic structure in galaxy clusters. The validity of observational methods used to extract such information can be tested directly by means of a virtual photon simulator, as the one presented here to this purpose, which can faithfully translate simulated data into observation–like results. This comparison benefits of the detailed information available in the case of simulations, which otherwise can not be gained in a direct way.

The possibility to mimic X–ray observations of galaxy clusters from hydrodynamical simulations allows us to reduce the gap between predictions from theoretical models and observational results. Ultimately, it will be possible to better define the projection and instrumental effects and single out the underlying physical processes, in order to correctly interpret the high quality X—ray data available with next–generation telescopes.

Part III

Appendices

Appendix A

Fundamental cosmological quantities

Here, let us specify some useful cosmological quantities and relations, which are conveniently utilised in our investigations.

A.0.2 The redshift

The *cosmological redshift* is definitely one of the most important quantity in cosmology, for that it is strictly related to the scale factor $a(t)$, but it can be more directly estimated from observational measurements.

Let us consider a luminous source that has no peculiar motion and is only moving with the expansion of the Universe and is located at a comoving coordinate with respect to the origin (i.e. the observer) r. The redshift associated to this source is defined as

$$z \equiv \frac{\lambda_o - \lambda_e}{\lambda_e}, \tag{A.1}$$

with λ_o and λ_e representing the wavelength of the radiation from the source observed and emitted, respectively. Since both source and observer are comoving with the Universe, the redshift z can be related directly to the scale factor. In fact, from the Friedmann–Lemaître–Robertson–Walker (FLRW) metric describing the geometry of the Universe, it can be easily derived (see, e.g., Coles and Lucchin, 1995; Peacock, 1999, for more details) that:

$$1 + z = \frac{a_0}{a}, \tag{A.2}$$

where, at the present time t_0, we set $a(t_0) \equiv a_0$ and $z \equiv 0$, by definition.

A.0.3 Cosmological distances

The distance, in cosmology, can be defined in several ways.

The **proper distance**, also obtainable from the FLRW metric, can be expressed as:

$$d_p = af(r) = \frac{ac}{H_0} \int_a^{a_0} \frac{\mathrm{d}a'}{a'^2 E(a')} = \frac{c}{(1+z)H_0} \int_0^z \frac{\mathrm{d}z'}{E(z')}, \tag{A.3}$$

given that

$$f(r) = \int_t^{t_0} \frac{c\mathrm{d}t'}{a(t')} = c \int_a^{a_0} \frac{\mathrm{d}a'}{a'^2 H(a')} = \frac{c}{a_0} \int_0^z \frac{\mathrm{d}z'}{H(z')}. \tag{A.4}$$

In both equations, we have made use of

$$H(z)^2 = H_0^2 \left[(1 - \Omega_{0,tot})(1+z)^2 + \Sigma\Omega_{0,w_i}(1+z)^{1-3w_i} \right] \equiv H_0^2 E^2(z)$$

(from the second Friedmann equation for the evolution of the Universe, see, e.g. Coles and Lucchin, 1995; Peacock, 1999), wherein we allow for various components of the cosmic fluid are considered, with equation–of–state $p = w_i\rho c^2$. H_0 is the value of the *Hubble constant* at $z = 0$, for which recent WMAP estimates provide $H_0 = 70.4 \pm 2.5\mathrm{km\,s^{-1}\,Mpc^{-1}}$ (Komatsu et al., 2011).

Also, the so–called **comoving distance** is frequently used in cosmological investigations and is basically defined as the proper distance at the present epoch:

$$d_{com} \equiv d_p(a_0) = a_0 f(r) = a_0 c \int_a^{a_0} \frac{\mathrm{d}a'}{a'^2 H(a')} = c \int_0^z \frac{\mathrm{d}z'}{H(z')}, \tag{A.5}$$

hence

$$d_p = \frac{d_{com}}{(1+z)}. \tag{A.6}$$

However, it is not possible to measure directly neither d_p nor d_{com} from observations and it is therefore convenient to define also the **angular–diameter distance**

$$d_{ang} \equiv \frac{D}{d\theta} = ar \tag{A.7}$$

and the **luminosity distance**

$$d_{lum} \equiv \left(\frac{L}{4\pi F} \right)^{1/2}, \tag{A.8}$$

from which, after some math,

$$d_{lum} = a_0^2 \frac{r}{a}. \tag{A.9}$$

While the former is inferred from the transversal dimension of the source (from the FLRW metric), the latter is constructed to preserve the Euclidean law for the flux (for the complete derivation, see e.g. Coles and Lucchin (1995)), in which the flux observed scales with d^{-2}.

For flat universes (where $f(r) = r$) one can relate both angular–diameter and luminosity distance to the comoving and proper distances by:

$$d_{ang} = d_p = \frac{d_{com}}{(1+z)}, \tag{A.10}$$

$$d_{lum} = d_p(1+z)^2 = d_{com}(1+z). \tag{A.11}$$

In Fig. A.1 we show the distance, calculated according to the different definitions, as function of redshift. We assume here a flat universe with "standard" cosmology, where $\Omega_{0,M} = 0.3$, $\Omega_{0,\Lambda} = 0.7$, $\Omega_{0,r} = 0$ and $h = 0.7$. It is interesting to notice from this figure that the angular–diameter distance is not monotonically increasing with redshift.
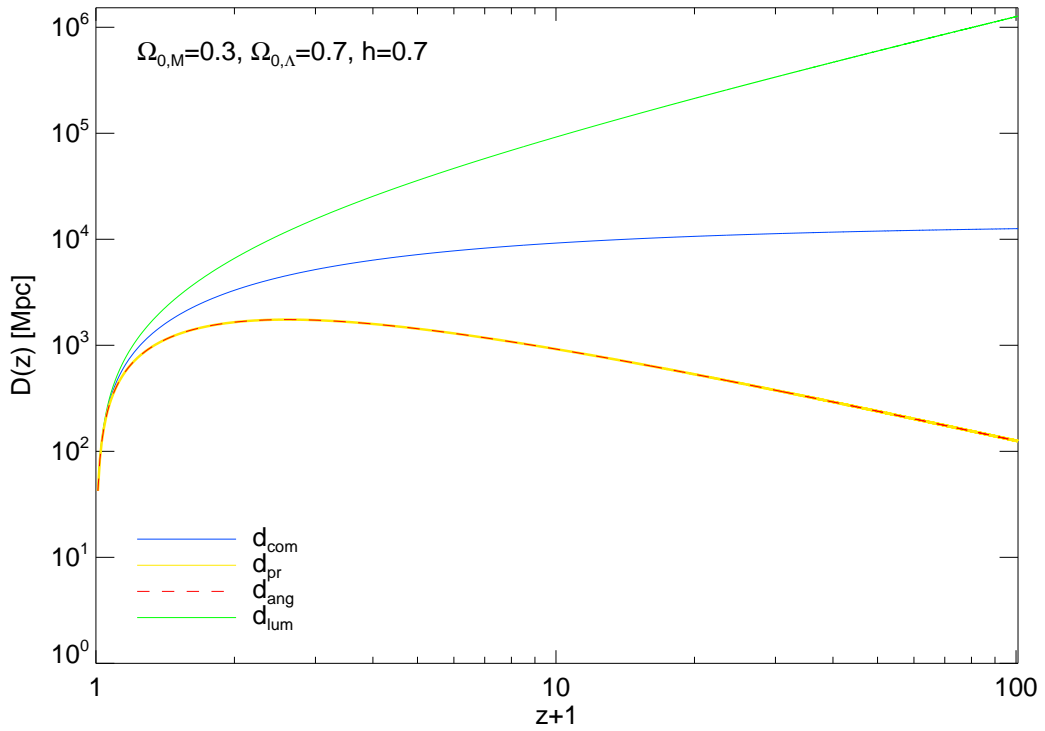
Figure A.1: Cosmological distances as function of the redshift. All the distances are calculated for a flat universe with "standard" cosmology, $\Omega_{0,M} = 0.3$, $\Omega_{0,\Lambda} = 0.7$, $\Omega_{0,r} = 0$ and $h = 0.7$. Specifically, each curve refers to a different definition of distance: the comoving distance (blue), the proper distance (yellow), the angular–diameter distance (red, dashed; for a flat universe this is equal to the proper distance), and the luminosity distance (green).

Part IV

Bibliography

Bibliography

Akamatsu, H., Hoshino, A., Ishisaki, Y., Ohashi, T., Sato, K., Takei, Y., and Ota, N. (2011). X-Ray Study of the Outer Region of Abell 2142 with Suzaku. *ArXiv e-prints*.

Akritas, M. G. and Bershady, M. A. (1996). Linear Regression for Astronomical Data with Measurement Errors and Intrinsic Scatter. *ApJ*, 470:706.

Anders, E. and Grevesse, N. (1989). Abundances of the elements - Meteoritic and solar. *Geochim. Cosmochim. Acta*, 53:197–214.

Arnaud, K. A. (1996). XSPEC: The First Ten Years. In G. H. Jacoby & J. Barnes, editor, *Astronomical Data Analysis Software and Systems V*, volume 101 of *Astronomical Society of the Pacific Conference Series*, pages 17–+.

Arnaud, M., Pointecouteau, E., and Pratt, G. W. (2005). The structural and scaling properties of nearby galaxy clusters. II. The M-T relation. *A&A*, 441:893–903.

Ascasibar, Y. and Markevitch, M. (2006). The Origin of Cold Fronts in the Cores of Relaxed Galaxy Clusters. *ApJ*, 650:102–127.

Balogh, M. L., Pearce, F. R., Bower, R. G., and Kay, S. T. (2001). Revisiting the cosmic cooling crisis. *MNRAS*, 326:1228–1234.

Bartelmann, M., Doran, M., and Wetterich, C. (2006). Non-linear structure formation in cosmologies with early dark energy. *A&A*, 454:27–36.

Bautz, M. W., Miller, E. D., Sanders, J. S., Arnaud, K. A., Mushotzky, R. F., Porter, F. S., Hayashida, K., Henry, J. P., Hughes, J. P., Kawaharada, M., Makashima, K., Sato, M., and Tamura, T. (2009). Suzaku Observations of Abell 1795: Cluster Emission to r_200. *Pub. Astron. Soc. Japan*, 61:1117–.

Biffi, V., Dolag, K., and Böhringer, H. (2011). Velocity structure diagnostics of simulated galaxy clusters. *MNRAS*, 413:573–584.

Biffi, V., Dolag, K., Böhringer, H., and Lemson, G. (2012). Observing simulated galaxy clusters with PHOX: a novel X-ray photon simulator. *MNRAS*, 420:3545–3556.

Binney, J. and Tremaine, S. (2008). *Galactic Dynamics: Second Edition*. Princeton University Press.

Blackburn, J. K. (1995). FTOOLS: A FITS Data Processing and Analysis Software Package. In R. A. Shaw, H. E. Payne, & J. J. E. Hayes, editor, *Astronomical Data Analysis Software and Systems IV*, volume 77 of *Astronomical Society of the Pacific Conference Series*, pages 367–+.

Böhringer, H., Belsole, E., Kennea, J., Matsushita, K., Molendi, S., Worrall, D. M., Mushotzky, R. F., Ehle, M., Guainazzi, M., Sakelliou, I., Stewart, G., Vestrand, W. T., and Dos Santos, S. (2001). XMM-Newton observations of M 87 and its X-ray halo. *A&A*, 365:L181–L187.

Böhringer, H. and Werner, N. (2010). X-ray spectroscopy of galaxy clusters: studying astrophysical processes in the largest celestial laboratories. *A&A Rev.*, 18:127–196.

Bonafede, A., Feretti, L., Murgia, M., Govoni, F., Giovannini, G., Dallacasa, D., Dolag, K., and Taylor, G. B. (2010). The Coma cluster magnetic field from Faraday rotation measures. *A&A*, 513:A30.

Booth, C. M. and Schaye, J. (2009). Cosmological simulations of the growth of supermassive black holes and feedback from active galactic nuclei: method and tests. *MNRAS*, 398:53–74.

Borgani, S., Dolag, K., Murante, G., Cheng, L.-M., Springel, V., Diaferio, A., Moscardini, L., Tormen, G., Tornatore, L., and Tozzi, P. (2006). Hot and cooled baryons in smoothed particle hydrodynamic simulations of galaxy clusters: physics and numerics. *MNRAS*, 367:1641–1654.

Borgani, S. and Kravtsov, A. (2009). Cosmological simulations of galaxy clusters. *ArXiv e-prints*.

Brighenti, F. and Mathews, W. G. (2003). Feedback Heating in Cluster and Galactic Cooling Flows. *ApJ*, 587:580–588.

Brüggen, M., Ruszkowski, M., Simionescu, A., Hoeft, M., and Dalla Vecchia, C. (2005). Simulations of Magnetic Fields in Filaments. *ApJL*, 631:L21–L24.

Bryan, G. L. and Norman, M. L. (1998). Statistical Properties of X-Ray Clusters: Analytic and Numerical Comparisons. *ApJ*, 495:80.

Cassano, R. and Brunetti, G. (2005). Cluster mergers and non-thermal phenomena: a statistical magneto-turbulent model. *MNRAS*, 357:1313–1329.

Churazov, E., Brüggen, M., Kaiser, C. R., Böhringer, H., and Forman, W. (2001). Evolution of Buoyant Bubbles in M87. *ApJ*, 554:261–273.

Churazov, E., Vikhlinin, A., Zhuravleva, I., Schekochihin, A., Parrish, I., Sunyaev, R., Forman, W., Boehringer, H., and Randall, S. (2011). X-Ray surface brightness and gas density fluctuations in the Coma cluster. *ArXiv e-prints*.

Churazov, E., Zhuravleva, I., Sazonov, S., and Sunyaev, R. (2010). Resonant Scattering of X-ray Emission Lines in the Hot Intergalactic Medium. *Space Sci. Rev.*, 157:193–209.

Cleary, P. W. and Monaghan, J. J. (1999). Conduction Modelling Using Smoothed Particle Hydrodynamics. *Journal of Computational Physics*, 148:227–264.

Coles, P. and Lucchin, F. (1995). *Cosmology. The origin and evolution of cosmic structure.*

Dalla Vecchia, C. and Schaye, J. (2008). Simulating galactic outflows with kinetic supernova feedback. *MNRAS*, 387:1431–1444.

Davis, M., Efstathiou, G., Frenk, C. S., and White, S. D. M. (1985). The evolution of large-scale structure in a universe dominated by cold dark matter. *ApJ*, 292:371–394.

Di Matteo, T., Springel, V., and Hernquist, L. (2005). Energy input from quasars regulates the growth and activity of black holes and their host galaxies. *Nature*, 433:604–607.

Dolag, K., Bartelmann, M., and Lesch, H. (1999). SPH simulations of magnetic fields in galaxy clusters. *A&A*, 348:351–363.

Dolag, K., Bartelmann, M., Perrotta, F., Baccigalupi, C., Moscardini, L., Meneghetti, M., and Tormen, G. (2004). Numerical study of halo concentrations in dark-energy cosmologies. *A&A*, 416:853–864.

Dolag, K., Borgani, S., Murante, G., and Springel, V. (2009). Substructures in hydrodynamical cluster simulations. *MNRAS*, 399:497–514.

Dolag, K., Meneghetti, M., Moscardini, L., Rasia, E., and Bonaldi, A. (2006). Simulating the physical properties of dark matter and gas inside the cosmic web. *MNRAS*, 370:656–672.

Dolag, K., Reinecke, M., Gheller, C., and Imboden, S. (2008). Splotch: visualizing cosmological simulations. *New Journal of Physics*, 10(12):125006.

Dolag, K. and Schindler, S. (2000). The effect of magnetic fields on the mass determination of clusters of galaxies. *A&A*, 364:491–496.

Dolag, K. and Stasyszyn, F. (2009). An MHD GADGET for cosmological simulations. *MNRAS*, 398:1678–1697.

Dolag, K., Vazza, F., Brunetti, G., and Tormen, G. (2005). Turbulent gas motions in galaxy cluster simulations: the role of smoothed particle hydrodynamics viscosity. *MNRAS*, 364:753–772.

Dubois, Y., Devriendt, J., Slyz, A., and Teyssier, R. (2010). Jet-regulated cooling catastrophe. *MNRAS*, 409:985–1001.

Ettori, S. and Molendi, S. (2011). X-ray observations of cluster outskirts: current status and future prospects. *Memorie della Societa Astronomica Italiana Supplementi*, 17:47–+.

Fabian, A. C. (1994). Cooling Flows in Clusters of Galaxies. *ARA&A*, 32:277–318.

Fabian, A. C. and Nulsen, P. E. J. (1977). Subsonic accretion of cooling gas in clusters of galaxies. *MNRAS*, 180:479–484.

Fabian, A. C., Sanders, J. S., Taylor, G. B., Allen, S. W., Crawford, C. S., Johnstone, R. M., and Iwasawa, K. (2006). A very deep Chandra observation of the Perseus cluster: shocks, ripples and conduction. *MNRAS*, 366:417–428.

Fabjan, D., Borgani, S., Tornatore, L., Saro, A., Murante, G., and Dolag, K. (2010). Simulating the effect of active galactic nuclei feedback on the metal enrichment of galaxy clusters. *MNRAS*, 401:1670–1690.

Fang, T., Humphrey, P., and Buote, D. (2009). Rotation and Turbulence of the Hot Intracluster Medium in Galaxy Clusters. *ApJ*, 691:1648–1659.

Frenk, C. S., White, S. D. M., Davis, M., and Efstathiou, G. (1988). The formation of dark halos in a universe dominated by cold dark matter. *ApJ*, 327:507–525.

Frenk, C. S., White, S. D. M., Efstathiou, G., and Davis, M. (1985). Cold dark matter, the structure of galactic haloes and the origin of the Hubble sequence. *Nature*, 317:595–597.

Fryxell, B., Olson, K., Ricker, P., Timmes, F. X., Zingale, M., Lamb, D. Q., MacNeice, P., Rosner, R., Truran, J. W., and Tufo, H. (2000). FLASH: An Adaptive Mesh Hydrodynamics Code for Modeling Astrophysical Thermonuclear Flashes. *ApJS*, 131:273–334.

Fujita, Y., Tawa, N., Hayashida, K., Takizawa, M., Matsumoto, H., Okabe, N., and Reiprich, T. H. (2008). High Metallicity of the X-Ray Gas Up to the Virial Radius of a Binary Cluster of Galaxies: Evidence of Galactic Superwinds at High-Redshift. *Pub. Astron. Soc. Japan*, 60:343–+.

Gardini, A., Rasia, E., Mazzotta, P., Tormen, G., De Grandi, S., and Moscardini, L. (2004). Simulating Chandra observations of galaxy clusters. *MNRAS*, 351:505–514.

George, M. R., Fabian, A. C., Sanders, J. S., Young, A. J., and Russell, H. R. (2009). X-ray observations of the galaxy cluster PKS0745-191: to the virial radius, and beyond. *MNRAS*, 395:657–666.

Gilfanov, M. R., Syunyaev, R. A., and Churazov, E. M. (1987). Radial Brightness Profiles of Resonance X-Ray Lines in Galaxy Clusters. *Soviet Astronomy Letters*, 13:3.

Gunn, J. E. and Gott, III, J. R. (1972). On the Infall of Matter Into Clusters of Galaxies and Some Effects on Their Evolution. *ApJ*, 176:1.

Heinz, S. and Brüggen, M. (2009). XIM: A virtual X-ray observatory for hydrodynamic simulations. *ArXiv e-prints*.

Heinz, S., Brüggen, M., and Morsony, B. (2010). Prospects of High-Resolution X-ray Spectroscopy for Active Galactic Nucleus Feedback in Galaxy Clusters. *ApJ*, 708:462–468.

Hoshino, A., Henry, J. P., Sato, K., Akamatsu, H., Yokota, W., Sasaki, S., Ishisaki, Y., Ohashi, T., Bautz, M., Fukazawa, Y., Kawano, N., Furuzawa, A., Hayashida, K., Tawa, N., Hughes, J. P., Kokubun, M., and Tamura, T. (2010). X-Ray Temperature and Mass Measurements to the Virial Radius of Abell 1413 with Suzaku. *Pub. Astron. Soc. Japan*, 62:371–389.

Iapichino, L. and Niemeyer, J. C. (2008). Hydrodynamical adaptive mesh refinement simulations of turbulent flows - II. Cosmological simulations of galaxy clusters. *MNRAS*, 388:1089–1100.

Iapichino, L., Schmidt, W., Niemeyer, J. C., and Merklein, J. (2011). Turbulence production and turbulent pressure support in the intergalactic medium. *MNRAS*, 414:2297–2308.

Inogamov, N. A. and Sunyaev, R. A. (2003). Turbulence in Clusters of Galaxies and X-ray Line Profiles. *Astronomy Letters*, 29:791–824.

Ishisaki, Y., Maeda, Y., Fujimoto, R., Ozaki, M., Ebisawa, K., Takahashi, T., Ueda, Y., Ogasaka, Y., Ptak, A., and 25 co–authors (2007). Monte Carlo Simulator and Ancillary Response Generator of Suzaku XRT/XIS System for Spatially Extended Source Analysis. *Pub. Astron. Soc. Japan*, 59:113–132.

Jenkins, A., Frenk, C. S., White, S. D. M., Colberg, J. M., Cole, S., Evrard, A. E., Couchman, H. M. P., and Yoshida, N. (2001). The mass function of dark matter haloes. *MNRAS*, 321:372–384.

Jubelgas, M., Springel, V., and Dolag, K. (2004). Thermal conduction in cosmological SPH simulations. *MNRAS*, 351:423–435.

Jubelgas, M., Springel, V., Enßlin, T., and Pfrommer, C. (2008). Cosmic ray feedback in hydrodynamical simulations of galaxy formation. *A&A*, 481:33–63.

Kaastra, J. S., Ferrigno, C., Tamura, T., Paerels, F. B. S., Peterson, J. R., and Mittaz, J. P. D. (2001). XMM-Newton observations of the cluster of galaxies Sérsic 159-03. *A&A*, 365:L99–L103.

Kaastra, J. S. and Mewe, R. (1993). X-ray emission from thin plasmas. I - Multiple Auger ionisation and fluorescence processes for Be to Zn. *A&A Supp.*, 97:443–482.

Kaastra, J. S., Paerels, F. B. S., Durret, F., Schindler, S., and Richter, P. (2008). Thermal Radiation Processes. *Space Sci. Rev.*, 134:155–190.

Kaastra, J. S., Tamura, T., Peterson, J. R., Bleeker, J. A. M., Ferrigno, C., Kahn, S. M., Paerels, F. B. S., Piffaretti, R., Branduardi-Raymont, G., and Böhringer, H. (2004). Spatially resolved X-ray spectroscopy of cooling clusters of galaxies. *A&A*, 413:415–439.

Kaiser, N. (1986). Evolution and clustering of rich clusters. *MNRAS*, 222:323–345.

Katz, N. (1992). Dissipational galaxy formation. II - Effects of star formation. *ApJ*, 391:502–517.

Katz, N., Weinberg, D. H., and Hernquist, L. (1996). Cosmological Simulations with TreeSPH. *ApJS*, 105:19–+.

Katz, N. and White, S. D. M. (1993). Hierarchical galaxy formation - Overmerging and the formation of an X-ray cluster. *ApJ*, 412:455–478.

Kawahara, H., Reese, E. D., Kitayama, T., Sasaki, S., and Suto, Y. (2008). Extracting Galaxy Cluster Gas Inhomogeneity from X-Ray Surface Brightness: A Statistical Approach and Application to Abell 3667. *ApJ*, 687:936–950.

Kawahara, H., Suto, Y., Kitayama, T., Sasaki, S., Shimizu, M., Rasia, E., and Dolag, K. (2007). Radial Profile and Lognormal Fluctuations of the Intracluster Medium as the Origin of Systematic Bias in Spectroscopic Temperature. *ApJ*, 659:257–266.

Kawaharada, M., Okabe, N., Umetsu, K., Takizawa, M., Matsushita, K., Fukazawa, Y., Hamana, T., Miyazaki, S., Nakazawa, K., and Ohashi, T. (2010). Suzaku Observation of A1689: Anisotropic Temperature and Entropy Distributions Associated with the Large-scale Structure. *ApJ*, 714:423–441.

Kellogg, E., Gursky, H., Tananbaum, H., Giacconi, R., and Pounds, K. (1972). The Extended X-Ray Source at M87. *ApJL*, 174:L65.

Kitayama, T. and Suto, Y. (1996). Semianalytic Predictions for Statistical Properties of X-Ray Clusters of Galaxies in Cold Dark Matter Universes. *ApJ*, 469:480.

Komatsu, E., Smith, K. M., Dunkley, J., Bennett, C. L., Gold, B., Hinshaw, G., Jarosik, N., Larson, D., Nolta, M. R., Page, L., Spergel, D. N., Halpern, M., Hill, R. S., Kogut, A., Limon, M., Meyer, S. S., Odegard, N., Tucker, G. S., Weiland, J. L., Wollack, E., and Wright, E. L. (2011). Seven-year Wilkinson Microwave Anisotropy Probe (WMAP) Observations: Cosmological Interpretation. *ApJS*, 192:18–+.

Kravtsov, A. V. (1999). *High-resolution simulations of structure formation in the universe.* PhD thesis, NEW MEXICO STATE UNIVERSITY.

Kravtsov, A. V., Klypin, A., and Hoffman, Y. (2002). Constrained Simulations of the Real Universe. II. Observational Signatures of Intergalactic Gas in the Local Supercluster Region. *ApJ*, 571:563–575.

Kravtsov, A. V., Nagai, D., and Vikhlinin, A. A. (2005). Effects of Cooling and Star Formation on the Baryon Fractions in Clusters. *ApJ*, 625:588–598.

Kravtsov, A. V., Vikhlinin, A., and Nagai, D. (2006). A New Robust Low-Scatter X-Ray Mass Indicator for Clusters of Galaxies. *ApJ*, 650:128–136.

Laganá, T. F., de Souza, R. S., and Keller, G. R. (2010). On the influence of non-thermal pressure on the mass determination of galaxy clusters. *A&A*, 510:A76+.

Lau, E. T., Kravtsov, A. V., and Nagai, D. (2009). Residual Gas Motions in the Intracluster Medium and Bias in Hydrostatic Measurements of Mass Profiles of Clusters. *ApJ*, 705:1129–1138.

Lau, E. T., Nagai, D., Kravtsov, A. V., and Zentner, A. R. (2011). Shapes of Gas, Gravitational Potential, and Dark Matter in ΛCDM Clusters. *ApJ*, 734:93–+.

Liedahl, D. A., Osterheld, A. L., and Goldstein, W. H. (1995). New calculations of Fe L-shell X-ray spectra in high-temperature plasmas. *ApJL*, 438:L115–L118.

Lin, Y.-T., Mohr, J. J., and Stanford, S. A. (2003). Near-Infrared Properties of Galaxy Clusters: Luminosity as a Binding Mass Predictor and the State of Cluster Baryons. *ApJ*, 591:749–763.

Maio, U., Ciardi, B., Dolag, K., Tornatore, L., and Khochfar, S. (2010). The transition from population III to population II-I star formation. *MNRAS*, 407:1003–1015.

Maio, U., Dolag, K., Ciardi, B., and Tornatore, L. (2007). Metal and molecule cooling in simulations of structure formation. *MNRAS*, 379:963–973.

Markevitch, M. and Vikhlinin, A. (2007). Shocks and cold fronts in galaxy clusters. *Phys. Rep.*, 443:1–53.

Marri, S. and White, S. D. M. (2003). Smoothed particle hydrodynamics for galaxy-formation simulations: improved treatments of multiphase gas, of star formation and of supernovae feedback. *MNRAS*, 345:561–574.

Mathews, W. G. and Brighenti, F. (2003). Hot Gas in and around Elliptical Galaxies. *ARA&A*, 41:191–239.

Mazzotta, P., Rasia, E., Moscardini, L., and Tormen, G. (2004). Comparing the temperatures of galaxy clusters from hydrodynamical N-body simulations to Chandra and XMM-Newton observations. *MNRAS*, 354:10–24.

McCarthy, I. G., Schaye, J., Ponman, T. J., Bower, R. G., Booth, C. M., Dalla Vecchia, C., Crain, R. A., Springel, V., Theuns, T., and Wiersma, R. P. C. (2010). The case for AGN feedback in galaxy groups. *MNRAS*, 406:822–839.

McNamara, B. R. and Nulsen, P. E. J. (2007). Heating Hot Atmospheres with Active Galactic Nuclei. *ARA&A*, 45:117–175.

Mewe, R., Gronenschild, E. H. B. M., and van den Oord, G. H. J. (1985). Calculated X-radiation from optically thin plasmas. V. *A&A Supp.*, 62:197–254.

Mittal, R., Hicks, A., Reiprich, T. H., and Jaritz, V. (2011). The L_X - T_{vir} relation in galaxy clusters: effects of radiative cooling and AGN heating. *A&A*, 532:A133.

Molendi, S. and Pizzolato, F. (2001). Is the Gas in Cooling Flows Multiphase? *ApJ*, 560:194–200.

Monaghan, J. J. (1997). SPH and Riemann Solvers. *Journal of Computational Physics*, 136:298–307.

Monaghan, J. J. and Gingold, R. A. (1983). Shock Simulation by the Particle Method SPH. *Journal of Computational Physics*, 52:374–+.

Morris, J. P. and Monaghan, J. J. (1997). A Switch to Reduce SPH Viscosity. *Journal of Computational Physics*, 136:41–50.

Morrison, R. and McCammon, D. (1983). Interstellar photoelectric absorption cross sections, 0.03-10 keV. *ApJ*, 270:119–122.

Mosconi, M. B., Tissera, P. B., Lambas, D. G., and Cora, S. A. (2001). Chemical evolution using smooth particle hydrodynamical cosmological simulations - I. Implementation, tests and first results. *MNRAS*, 325:34–48.

Nagai, D., Vikhlinin, A., and Kravtsov, A. V. (2007). Testing X-Ray Measurements of Galaxy Clusters with Cosmological Simulations. *ApJ*, 655:98–108.

Navarro, J. F., Frenk, C. S., and White, S. D. M. (1995). Simulations of X-ray clusters. *MNRAS*, 275:720–740.

Navarro, J. F., Frenk, C. S., and White, S. D. M. (1996). The Structure of Cold Dark Matter Halos. *ApJ*, 462:563.

Navarro, J. F., Frenk, C. S., and White, S. D. M. (1997). A Universal Density Profile from Hierarchical Clustering. *ApJ*, 490:493.

Navarro, J. F. and White, S. D. M. (1993). Simulations of Dissipative Galaxy Formation in Hierarchically Clustering Universes - Part One - Tests of the Code. *MNRAS*, 265:271–+.

Nord, B., Stanek, R., Rasia, E., and Evrard, A. E. (2008). Effects of selection and covariance on X-ray scaling relations of galaxy clusters. *MNRAS*, 383:L10–L14.

Norman, M. L. and Bryan, G. L. (1999). Cluster Turbulence. In H.-J. Röser & K. Meisenheimer, editor, *The Radio Galaxy Messier 87*, volume 530 of *Lecture Notes in Physics, Berlin Springer Verlag*, page 106.

Norman, M. L., Bryan, G. L., Harkness, R., Bordner, J., Reynolds, D., O'Shea, B., and Wagner, R. (2007). Simulating Cosmological Evolution with Enzo. *ArXiv e-prints*.

Parrish, I. J., McCourt, M., Quataert, E., and Sharma, P. (2011). Turbulent pressure support in the outer parts of galaxy clusters. *MNRAS*, page L356.

Pawl, A., Evrard, A. E., and Dupke, R. A. (2005). Detecting Intracluster Gas Motion in Galaxy Clusters: Mock Astro-E2 Observations. *ApJ*, 631:773–784.

Peacock, J. A. (1999). *Cosmological Physics*.

Perlmutter, S., Aldering, G., Goldhaber, G., Knop, R. A., Nugent, P., Castro, P. G., Deustua, S., Fabbro, S., Goobar, A., Groom, D. E., Hook, I. M., Kim, A. G., Kim, M. Y., Lee, J. C., Nunes, N. J., Pain, R., Pennypacker, C. R., Quimby, R., Lidman, C., Ellis, R. S., Irwin, M., McMahon, R. G., Ruiz-Lapuente, P., Walton, N., Schaefer, B., Boyle, B. J., Filippenko, A. V., Matheson, T., Fruchter, A. S., Panagia, N., Newberg, H. J. M., Couch, W. J., and The Supernova Cosmology Project (1999). Measurements of Omega and Lambda from 42 High-Redshift Supernovae. *ApJ*, 517:565–586.

Peterson, J. R., Kahn, S. M., Paerels, F. B. S., Kaastra, J. S., Tamura, T., Bleeker, J. A. M., Ferrigno, C., and Jernigan, J. G. (2003). High-Resolution X-Ray Spectroscopic Constraints on Cooling-Flow Models for Clusters of Galaxies. *ApJ*, 590:207–224.

Peterson, J. R., Paerels, F. B. S., Kaastra, J. S., Arnaud, M., Reiprich, T. H., Fabian, A. C., Mushotzky, R. F., Jernigan, J. G., and Sakelliou, I. (2001). X-ray imaging-spectroscopy of Abell 1835. *A&A*, 365:L104–L109.

Pfrommer, C., Enßlin, T. A., Springel, V., Jubelgas, M., and Dolag, K. (2007). Simulating cosmic rays in clusters of galaxies - I. Effects on the Sunyaev-Zel'dovich effect and the X-ray emission. *MNRAS*, 378:385–408.

Phillips, G. J. and Monaghan, J. J. (1985). A numerical method for three-dimensional simulations of collapsing, isothermal, magnetic gas clouds. *MNRAS*, 216:883–895.

Piffaretti, R. and Valdarnini, R. (2008). Total mass biases in X-ray galaxy clusters. *A&A*, 491:71–87.

Pratt, G. W., Croston, J. H., Arnaud, M., and Böhringer, H. (2009). Galaxy cluster X-ray luminosity scaling relations from a representative local sample (REXCESS). *A&A*, 498:361–378.

Press, W. H. and Schechter, P. (1974). Formation of Galaxies and Clusters of Galaxies by Self-Similar Gravitational Condensation. *ApJ*, 187:425–438.

Price, D. J. and Monaghan, J. J. (2005). Smoothed Particle Magnetohydrodynamics - III. Multidimensional tests and the $\nabla.B = 0$ constraint. *MNRAS*, 364:384–406.

Puchwein, E., Sijacki, D., and Springel, V. (2008). Simulations of AGN Feedback in Galaxy Clusters and Groups: Impact on Gas Fractions and the L_X-T Scaling Relation. *ApJL*, 687:L53–L56.

Rasia, E., Ettori, S., Moscardini, L., Mazzotta, P., Borgani, S., Dolag, K., Tormen, G., Cheng, L. M., and Diaferio, A. (2006). Systematics in the X-ray cluster mass estimators. *MNRAS*, 369:2013–2024.

Rasia, E., Mazzotta, P., Bourdin, H., Borgani, S., Tornatore, L., Ettori, S., Dolag, K., and Moscardini, L. (2008). X-MAS2: Study Systematics on the ICM Metallicity Measurements. *ApJ*, 674:728–741.

Rasia, E., Meneghetti, M., Martino, R., Borgani, S., Bonafede, A., Dolag, K., Ettori, S., Fabjan, D., Giocoli, C., Mazzotta, P., Merten, J., Radovich, M., and Tornatore, L. (2012). Lensing and X-ray mass estimates of clusters (SIMULATION). *ArXiv e-prints*.

Rasia, E., Tormen, G., and Moscardini, L. (2004). A dynamical model for the distribution of dark matter and gas in galaxy clusters. *MNRAS*, 351:237–252.

Rebusco, P., Churazov, E., Sunyaev, R., Böhringer, H., and Forman, W. (2008). Width of X-ray lines as a diagnostic of gas motions in cooling flows. *MNRAS*, 384:1511–1518.

Reiprich, T. H. and Böhringer, H. (2002). The Mass Function of an X-Ray Flux-limited Sample of Galaxy Clusters. *ApJ*, 567:716–740.

Reiprich, T. H., Hudson, D. S., Zhang, Y.-Y., Sato, K., Ishisaki, Y., Hoshino, A., Ohashi, T., Ota, N., and Fujita, Y. (2009). Suzaku measurement of Abell 2204's intracluster gas temperature profile out to 1800 kpc. *A&A*, 501:899–905.

Riess, A. G., Filippenko, A. V., Challis, P., Clocchiatti, A., Diercks, A., Garnavich, P. M., Gilliland, R. L., Hogan, C. J., Jha, S., Kirshner, R. P., Leibundgut, B., Phillips, M. M., Reiss, D., Schmidt, B. P., Schommer, R. A., Smith, R. C., Spyromilio, J., Stubbs, C., Suntzeff, N. B., and Tonry, J. (1998). Observational Evidence from Supernovae for an Accelerating Universe and a Cosmological Constant. *AJ*, 116:1009–1038.

Ruszkowski, M., Lee, D., Bruggen, M., Parrish, I., and Oh, S. P. (2010). Cosmological MHD simulations of cluster formation with anisotropic thermal conduction. *ArXiv e-prints*.

Sanders, J. S., Fabian, A. C., and Smith, R. K. (2011). Constraints on turbulent velocity broadening for a sample of clusters, groups and elliptical galaxies using XMM-Newton. *MNRAS*, 410:1797–1812.

Sarazin, C. L. (1988). *X-ray emission from clusters of galaxies*.

Scannapieco, C., Tissera, P. B., White, S. D. M., and Springel, V. (2005). Feedback and metal enrichment in cosmological smoothed particle hydrodynamics simulations - I. A model for chemical enrichment. *MNRAS*, 364:552–564.

Scannapieco, C., Tissera, P. B., White, S. D. M., and Springel, V. (2006). Feedback and metal enrichment in cosmological SPH simulations - II. A multiphase model with supernova energy feedback. *MNRAS*, 371:1125–1139.

Schuecker, P., Finoguenov, A., Miniati, F., Böhringer, H., and Briel, U. G. (2004). Probing turbulence in the Coma galaxy cluster. *A&A*, 426:387–397.

Sijacki, D., Pfrommer, C., Springel, V., and Enßlin, T. A. (2008). Simulations of cosmic-ray feedback by active galactic nuclei in galaxy clusters. *MNRAS*, 387:1403–1415.

Sijacki, D. and Springel, V. (2006). Hydrodynamical simulations of cluster formation with central AGN heating. *MNRAS*, 366:397–416.

Sijacki, D., Springel, V., Di Matteo, T., and Hernquist, L. (2007). A unified model for AGN feedback in cosmological simulations of structure formation. *MNRAS*, 380:877–900.

Simionescu, A., Allen, S. W., Mantz, A., Werner, N., Takei, Y., Morris, R. G., Fabian, A. C., Sanders, J. S., Nulsen, P. E. J., George, M. R., and Taylor, G. B. (2011). Baryons at the Edge of the X-ray-Brightest Galaxy Cluster. *Science*, 331:1576–.

Smith, R. K., Brickhouse, N. S., Liedahl, D. A., and Raymond, J. C. (2001). Collisional Plasma Models with APEC/APED: Emission-Line Diagnostics of Hydrogen-like and Helium-like Ions. *ApJL*, 556:L91–L95.

Spergel, D. N., Bean, R., Doré, O., Nolta, M. R., Bennett, C. L., Dunkley, J., Hinshaw, G., Jarosik, N., Komatsu, E., Page, L., Peiris, H. V., Verde, L., Halpern, M., Hill, R. S., Kogut, A., Limon, M., Meyer, S. S., Odegard, N., Tucker, G. S., Weiland, J. L., Wollack, E., and Wright, E. L. (2007). Three-Year Wilkinson Microwave Anisotropy Probe (WMAP) Observations: Implications for Cosmology. *ApJS*, 170:377–408.

Springel, V. (2005). The cosmological simulation code GADGET-2. *MNRAS*, 364:1105–1134.

Springel, V., Di Matteo, T., and Hernquist, L. (2005a). Modelling feedback from stars and black holes in galaxy mergers. *MNRAS*, 361:776–794.

Springel, V. and Hernquist, L. (2003). Cosmological smoothed particle hydrodynamics simulations: a hybrid multiphase model for star formation. *MNRAS*, 339:289–311.

Springel, V., White, M., and Hernquist, L. (2001). Hydrodynamic Simulations of the Sunyaev-Zeldovich Effect(s). *ApJ*, 549:681–687.

Springel, V., White, S. D. M., Jenkins, A., Frenk, C. S., Yoshida, N., Gao, L., Navarro, J., Thacker, R., Croton, D., Helly, J., Peacock, J. A., Cole, S., Thomas, P., Couchman, H., Evrard, A., Colberg, J., and Pearce, F. (2005b). Simulations of the formation, evolution and clustering of galaxies and quasars. *Nature*, 435:629–636.

Stanek, R., Rasia, E., Evrard, A. E., Pearce, F., and Gazzola, L. (2010). Massive Halos in Millennium Gas Simulations: Multivariate Scaling Relations. *ApJ*, 715:1508–1523.

Sunyaev, R. A., Norman, M. L., and Bryan, G. L. (2003). On the Detectability of Turbulence and Bulk Flows in X-ray Clusters. *Astronomy Letters*, 29:783–790.

Teyssier, R., Moore, B., Martizzi, D., Dubois, Y., and Mayer, L. (2011). Mass distribution in galaxy clusters: the role of Active Galactic Nuclei feedback. *MNRAS*, 414:195–208.

Tormen, G., Bouchet, F. R., and White, S. D. M. (1997). The structure and dynamical evolution of dark matter haloes. *MNRAS*, 286:865–884.

Tornatore, L., Borgani, S., Dolag, K., and Matteucci, F. (2007). Chemical enrichment of galaxy clusters from hydrodynamical simulations. *MNRAS*, 382:1050–1072.

Tornatore, L., Borgani, S., Matteucci, F., Recchi, S., and Tozzi, P. (2004). Simulating the metal enrichment of the intracluster medium. *MNRAS*, 349:L19–L24.

Vazza, F., Brunetti, G., Gheller, C., Brunino, R., and Brüggen, M. (2011). Massive and refined. II. The statistical properties of turbulent motions in massive galaxy clusters with high spatial resolution. *A&A*, 529:A17.

Vazza, F., Brunetti, G., Kritsuk, A., Wagner, R., Gheller, C., and Norman, M. (2009). Turbulent motions and shocks waves in galaxy clusters simulated with adaptive mesh refinement. *A&A*, 504:33–43.

Weinberg, N. N. and Kamionkowski, M. (2003). Constraining dark energy from the abundance of weak gravitational lenses. *MNRAS*, 341:251–262.

Werner, N., Zhuravleva, I., Churazov, E., Simionescu, A., Allen, S. W., Forman, W., Jones, C., and Kaastra, J. S. (2009). Constraints on turbulent pressure in the X-ray haloes of giant elliptical galaxies from resonant scattering. *MNRAS*, 398:23–32.

White, S. D. M., Davis, M., Efstathiou, G., and Frenk, C. S. (1987). Galaxy distribution in a cold dark matter universe. *Nature*, 330:451–453.

White, S. D. M. and Rees, M. J. (1978). Core condensation in heavy halos - A two-stage theory for galaxy formation and clustering. *MNRAS*, 183:341–358.

Yoshida, N., Abel, T., Hernquist, L., and Sugiyama, N. (2003). Simulations of Early Structure Formation: Primordial Gas Clouds. *ApJ*, 592:645–663.

Yoshida, N., Colberg, J., White, S. D. M., Evrard, A. E., MacFarland, T. J., Couchman, H. M. P., Jenkins, A., Frenk, C. S., Pearce, F. R., Efstathiou, G., Peacock, J. A., and Thomas, P. A. (2001). Simulations of deep pencil-beam redshift surveys. *MNRAS*, 325:803–816.

Zhuravleva, I. V., Churazov, E. M., Sazonov, S. Y., Sunyaev, R. A., Forman, W., and Dolag, K. (2010). Polarization of X-ray lines from galaxy clusters and elliptical galaxies - a way to measure the tangential component of gas velocity. *MNRAS*, 403:129–150.

Zwicky, F. (1937). On the Masses of Nebulae and of Clusters of Nebulae. *ApJ*, 86:217.

Acknowledgments

First of all, I would like to thank my PhD supervisors, Hans Böringer and Klaus Dolag, for guiding me throughout these three years. I thank Hans for precious discussions and scientific support. I am grateful to Klaus for sincere and countinuous encouragement, for several useful suggestions and for the patience in answering all my questions. I thank both, together with the Max Planck Institutes for Astrophysics and for Extraterrestrial Physics and the International Max Planck Research School, for giving me the opportunity to do the PhD, improve my astrophysical knowledge and research experience.

I am grateful to all my friends in Italy and Munich, for the friendship and for all the amusing parties, beers and fun.

I am particularly thankful to my dearest friends, Lucia, Jessica, Claudia, for being always there.

To Umberto I dedicate a very special *thank you*, for sharing with me the most important and beautiful moments during these years and for always being present in the difficult ones.

Finally, my gratitude is for my parents, for giving me the possibility to pursue my dreams with unquestioning support and love. *Grazie per il vostro affetto e incoraggiamento, che hanno reso possibile tutto questo.*

Curriculum Vitae et Studiorum

Veronica Biffi

Contacts

Address:	Max–Planck Institut für Astrophysik
	c/o Max–Planck Institut für extraterrestrische Physik
	Giessenbachstr. 1, D–85748 Garching b. München, Germany
Phone:	+49 89 30000 3340
E–mail:	biffi@mpa-garching.mpg.de, biffi@mpe.mpg.de
Homepage:	http://www.mpe.mpg.de/∼biffi

Personal data

Born on December 2, 1984 in Grosseto (Italy).

Languages: Italian, English, German, French.

Education

2008 – 2012: PhD in Astrophysics
Ludwig–Maximilians–Universität, München, Germany
IMPRS fellow at MPA/MPE, Garching b. München, Germany
Research project: "Studying the physics of galaxy clusters
by simulations and X–ray observations"
Supervisors: Prof. Dr. Hans Böhringer, Dr. Klaus Dolag

2006 – 2008: M.Sc. in Astrophysics and Cosmology
Alma Mater Studiorum - University of Bologna, Italy
Thesis: "The spherical collapse in dark energy
models: application to galaxy clusters"
Supervisor: Prof. Lauro Moscardini
Co–supervisor: Dr. Stefano Ettori
Results: 110/110 cum laude

2003 – 2006: B.Sc. in Astronomy
Alma Mater Studiorum University of Bologna, Italy
Thesis: "Mass estimators of stellar systems from
projected dynamics"
Supervisor: Prof. Luca Ciotti
Results: 110/110 cum laude

1998 – 2003: High School
Liceo Scientifico "G. Marconi", Grosseto, Italy
Results: 100/100

Publications

Papers

1. "Observing simulated galaxy clusters with PHOX: a novel X–ray photon simulator"
   V. Biffi, K. Dolag, H. Böhringer, G. Lemson, 2012, MNRAS, 420, 3545;

2. "First simultaneous optical/near-infrared imaging of an X-ray selected, high-redshift cluster of galaxies with GROND"
   D. Pierini et al. (**V. Biffi** among the co–authors), 2012, A&A, 540, 45;

3. "Velocity structure diagnostics of simulated galaxy clusters"
   V. Biffi, K. Dolag, H. Böhringer, 2011, MNRAS, 413, 573;

In preparation

1. "Observing simulated galaxy clusters with PHOX: the prospects of velocity diagnostics of the ICM"
   V. Biffi, K. Dolag, H. Böhringer, 2012, to be submitted

Conference Proceedings

1. "Observing simulated clusters: a novel virtual X–ray telescope"
   V. Biffi, K. Dolag, H. Böhringer, G. Lemson, 2011, ASP Conference Series for the meeting "Advances in Computational Astrophysics: methods, tools and outcomes", R. Capuzzo–Dolcetta, M. Limongi and A. Tornambè eds;

2. "Velocity structure diagnostics of X–ray galaxy clusters"
   V. Biffi, K. Dolag, H. Böhringer, 2009, proceedings of the conference "The Energetic Cosmos: from *Suzaku* to *ASTRO–H*", JAXA Special Publication, JAXA–SP–09–008E (2010), 92;